Enhanced Crystallization of Amorphous Silicon Films with Silicon Nanocrystal Seeding

A DISSERTATION

SUBMITTED TO THE FACULTY OF THE GRADUATE SCHOOL

OF THE UNIVERSITY OF MINNESOTA

BY

Lin Cui

IN PARTIAL FULFILLMENT OF THE REQUIREMENTS

FOR THE DEGREE OF

Doctor of Philosophy

Uwe Kortshagen

November, 2013

Acknowledgements

There are so many people who have contributed to the completion of my PhD degree. My whole graduate career includes plenty of thoughts, ideas, trials, improvements, accomplishments as well as mistakes and failures. I could not have completed such long journey without the support and encouragement of my professors, teachers and labmates, not only practically but also mentally. I must thank all of them.

I would like to thank Professor Uwe Kortshagen, whose direction and guidance through a long period of six years gave a great amount of instruction and encouragement to my research work. Also I am greatly impressed by and have learned a lot from his personality and attitude.

I would like to thank Professor Steven Girshick, Professor James Kakalios and Professor David Pui for their feedback to my work and serving in my committee. I also thank Jason Trask and Andrew Wagner who have worked together with me for five years on the dual-plasma system. Without their co-operation and ideas I could hardly have finished my research. I need to thank other group members and HTPL members, such as David Rowe, Rebecca Anthony, Rick Liptak, Chin-Yi Liu, Katelyn Schramke, Brian Merritt, Jihua Yang, Dart-Ken Poon, Song Guo, Ting Chen, Pingyan Lei and other, with whom I have had a wonderful experience in the lab.

I also would like to thank all the characterization facility staff, including Ozan

Ugurlu, Jason Myers and Greg Haugstad, for their help with characterization experiments.

Finally I need to specially thank my parents, Huaibao Cui and Hui Zhao. Thank you for your long-time support and education over the past years, because without you it would be impossible for me to achieve my dreams. Finally thank my girlfriend Lingxiao Zhai for your companionship.

Dedication

To Dad and Mom, Mr. Huaibao Cui and Mrs. Hui Zhao, for their endless love and support.

Abstract

Over the last decade, the solar photovoltaics (PV) industry has grown rapidly with increasing fossil fuel cost and greenhouse gas emissions. The applications of high quality, large grain hydrogenated microcrystalline silicon (μc-Si:H) thin film transistors and solar cells have become popular in recent years. To attain stability and excellent electronic properties as well as the low manufacturing cost, one must produce μc-Si with the maximum possible grain sizes, ideally as large as the film thickness itself. However, the traditional plasma enhanced chemical vapor deposition (PECVD) process for μc-Si:H growth is limited by poor control over structural quality.

This work studies a new approach to synthesizing μc-Si:H with a lower thermal budget and better control of the microstructure, with potentially larger grain sizes. Such unique technique uses a low-pressure radio-frequency plasma reactor to synthesize silicon nanocrystals and embeds these nanocrystals in a-Si:H matrix, where they serve as starting points for crystal grain growth upon thermal annealing. In studying the crystallization process of seeded films, two important criteria are to be optimized: the maximization of crystal grain size, and minimization of annealing time. This work expects to reduce the annealing time by eliminating the incubation time by implanting nanocrystal seeds into the amorphous matrix. In regards to grain structure optimization, the final grain size can be controlled via controlling the initial seed concentration.

Furthermore, a new phenomenon of nanovoid enhanced crystallization is observed during heated stage TEM annealing of seeded films. Nanocavity regions, referred as "nanovoids", form at the interface between the nanoseeds and the amorphous matrix. Those nanovoids propagate through the film during annealing at a speed higher than

the solid-phase epitaxy (SPE) of the seeds and leave crystalline region behind, which further enhance the crystallization of amorphous Si films. The formation of nanovoids is related to film nanoporosity and the shadowing effect of the nanoparticles, and the void propagation mechanism is explained as a combination effect of atomic surface diffusion at its inner surface and the twin growth at its tail region. Efforts are made to control the nanovoid density as well as its crystallization enhancement effect, by tuning the film nanoporosity, the nanoparticle shape and introduction of a new seeded film structure.

Contents

List of Figures

Chapter 1

Introduction

1.1 Photovoltaics

The solar photovoltaics (PV) is a clean, sustainable and renewable technology, as well as one of the feasible replacements for the fossil fuel infrastructure offsetting increasing fuel costs and greenhouse gas emissions. Over the last decade, the global PV industry has grown in excess of 40% per year, due to both reduced manufacturing costs and government incentives [1]. The existing capacity of solar PV almost doubled to 40 GW from 23 GW during 2010 [2], and this value further increased by 74% to 70 GW in 2011 [3]. The global size of the PV industry exceeded USD 100 billion in 2011 [3], and its scale is predicted to continue to rise. Despite the increased demand for sustainable energy, current PV capacity is still small compared to the other renewable energy sources, as the economic barrier remains the primary restriction to the PV industry [4].

All solar cells require light absorbing materials to absorb photons and generate free electrons via the PV effect. Silicon (Si) is the most widely used material in PV cells [5]. This is in part due to the fact that Si is in large abundance on earth and also has good

stability as well as physical and chemical properties. Another reason why Si cells have been dominant is related to the wide application of Si materials in the microelectronics industry.

Solar cells can be grouped into two main categories: wafer-type cells (single or multi-crystalline) and thin-film solar cells (amorphous silicon, Cd-Te, CIGS, etc.) [6]. Wafer type cells are produced by cutting large cylindrical monocrystalline Si ingots, which are synthesized from high-purity molten silicon. Nearly 95% of the PV market is dominated by the wafer-type crystalline silicon while the remaining 5% are mainly silicon thin-film solar cells. The current record for conversion efficiency of crystalline Si (c-Si) cells is near 25%, while thin-film Si cells have efficiencies only as high as 10% [7]. Although obtaining outstanding efficiency, further mass production of c-Si cells is limited because of their high cost. Therefore the PV industry is now moving toward the silicon thin-film cell because of its potential reduction of energy payback time (EPBT): the time it takes for a PV module to generate energy equal to the amount used in its production [8]. Recent study shows that thin-film cells have an EPBT that is less than half that of monocrystalline Si (2.7 years) even with lower PV efficiencies [9].

1.2 Amorphous Silicon Solar Cells

The most popular and well-studied material for thin-film solar cells is hydrogenated amorphous Si (a-Si:H), which is predominantly prepared by plasma enhanced chemical vapor deposition (PECVD) [10, 11]. In c-Si, every Si atom is tetrahedrally bonded to four neighboring Si atoms and this tetrahedral structure repeats over a large range, forming an ordered crystal lattice. Such long range order is not present in a-Si, where the atoms tend to form a continuous random network. Moreover, dangling bonds exist in the a-Si network, acting as defects in the amorphous matrix and causing undesired

electrical performance [12]. a-Si:H has a sufficiently low quantity of dangling bonds due to the passivation by H atoms, which are related to the well-known Staebler-Wronski effect (SWE) [13].

1.2.1 a-Si:H Film

Figure 1.1 shows the amorphous matrix of a-Si:H film, where the majority of Si-H_n bonds are monohydride bonds (Si-H) and dihydride bonds (Si-H_2). In particular, monohydrides are related to the hydrogen present in mono-/di-vacancies, which contributes to the short-range order (SRO) of the film. SRO is restricted to the region of the silicon network up to a distance of 3 $\mathring{A}$ from mono-/di-vacancies, and dictates the bond-angle distortion in amorphous network. The width of Raman transverse optical (TO) peak increases approximately linearly with the increase of bond-angle distortion, therefore could be used as the indicator of SRO [14]. On the other hand, dihydrides contribute to medium-range order (MRO) in an a-Si:H film, which extends up to 25 $\mathring{A}$ from mono-/di-vacancies. In other words, Si-H is related to the low defect density of the film while Si-H_2 is associated with high film nanoporosity. Generally, a-Si:H has H content of 5-15% [15].

a-Si:H has different band structure from c-Si, including broadened valence and conduction band tails and the presence of mid-gap defect states. The band tails are due to localized energy states inside the mobility edges resulting from the deviations in the bond length and angle [17, 18]. The mid-gap states are related to the presence of dangling bonds, which limit the transport properties of a-Si:H. a-Si:H has a higher band-gap (1.7 eV) than c-Si (1.1 eV), which means that it absorbs the visible part of the solar spectrum more strongly than the infrared portion.

Although a-Si:H has a higher absorption of light than crystalline cells, it has high

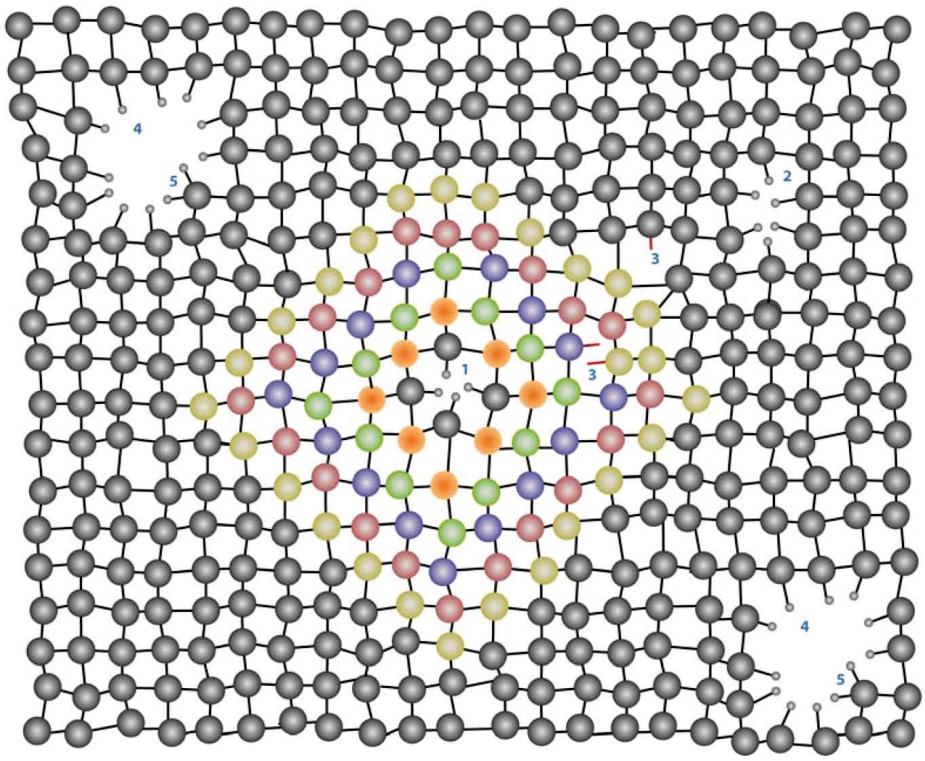

Figure 1.1: Schematic of an a-Si:H network, showing hydrogen in nano-vacancies and nano-voids, as well as silicon atoms within short-range order and medium-range order. 1: Monovacancy, 2: Divacancy, 3: Dangling bond, 4: Nanosized void, 5: Dihydrides [16].

inherent disorder and dangling bond concentration, causing low conductivity for charge carriers. The dangling bonds act as recombination centers which strongly reduce the carrier lifetime and further pin the Fermi energy level, making n-/p-type doping impossible. Although hydrogen is known to passivate dangling bonds, a high-quality film could still have defect density greater than 10^{15} cm^{-3} [19].

Another drawback of a-Si:H solar cells is the well-known Staebler-Wronski effect (SWE) [13], which relates to the effect of light-induced defect creation. With intense light exposure, the dark conductivity and photoconductivity of a-Si:H are reduced by several orders of magnitude. Furthermore, conversion efficiencies of single-junction a-Si:H cells degrade from 7-8% to less than 5% after several hours of light illumination. This degradation is found to be reversible: these properties can be recovered after annealing at temperatures higher than 150 °C. Several models have been developed to explain SWE, however this effect is still not fully understood. The mechanism of SWE is believed to be related with the main material properties of a-Si:H, such as disorder in the matrix, hydrogen bonding structure, and concentration of impurities. Currently, the most stabilized single-junction a-Si:H solar cells have highest efficiencies around 9.5% obtained on small areas [7].

1.2.2 PECVD Synthesis of a-Si:H Film

Radio frequency (rf) PECVD is now an important deposition method for the fabrication of a-Si:H. Compared to conventional CVD methods, PECVD allows lower process temperatures and provides flexible film properties. Additionally, varied film properties such as growth rate, density, and H content can be achieved by adjusting several plasma parameters, including plasma power density, deposition temperature, rf frequency, and argon or hydrogen gas dilution [20].

The role of plasma in the synthesis of a-Si:H is generalized into two aspects: (1) to dissociate silane into radicals that deposit onto the surface and (2) to produce energetic ions or atoms that transfer energy for dissociation. Silane (SiH_4) gas is a common precursor in PECVD synthesis, where SiH_4 molecules dissociate into radical species such as SiH_2, SiH_3, etc. SiH_3 species are believed to be the main precursor for high quality films [19]. The mechanism for PECVD can be divide into two stages: gas-phase dissociation process and plasma-surface interaction process. The main plasma reactions in the gas-phase including electron-molecule reactions, electron-neutral reactions, and ion-molecule reactions generate active species [21]:

$$SiH_4 + e \rightarrow SiH_n + (4-n)H + e \tag{1.1}$$

$$SiH_4 + e \rightarrow SiH_n^+ + (4-n)H + 2e \tag{1.2}$$

$$SiH_4 + e \rightarrow SiH_n^- + (4-n)H \tag{1.3}$$

$$H + SiH_4 \rightarrow SiH_3 + H_2 \tag{1.4}$$

$$SiH_4 + SiH_n \rightarrow Si_2H_{4+n} \tag{1.5}$$

$$SiH_n^+ + SiH_4 \rightarrow Si_2H_m^+ + (4+n-m)H \tag{1.6}$$

The abundance of SiH, SiH_2, SiH_3 species depends on which of the above reactions dominates, which can be further tuned by controlling the plasma parameters [22]. After the active species are formed in the gas-phase, SiH_n^+ positive ions are accelerated toward the grounded substrate as the source of ion bombardment in the plasma sheath region, while negative ions are confined within the plasma discharge [23]. The impacting ions create dangling bonds and abstract hydrogen from the growing surface. In a simple qualitative model, as the SiH_3 species arrive at the substrate surface, they can diffuse along the surface and react with only active sites or insert into the existing lattice,

filling the vacancies and leading to high-quality and smooth film growth. On the other hand, SiH_2 species can insert into the surface upon impaction at both active and passive sites, leading to void formation or lower quality films and increased surface roughness. Surface bombardment by energetic ions also plays an important role for the film growth mechanism. Increasing ion bombardment tends to make films denser and cause the film stress to become more compressive [24].

1.3 Microcrystalline Silicon Solar Cells

In order to increase solar cell production to the necessary levels, future solar cell technologies have to both reduce production costs and improve efficiencies. Therefore, the applications of high-quality, large-grain hydrogenated micro-crystalline silicon (μc-Si:H) thin film transistors and solar cells have become popular in recent years [25]. μc-Si:H films have better optoelectronic properties and greater stability under light exposure compared to a-Si:H films [26] [27]. One must produce μc-Si film with maximum possible grain size, ideally as large as the film thickness itself, to attain the stability and excellent electronic properties as well as the low manufacture cost.

1.3.1 Synthesis of μc-Si:H Film

The traditional PECVD process for μc-Si:H growth is limited by poor control over structural quality [25]. At present, the crystal grain size of μc-Si:H is too small for the technology to be comparable to the electronic quality of wafer-based single crystalline silicon. Different ways have been developed to produce large grain μc-Si:H from a-Si:H films, including solid-phase crystallization (SPC) [28–31], excimer-laser annealing (ELA) [32–34], and metal-induced crystallization (MIC) [35, 36]. The SPC mechanism involves

heating amorphous films for prolonged periods of time at sub-melting point temperatures until crystal grains emerge. The total annealing period is commonly characterized by three phases, including an incubation period, followed by a steady-state nucleation and grain growth of native crystals [37]. This process has been successful in producing films of higher quality than amorphous and as-deposited μc-Si:H films, but its manufacturing advantages are limited by the relatively high temperatures and long processing times required. ELA typically utilizes nanosecond pulses to crystallize a-Si:H films via a rapid melting and solidification process, but requires expensive additional equipment to implement, and is not very conducive to large-area device production. In MIC, a seeding agent such as nickel (Ni) is placed in a seed hole to initiate lateral crystallization around the Ni seed during a low-temperature solid-phase crystallization anneal. However, this approach has the disadvantage of introducing metal contamination into the silicon films, with deleterious effects on electronic transport.

1.3.2 Nanoseed Enhanced Crystallization

This thesis develops a new approach to manufacture μc-Si:H films, with a lower thermal budget and better control over microstructure, and larger grain sizes. This unique technique uses a low-pressure rf plasma reactor to synthesize silicon nanocrystals and embed these nanocrystals in a-Si:H matrix, where they serve as starting points for crystal grain growth upon thermal annealing.

This novel deposition process enables independently control over the amorphous matrix properties and crystal fraction of the film, as well as the size and density of embedded nanocrystals. During the recrystallization process, two important aspects need to be examined: maximization of crystal grain size and minimization of annealing time. By implanting nanocrystal seeds into the amorphous matrix, the incubation time

is expected to be eliminated, as the crystalline regions already exist in the film at the beginning stage of annealing. Furthermore, the micro-grain size in the final films can be controlled by adjusting initial seed concentrations.

Previous work has used similar ideas of implanting particles into a-Si:H matrix. Hakin *et al*. use micro-sized polycrystalline germanium (Ge) as seeds [38]. Uniform lateral crystallization is observed during annealing at 500 °C around the perimeter of the Ge seeds, as a result of tensile stress introduced by Ge seeding. However native nucleation was also observed at the boundary of a-Si:H film and glass substrate (Figure 1.2). This method produces fully crystallized film containing small grains with various orientations, resulting in poor film quality.

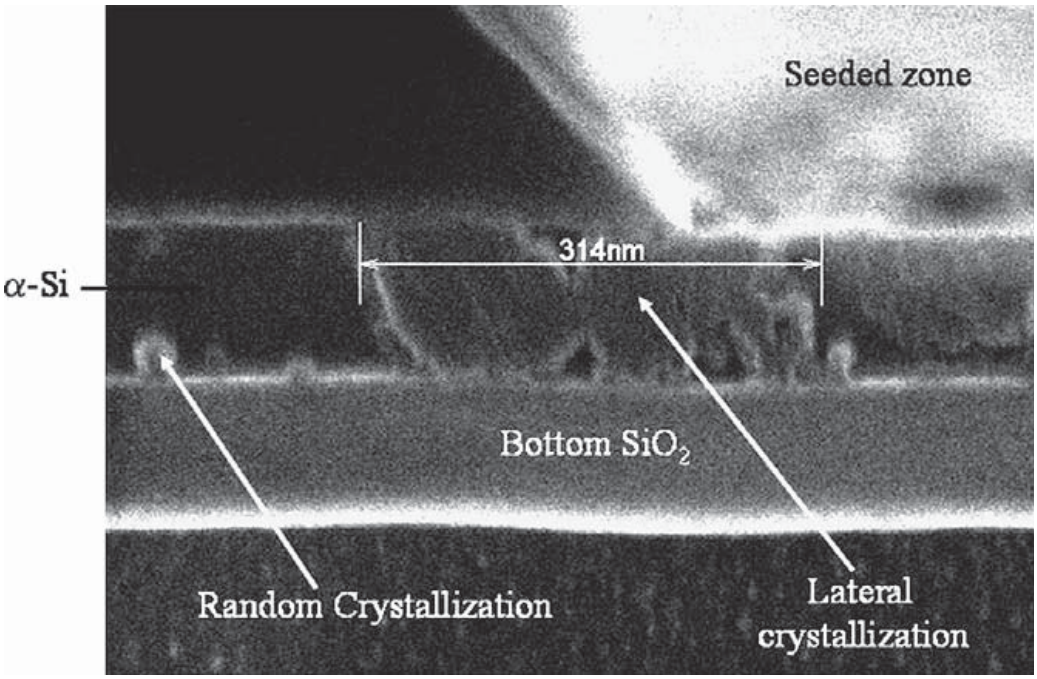

Figure 1.2: Cross-section SEM image of a-Si:H with Ge particle seeding, showing the lateral crystallization from the particle as well as native nucleation at film interface [38].

1.4 Thesis Layout

The goal of this work is to produce μc-Si:H from a-Si:H films with embedded Si nanocrystals, with the objective of reducing crystallization thermal budget and improving final grain size. The first chapter gives an overview of motivation and background of this work, as well as a review of previous similar work. Chapter 2 describes the characterization techniques used to analyze the properties of the as-deposited and mix-phase films. Chapter 3 introduces a "dual-plasma" deposition system and a layer-by-layer technique to embed Si nanocrystals into amorphous films. The nanoseed enhanced crystallization kinetics are studied in Chapter 4, revealing crystallization enhancement over intrinsic a-Si:H film. Chapter 5 discusses a newly observed crystallization event, named as "nanovoid". This chapter also explores the formation and propagation mechanism of the nanovoids. Chapter 6 then studies the factors controlling nanovoid enhanced crystallization, and provides solutions to independently control nanoseed growth and void propagation. Chapter 7 concludes the thesis and provides possible areas for future work.

Chapter 2

Characterization Techniques

2.1 Overview

This work aims to study the crystallization enhancement effect of amorphous silicon films with nanoparticle seeding. In order to understand the properties of the Si nanocrystals and a-Si:H films, as well as the crystallization kinetics of the seeded films, different kinds of characterization techniques are used, including Raman spectroscopy, heated-stage transmission electron microscopy (HSTEM), and forward recoil elastic spectrometry (FReS).

2.2 Raman Spectroscopy

Raman spectroscopy has been used as a sensitive technique for measuring the microstructure of amorphous silicon films before and after annealing, and is based on inelastic Raman scattering of monochromatic laser light [39]. In this work, Raman spectroscopy is used to analyze the crystallinity and the intrinsic stress of mixed-phase Si films.

The Raman scattering effect happens when laser light with a frequency of ν_0 incident on a sample then excites the molecule from the ground state to a virtual energy state. The molecule emits a photon when it relaxes. The energy difference between the original ground state and the excited state causes a shift (ν_m) of the emitted photon frequency from the incident frequency ($\nu_0 \pm \nu_m$). On the other hand, if the molecule relaxes to the same ground state, it emits light with the same frequency ν_0. This type of elastic interaction is called as Rayleigh scattering. More than 99.99 % of all incident photons in Raman spectrometry undergo Rayleigh scattering, therefore spontaneous Raman scattering is very weak and is needed to be filtered out from intense Rayleigh background.

This study uses a Witec Alpha 300R confocal Raman microscope with a spectral range up to 4000 cm^{-1} and spectral resolution down to 0.02 cm^{-1}. Omnichrome Argon ion laser with a 514.5 nm excitation wavelength and a 50 mW maxima output power is used to excite vibrations. A simplified scheme of the confocal microscope is shown in Figure 2.1. The light source is focused with an objective lens onto the sample. The spatial extension of the spot on the sample is a function of wavelength. With a beam splitter, the image spot is also focused through a pinhole onto a detector. With the addition of an extra aperture between the detector and the splitter, only the signal from a particular depth of field around 500 nm is allowed to pass through. The depth of field is typically larger than the Si film thickness, around 100 nm.

The laser beam in Raman measurements can cause local bulk heating of the investigated area, causing a peak shift similar to the effect of tensile stress [40]. On the other hand, the locally heated region expands thermally and exhibits compressive stress from the surrounding cold material, which partially compensates the first effect. As such,

the laser power should not exceed 2.5 mW to keep the tensile stress due to local heating below 0.01 cm^{-1} [74]. Also the integration time should be long enough to provide sufficient signal to noise (S/N) ratio for accurate fitting of the Raman peaks.

A typical Raman spectrum of amorphous Si film is shown in Figure 2.2 (a). It is composed of four distinct broad bands at about 180 cm^{-1}, 315 cm^{-1}, 400cm^{-1} and 480 cm^{-1}, associated with longitudinal acoustic (LA), longitudinal optic (LO), transverse acoustic (TA) and transverse optic (TO) modes, respectively. In comparison, the Raman spectrum of μc-Si film is shown in Figure 2.2 (b), which features a dominant sharp peak at around 518 cm^{-1} corresponding to the TO mode for bulk crystalline Si. The full width at half maximum (FWHM) of the crystalline Si TO peak is an indication of μc-Si quality, where an increasing value is related to the reduction of crystal grain size [41]. Additionally, the weak peak around 500-505 cm^{-1} is attributed to strained bonds at grain boundaries [42].

All the amorphous (TO, LO, LA, TA) and crystalline (TO and GB) components of the spectrum must be distinguished to calculate the volumetric crystalline fraction. In this work, a fitting software XPSPEAK41 is used to fit the Gaussian peaks. The following fitting techniques are adopted to improve the fitting efficiency and accuracy [41]. Before fitting the annealed μc-Si:H spectrum, a control sample of as-deposited amorphous film from the same batch is analyzed. Its amorphous LA, LO, TA and TO peak locations are then held constant for the following calculation of annealed samples, however the FWHM and intensity of those modes are allowed to vary. By fixing the position of amorphous bands, the mixed-phase samples are fit by only adding the crystalline peak around 520 cm^{-1} and grain boundary peak near 500-505 cm^{-1} with Lorentz curves. This significantly reduce the fitting complexity. The fitting iteration is stopped once a set tolerance is reached.

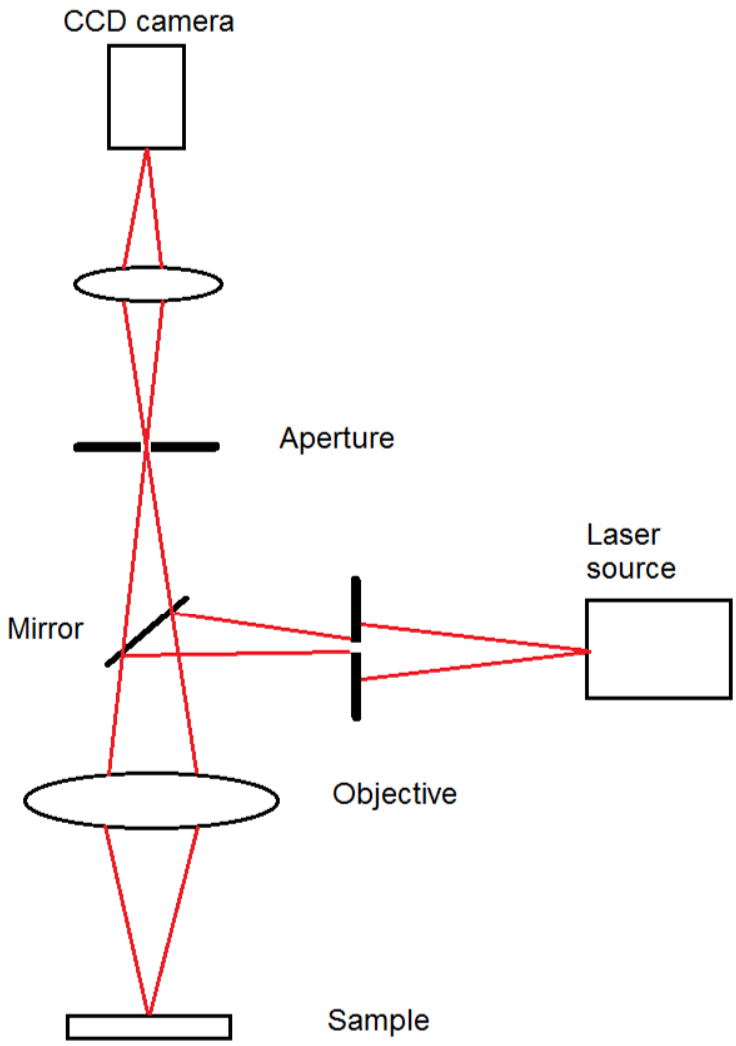

Figure 2.1: Simplified scheme for the reflective confocal microscope.

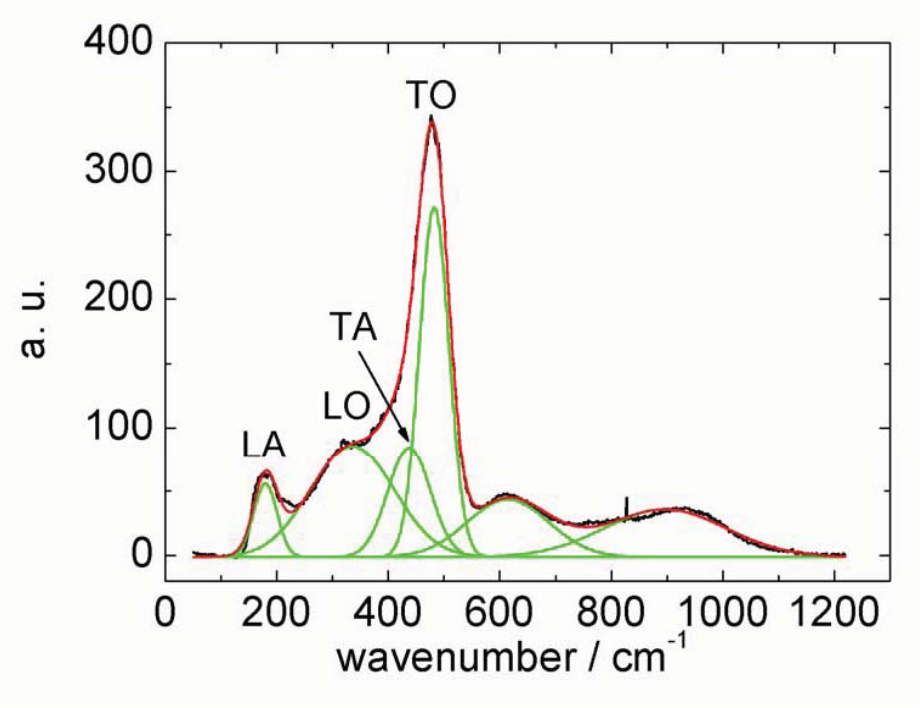

(a)

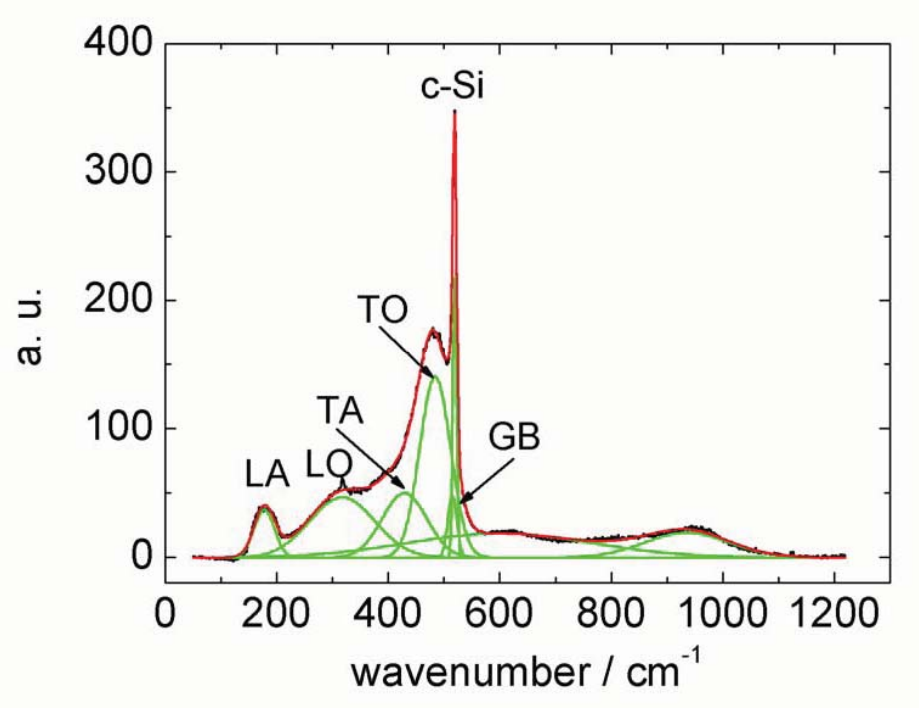

(b)

Figure 2.2: Raman spectrum of a-Si:H film (a) and μc-Si:H film (b), indicating amorphous peaks, as well as crystalline and grain boundary peaks.

Raman crystalline fraction is then calculated by comparing the areas underneath the amorphous and crystalline Si peaks as:

$$\chi_c = \frac{I_{crystalline}}{I_{crystalline} + \beta I_{amorphous}} \tag{2.1}$$

χ_c is the volumetric crystalline fraction. $I_{crystalline}$ is the area underneath crystalline peak at 520 cm^{-1} and grain boundary peak near 500-505 cm^{-1}, and $I_{amorphous}$ is the area underneath amorphous TO mode at 480 cm^{-1}. β is a correction factor that describes the ratio of the Raman scattering cross sections of amorphous and crystalline Si, with a typical value in the range of 0.1-1.9 [43]. This work is more interested in comparing the relative crystallinity instead of the absolute value during furnace annealing. Therefore it is acceptable to fix the value of β at 1 for simplicity of calculation.

2.3 Heated-stage TEM

Transmission electron microscopy (TEM) has been developed to image at significantly higher resolutions than light microscopy, where a beam of electrons is transmitted inside a column at ultra-high vacuum, interacting with an ultra-thin sample specimen. The transmitted electrons are then focused into a charge-coupled device (CCD) camera to form an image. A schematic for TEM is shown in Figure 2.3.

This work uses an FEI Tecnai T12 microscope combined with a Gatan 652 double-tilt heated-stage holder to monitor the *in-situ* crystallization mechanism of seeded a-Si:H films. Figure 2.4 shows the structure of the heated stage holder. To conduct *in-situ* heating experiments, a-Si films are deposited on top of molybdenum TEM grids coated with a thin carbon layer less than 10 nm. The specimen is then sandwiched between two tantalum washers and fixed by a hex ring inside the furnace of the holder, where

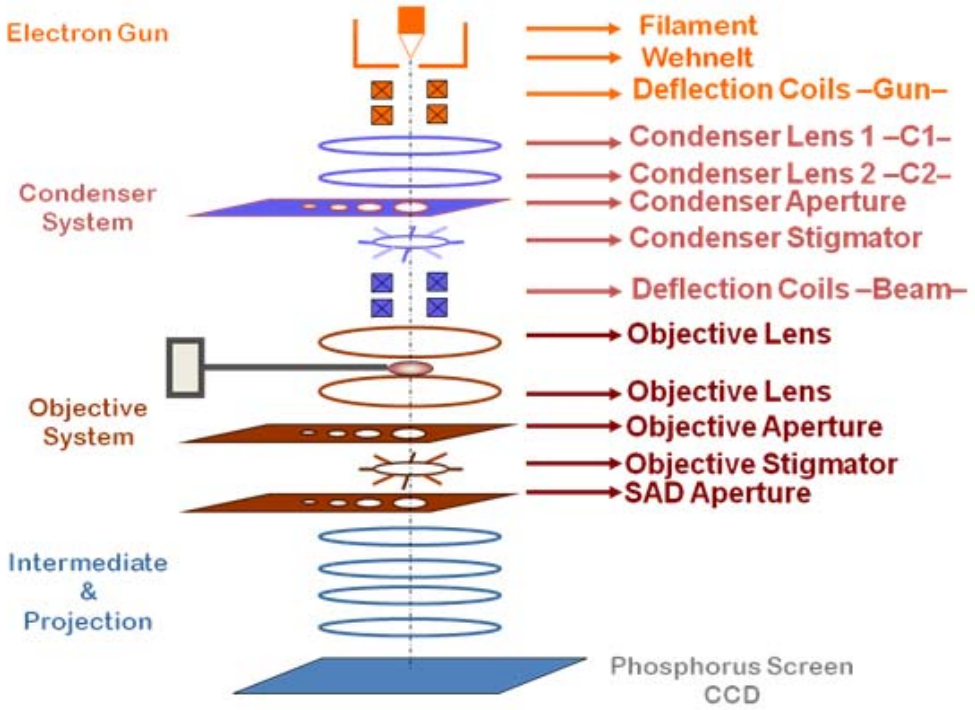

Figure 2.3: Simplified scheme of the transmission electron microscopy. (Courtesy of Ozan Ugurlu)

temperature is monitored by a thermocouple. A water recirculation unit is connected to the holder during the heating process to stabilize temperature and reduce specimen drift by maintaining a constant heat sink. A Keithley 2612A power supply powers the holder and the temperature controller. A threshold voltage is set to around 3.7 V and only current is adjusted to control temperature with the thermocouple feedback, to prevent overshooting of the temperature during annealing in case a current spike happens. The relationship between the applied current and the specimen temperature is plotted in Figure 2.5. With a typical annealing temperature of 600-650 °C, the corresponding current has a value of 400-450 mA, and output power is 1.8-2.1 W.

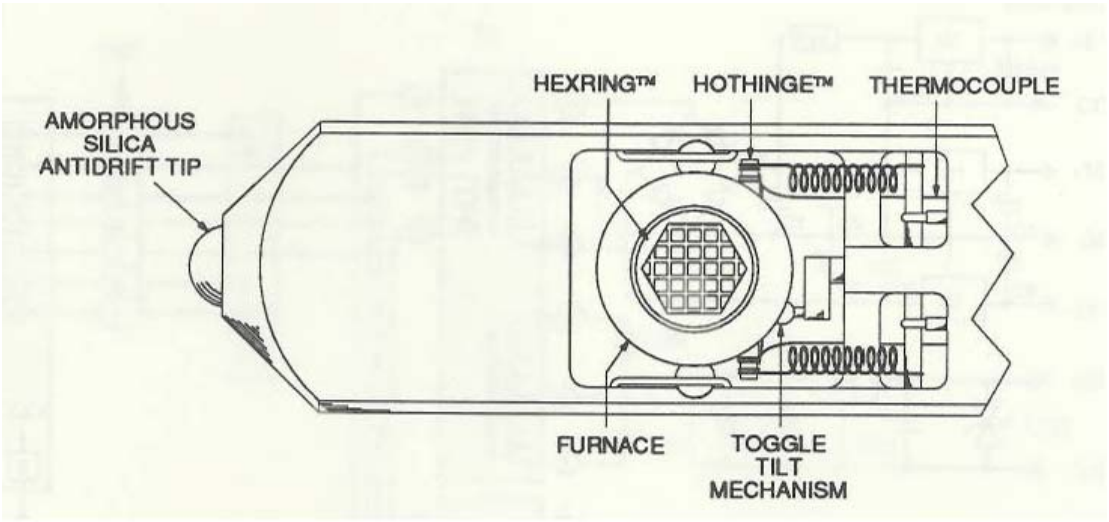

Figure 2.4: Sketch of front furnace portion of heated stage holder. (From manual of Gatan 652 double-tilt heated-stage holder)

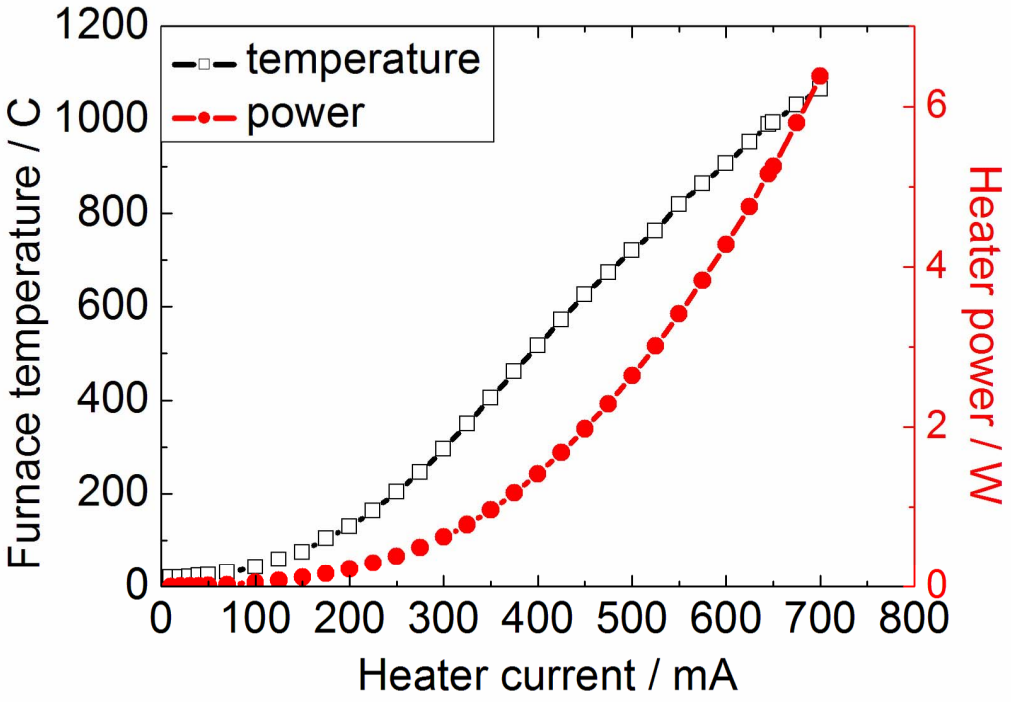

Figure 2.5: Plot of temperature and power of heated stage holder as a function of applied current of power supply.

After the sample is loaded inside the TEM high vacuum column, the beam is aligned to focus on the edge of the specimen, where the temperature is closer to the furnace temperature. The sample is slowly heated to the desired annealing temperature at a rate of around 20 °C/min. Time-series TEM images are recorded either by manual capture every 5 min, or automatic imaging with a rate of 2-6 images per minute. Selected area electron diffraction (SAED) pattern is a strong tool to study the crystal structure of Si films. The periodic structure of crystals scatters the electrons in a symmetric way, and different crystal lattice planes correspond to different bright spots in the diffraction pattern. Therefore, diffraction pattern of thin-film Si provides information of crystallinity as well as the crystal orientation.

In this work, HSTEM is employed to monitor the real time crystallization events and exploit the mechanism of void propagation, which will be discussed in detail in the following chapters. ImageJ software is used to process the time-series TEM images and measure the void displacement between successive images: ImageJ blends two TEM images with alignment of certain fixed points, and the displacement is measured as the distance between the center points of void tails.

2.4 Forward Recoil Elastic Spectrometry

Forward recoil elastic spectrometry (FReS) is an ion beam technique used to non-destructively measure the hydrogen concentration of a solid, which is a derivation of Rutherford Backscattering Spectroscopy (RBS) [44, 45]. In FRES, a beam of energetic helium (He) ions impinges on the sample throughout the film depth, and H atoms are scattered in the forward direction, passing through a layer of stopping foil and entering the detector. The recoiled H atoms will experience energy loss when travelling through the film, yielding the depth of the scattering event (Figure 2.6).

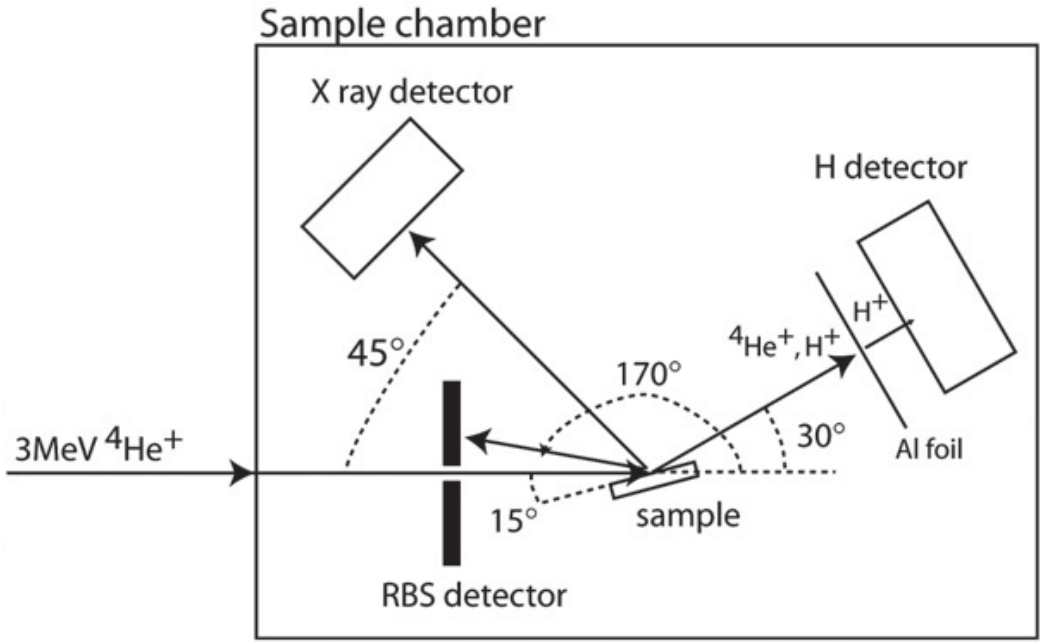

Figure 2.6: Principle of forward recoil elastic spectrometry [46].

This work uses an ion beam system equipped with a MAS 1700 pelletron tandem ion accelerator (5SDH) and a charge exchange RF plasma source. The ion detector is fixed at 165 degrees for RBS measurement and 30 degrees for FReS measurement. One common method to measure the H content is to compare the FReS spectrum of a-Si:H with that of mica film, which has chemical formula of $KAl_3Si_3O_{12}H_2Fe(tr)Ba(tr)$ and fixed H content of 9.5%. Therefore, by comparing the peak height of mica spectrum, h_{mica}, and silicon film, $h_{silicon}$, the H content in a-Si:H is calculated as:

$$C_H = \frac{h_{silicon}}{h_{mica}} \times 9.5\% \tag{2.2}$$

Figure 2.7 gives an example of the FReS spectrum of a-Si:H films and mica sample. This method generates certain error, as mica has much lower stopping power, the energy lost by each He ion per unit depth as it penetrates the solid. The reason is that the average number of electrons (which produce energy loss upon excitation) per atom in mica is lower, as around half of the mica atoms are oxygen, a lower atomic number element. This means that the energetic width of a given channel of data in the mica spectrum corresponds to a thicker depth slice, thus yielding greater signal in measuring H content for mica and predicting lower H content in Si films.

This can be compensated for by using Hypra software, which fits the FReS and RBS spectrum simultaneously. A layered model of a-Si:H is built in Hypra, including a bottom layer of thick Corning glass and a top layer of amorphous Si film of unknown thickness. The chemical formula of Corning 1737 glass is measured in advance as $Si_{0.9}O_{3.2}Ca_{0.06}Sr_{0.015}Sb_{0.012}Ba_{0.05}Al_{0.15}$ and the a-Si:H is assumed as SiH_n. The stoichiometric coefficient n, as well as the thickness of a-Si:H film, are simulated simultaneously with the RBS and FReS spectrum in Hypra. Such method results in a H content of 9-15% in this study.

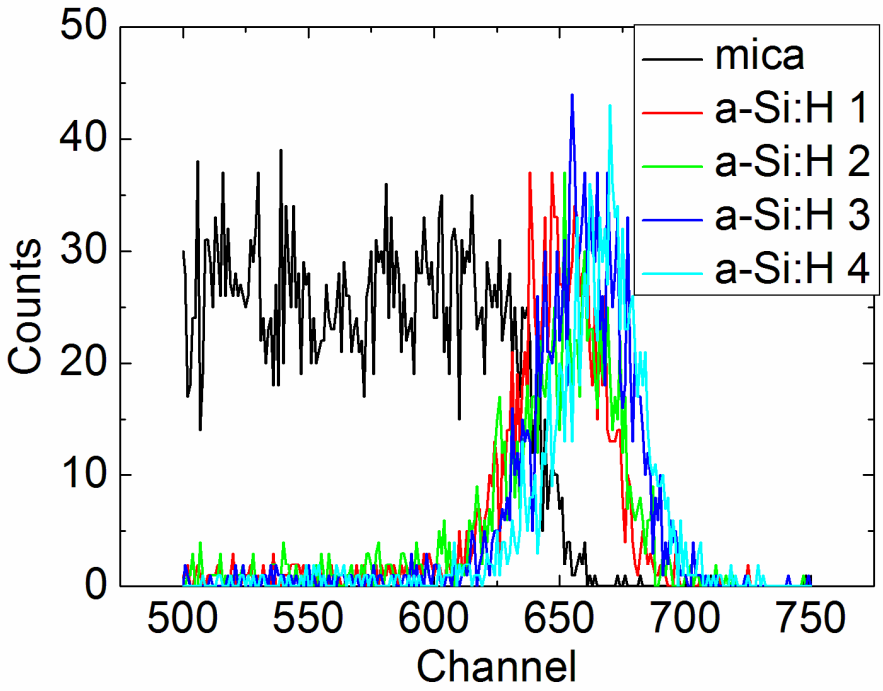

Figure 2.7: FReS spectrum of a-Si:H films and a mica sample. H content of Si films is measured by comparison of peak heights with mica film.

Chapter 3

Experiment Setup

3.1 Overview

This work focuses on reducing the recrystallization time while controlling the grain structure of μc-Si:H films in which silicon nanocrystals are embedded as nucleation seeds. This chapter introduces the experimental setup used to synthesize such film structures, called a "dual plasma" system, as well as the layer-by-layer film structure. The introduction of the double plasma sources enables independent control of properties of a-Si:H films as well as nanocrystal size and density.

3.2 Nanoparticle Synthesis

This work uses a "dual plasma" system to synthesize amorphous silicon film with silicon nanocrystal seeding, with the schematic shown in Figure 3.1. Silicon nanoparticles are synthesized on top of the system in a quartz tube reactor of 4.7 cm inner diameter and 23 cm length. Rf power at 13.56 MHz, fed into the quartz tube though a copper ring electrode, generates the plasma. An orifice with 1-2 mm diameter downstream of

the particle plasma serves as the grounded electrode. The distance between the ring electrode and the grounded electrode is 6-7 inches. A shutter 2 inches downstream of the orifice allows manual control over particle flow. In a typical operation, a shutter open time of 2-3 s results in a particle density in the film of 4 particle per μm^2. Silane diluted with 95% helium is used as precursor gas and argon as the buffer and purge gas, both controlled by mass-flow controllers [47].

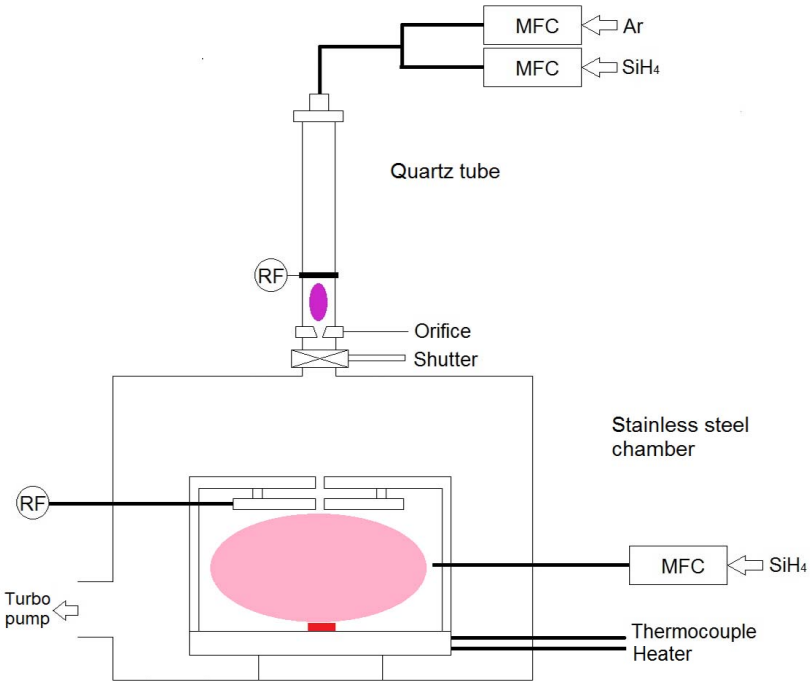

Figure 3.1: The system sketch of "dual plasma" system, composed of a particle plasma on top and a film plamsa on bottom.

Applying rf power to the ring electrode leads to a dim plasma region upstream of the ring electrode and a bright plasma region between the ring electrode and the downstream orifice. It is believed that particle nucleation happens in the upstream

region, while the downstream plasma could operate in diffused mode or filamentary mode. In a diffused mode plasma, a uniform plasma region is observed and likely caused by capacitive coupling of the copper electrode to the orifice. Particles generated in the diffused plasma typically have residence time as short as 1 s or less. With such short time exposed to the plasma, the particles tend to form agglomerates or a spherical shape. The second plasma mode is the filamentary mode where the discharge has an unstable and flickering appearance. High-speed photography has revealed that the filamentary discharge is composed of a string of 15-20 globular discharges with 3-5 mm length, separated by 1-2 mm dark region, rotating with a frequency about 150 Hz [48]. The rotation of discharge is not always periodic, as the filaments sometimes change the direction of rotation or show random jumps. As the nanoparticles move following the rotational filaments, their residence time is dramatically increased, up to several seconds, leading to the shape transformation toward the cubic shape. The formation of the cubic shape is believed to be the effect of surface diffusion caused by heat release in the electron-ion recombination processes at the particle surface, as the particle surface temperature exceeds the gas temperature by around 200-300 K [49].

Different types of silicon nanoparticles are synthesized by varying plasma parameters. The key factor in controlling particle shape is the residence time, the time when nanoparticles are exposed to the plasma discharge. Extended residence time is expected to favor the formation of cubic particles. The residence time of nanoparticle can be adjusted by the precursor gas flow rate and orifice size, which control the upstream and downstream pressure of the orifice. A total flow rate of 6-7 sccm leads to the upstream pressure inside the particle reactor during plasma operation at 1.5-2.0 Torr, compared to the relatively high vacuum, around 0.1 Pa, inside the downstream chamber. Such high pressure drops across the orifice generate choked gas flow at the exit of the orifice,

and a supersonic jet forms and accelerates the expanding particle beam towards the substrate at a velocity of around 300 m/s [50]. The input rf power density controls the crystallinity of nanoparticles, as power lower than 50 W is proved to produce amorphous nanoparticles.

Figure 3.2-3.4 shows the TEM images of various silicon nanoparticles, by controlling plasma parameters such as gas flow rate, orifice size, rf power and plasma mode. In Figure 3.2 (a), monodispersed single cubic crystals with averaged edge lengths of 25 nm are synthesized with the condition of 3 sccm Ar, 4 sccm SiH_4/He, 130-140 W rf power, orifice with 1 mm diameter, and a filamentary plasma mode. High resolution TEM images indicate that the cubic particles are terminated with silicon (100) crystal facets, which happen to be the minimum energy surface for hydrogen terminated silicon surface, dictated in Figure 3.2 (b). The cubic shape is thus the equilibrium shape for silicon nanoparticles with hydrogen terminated surfaces. Furthermore, the (100) silicon surface is a fast growing surface since it needs at most 2 adatoms to grow a new layer of atoms on it.

In comparison, Figure 3.3 (a) shows spherical (or multi-faceted) nanocrystals synthesized with 2 sccm Ar, 6 sccm SiH_4/He, 130 W rf power, 1 mm orifice, and diffused plasma mode. Without the existence of rotating filaments, the residence time of nanoparticles is reduced to less than 1 s. As a result, the nanoparticles form spherical shape due to insufficient surface diffusion process which impedes the restructuring of nanoparticles into cubic shape. Comparing to the exclusively (100) terminated cubic particles, spheres have multiple facet directions on a surface, implying anisotropic growth speed during early stage of crystallization. The size distribution of spherical particles in Figure 3.3 (b) reveals a slightly lower mean particle size of 17 nm and broader dispersity compared to the cubic ones, as particles with size larger than 50 nm are occasionally observed.

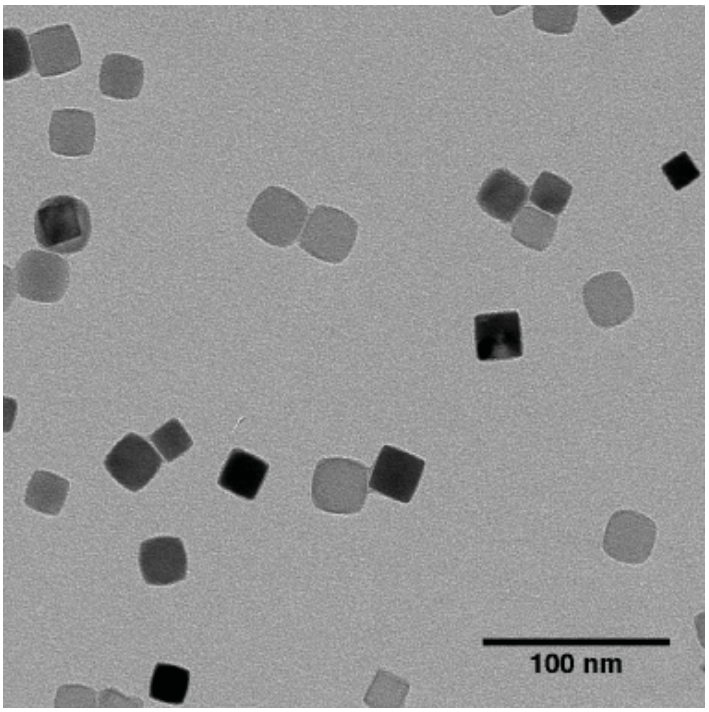

(a)

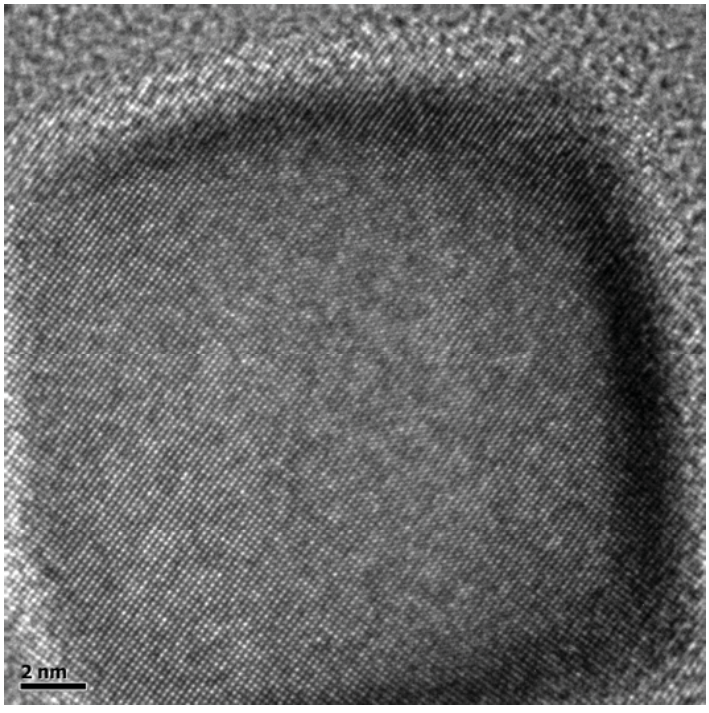

(b)

Figure 3.2: Bright field TEM images of cubic Si nanocrystals. (a) Top view image. (b) High resolution image showing crystal lattice.

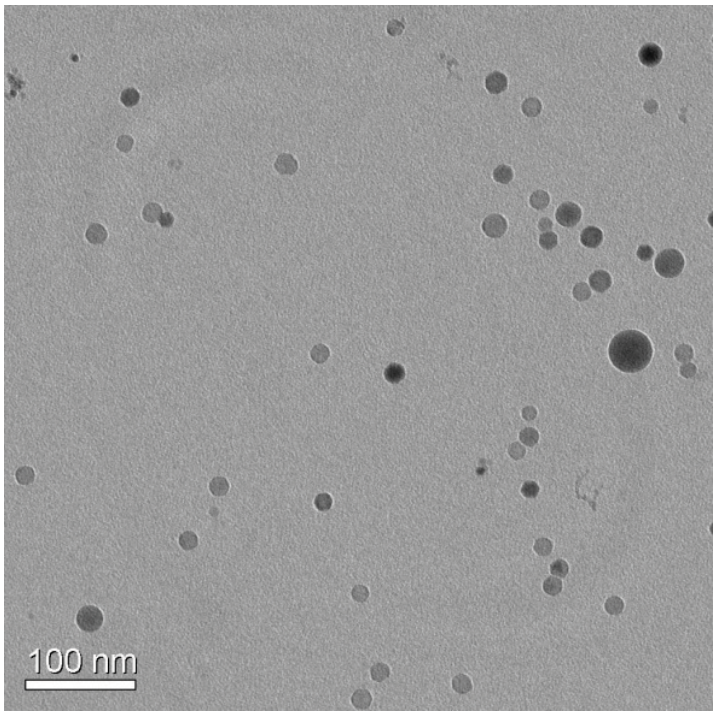

(a)

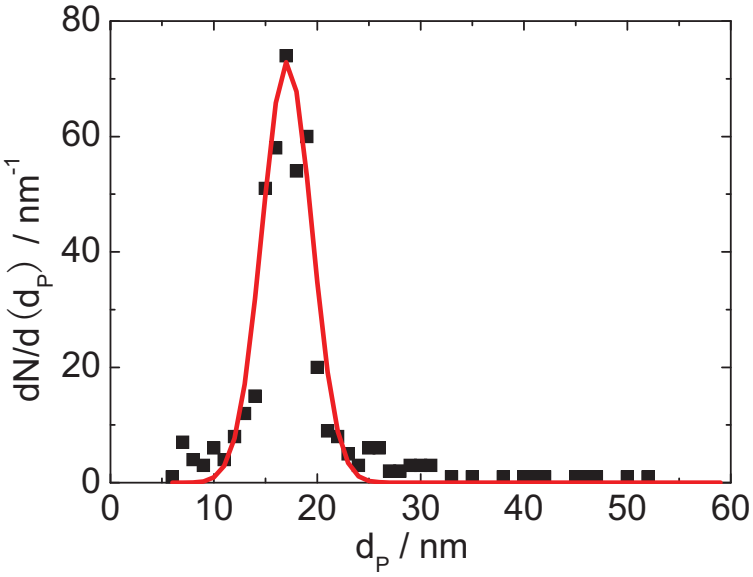

(b)

Figure 3.3: Bright field TEM images of spherical Si nanocrystals. (a) Top view image. (b) Plot of particle size distribution indicates a mean diameter of 17.08 nm and standard deviation of 4.79 nm.

While decreasing the rf power to below 20 W and with 3 sccm Ar, 4 sccm SiH_4/He, 1 mm orifice, and diffused plasma mode, amorphous Si nanoparticles are synthesized due to insufficient heating of atomic clusters to induce phase change [51]. Figure 3.4 (a) shows that amorphous particles have size below 10 nm. Each 8-10 nanoparticles tend to form agglomerates and the surface area of the agglomerates is very close to that of the cubic or spherical nanocrystals. The diffraction pattern image in 3.4 (b) confirms the same amorphous nature of the agglomerates with the bulk film.

3.3 Amorphous Silicom Film Synthesis

The main vacuum chamber in Figure 3.1 is used to the deposit amorphous silicon film. The dimension of the stainless steel chamber is approximately 25 cm in height and 50 cm in diameter. The chamber is always kept under high vacuum at $10^{-7} - 10^{-8}$ Torr to avoid any potential oxygen and hydrocarbon contamination. A turbomolecular pump is connected to the side of the chamber through a manually controlled gate valve, which is also used to adjust the pressure during film growth. A roughing pump backs the turbo pump at a constant pressure level of 100-400 mTorr with a small nitrogen gas flow, which is higher than the estimated pump oil vapor pressure of 100 mTorr. A transfer chamber with a manual push rod attached at the other side of the main chamber enables loading and unloading of substrates without breaking the vacuum. A stainless steel plate is attached to the front tip of the push rod and could be loaded or unloaded by manual rotation. The push rod is well adjusted to make sure that its front plate is at the same level of the bottom plate of the plasma box. A bypass line connecting the particle reactor and the main chamber allows for rapid evacuation and purging of the particle reactor.

The a-Si:H film is grown in the PECVD box inside the main chamber, which is

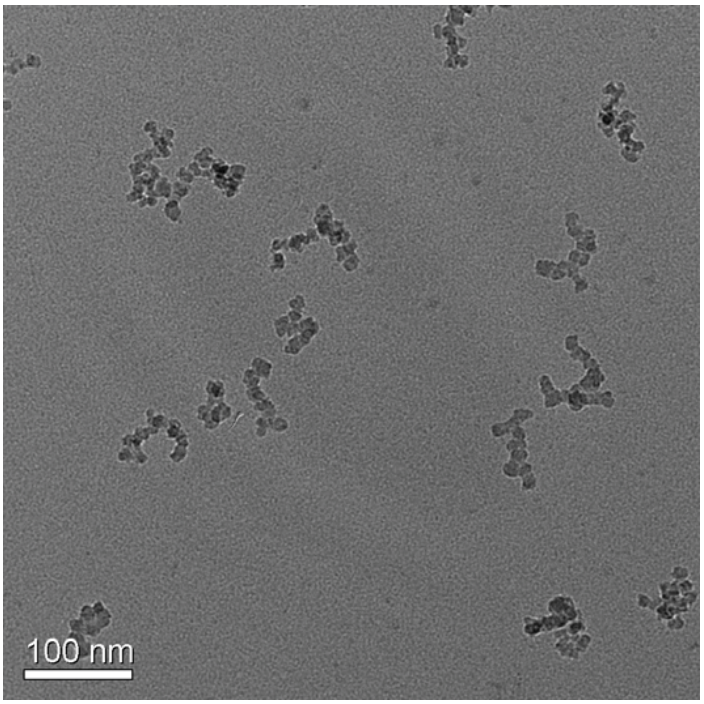

(a)

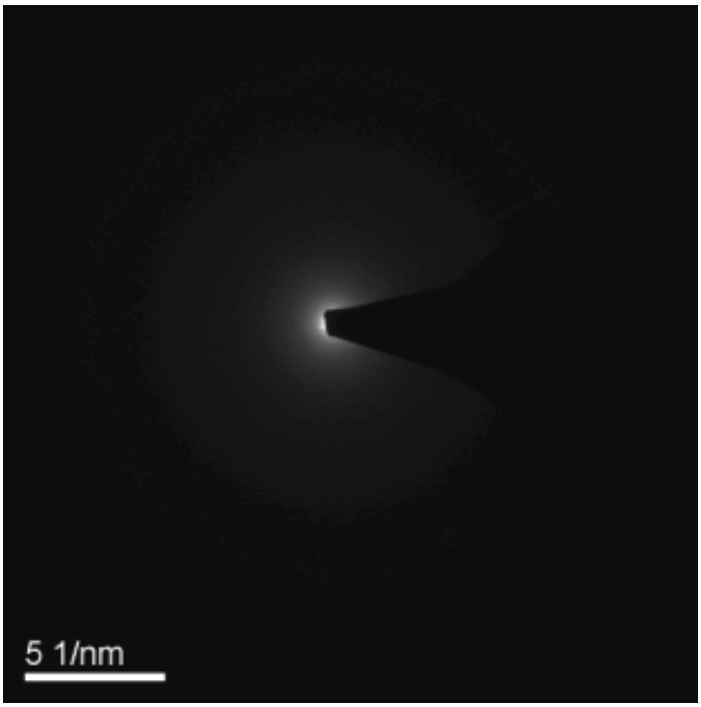

(b)

Figure 3.4: TEM images of amorphous Si nanoparticles. (a) Top view image. (b) Diffraction pattern indicates the amorphous structure.

composed of a stainless steel electrode 4 inches in diameter and powered by rf power, and a stainless steel box 6 inches in outer diameter which is grounded together with the chamber walls. A voltage-current probe connected to the rf circuit enables real-time monitoring of actual power absorbed by the film plasma, which suggests that usually only 1/3-1/2 of the total applied rf power is converted to energy in the plasma. The bottom plate of the plasma box has two cartridge heating elements embedded to heat up the substrate with a heater controller. A thermocouple is also connected to the plate to monitor the temperature. The distance between the rf powered electrode and bottom grounded electrode is 5 cm. A 3/4 inch hole at the top of box allows the particle jet to reach the bottom electrode and the holes with same size in the sidewall allow gas circulation in the box during deposition.

The standard operation for film deposition uses a silane flow rate of 50 sccm, a deposition temperature of 250 °C, and a chamber pressure at 100-400 mTorr. The PECVD plasma is uniformly distributed inside the PECVD box and shows an intense sheath region around the grounded substrate and the electrode. However, there is certain plasma coupling to the holes on top of the box and at the sidewall, as well as the thermocouple. Matching of rf circuit can be tuned to minimize the plasma loss and improve the rf coupling. Figure 3.5 (a) shows the continuous as-produced film with no cracks observed. Its thickness is directly measured from the cross section SEM image in Figure 3.5 (b), which indicates uniform thickness across micrometer length scale.

The film growth rate at the standard growth condition is around 20-80 Å/min, which is much lower than the industrial growth rate (50-500 Å/min) [52]. This is mainly due to the relatively low deposition pressure and rf power density. Efforts have been made to achieve higher growth rate by tuning the deposition power, deposition temperature, and applied rf frequency, which will be discussed in the following chapter.

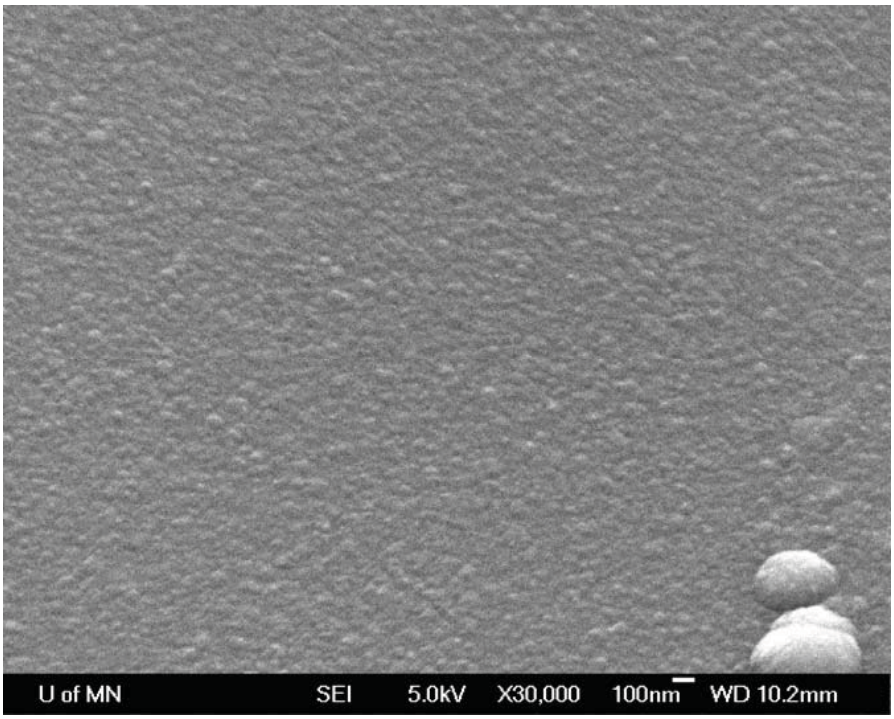

(a)

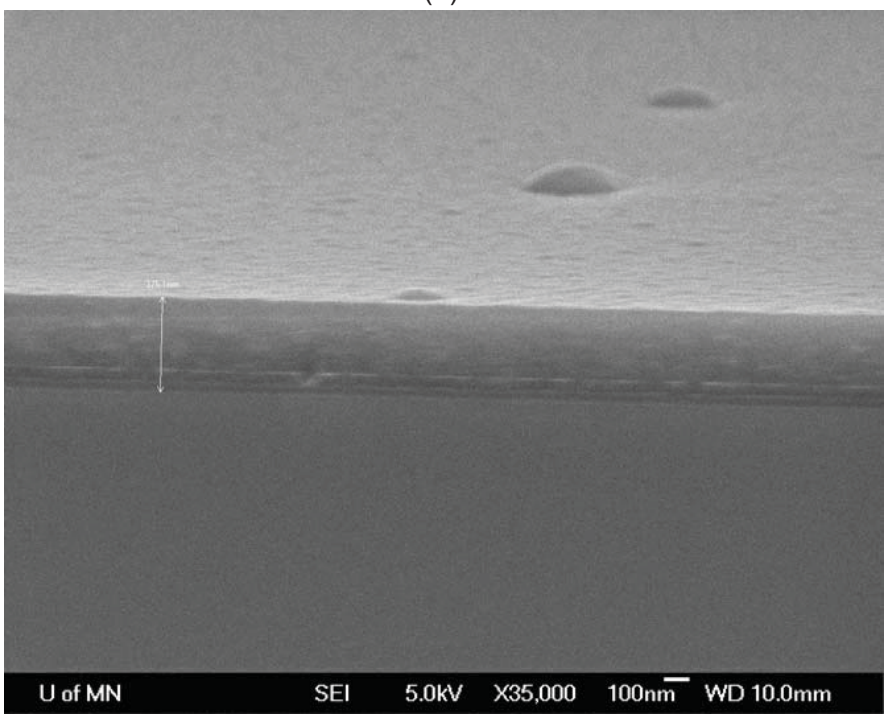

(b)

Figure 3.5: SEM images of amorphous Si films. (a) Top view image. (b) Cross section image.

3.4 Layered Structure Synthesis

This section briefly describes the method to synthesize the layer-by-layer seeded film structure by the dual plasma system introduced previously. A background pressure of $10^{-8} - 10^{-7}$ Torr is the prerequisite for any high-quality film deposition. An Ar cleaning plasma is run before every seeded film deposition experiment. Pure Ar gas with 40 sccm through the main chamber and 4 sccm through the particle reactor purges the system as well as gas supply lines for 4-5 min, following with Ar plasma in both the main chamber with applied rf power of 20 W and 100 mTorr pressure, and in the particle reactor with applied rf power of 100 W. Such a purging process helps improve the film quality by removing surface residue from the substrates and chamber walls. The samples are loaded into the main chamber through the transfer chamber after purging process. The transfer chamber is purged with Ar three times after each time its door is opened.

The film deposition method is described in Figure 3.6: a thin layer of a-Si:H film, typically around 20 nm, covers the glass or TEM grid substrates. The PECVD plasma is then extinguished and the chamber pressure is reduced to high vacuum of 10^{-6} Torr. Next, the upstream particle plasma is turned on to produce silicon nanoparticles and the shutter is opened after approximately 30 s in order to stabilize the plasma discharge, to expose the substrate to the particle beam for 2-5 s. In the last step, the particle discharge is extinguished and the film deposition process is repeated for another capping layer as thick as 80 nm.

Figure 3.7-3.9 shows the top-view TEM images of a-Si:H films seeded with various nanoparticles. The shaded region surrounding the particles is due to the thickness variation after embedding particles into the thick matrix (Figure 3.6). In Figure 3.9, the amorphous nanoparticles are invisible as both the particles and the film are amorphous materials.

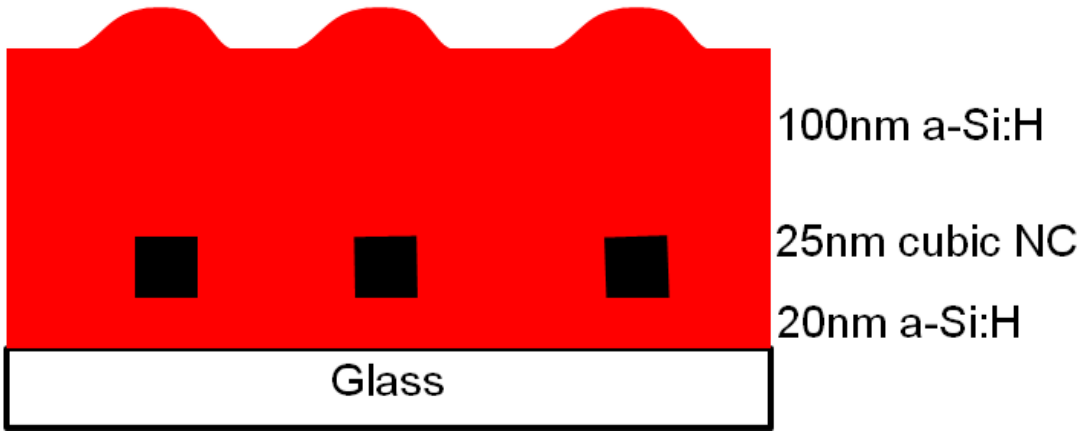

Figure 3.6: Sketch of layer-by-layer structure of seeded films.

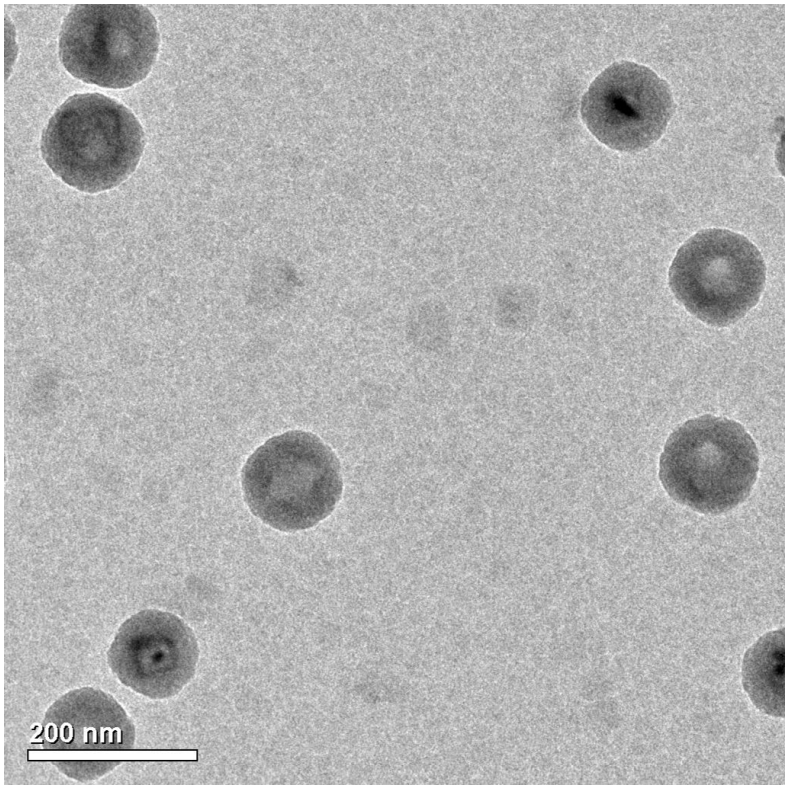

Figure 3.7: Bright field TEM image of a-Si:H film seeded with cubic nanocrystals.

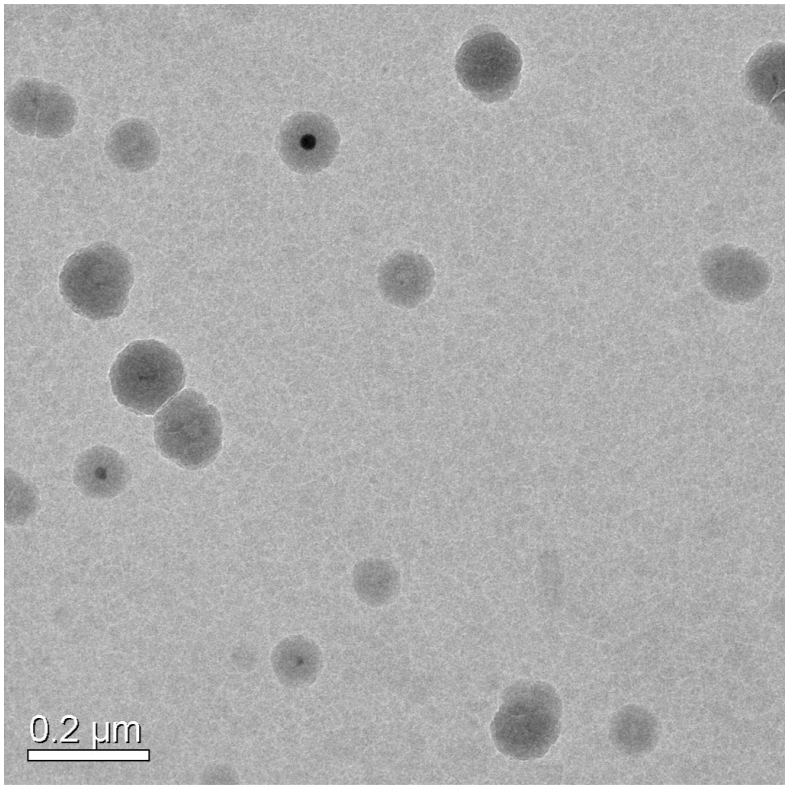

Figure 3.8: Bright field TEM image of a-Si:H film seeded with spherical nanocrystals.

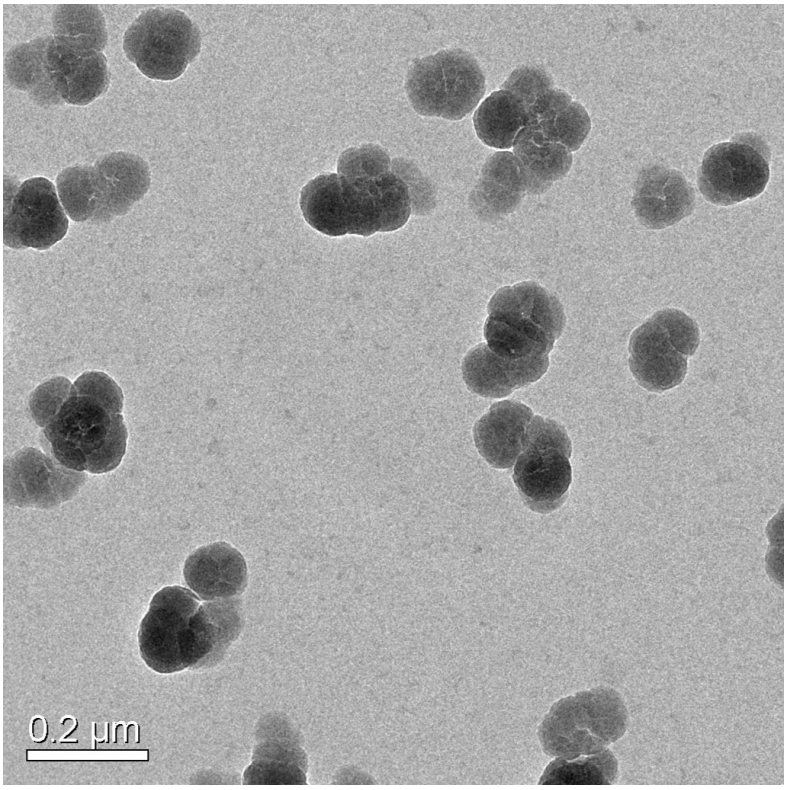

Figure 3.9: Bright field TEM image of a-Si:H film seeded with amorphous nanoparticles.

Chapter 4

Nanoseed Enhanced Crystallization

4.1 Overview

This chapter studies the macroscopic crystallization enhancement of a-Si:H films with nanoseed implantation, including the control of crystallization rate and grain structure. The amorphous incubation time is eliminated by embedding nanocrystal seeds into the amorphous matrix since the crystalline regions already exist inside the film at the beginning stage of annealing. Also, the grain size in the final film is improved by controlling the initial seed concentration. This chapter also shows that seeding of nanocrystals increases the short-range disorder of the amorphous matrix, which suppresses the solid-phase epitaxy of the seeds.

4.2 Crystallization Kinetics

Previous work has extensively studied the solid-phase crystallization behavior of amorphous silicon films, where the growth model was explained by the kink-like step at a crystalline-amorphous interface for thermal recrystallization [53, 54]. With the absence of an existing crystalline-amorphous interface, the phase transition occurs via random homogeneous nucleation of crystalline clusters. Upon annealing at high temperatures above 600 °C, the intrinsic amorphous silicon film naturally forms small crystalline clusters from rearranging bonds. Traditional crystallization theory argues that only clusters above a certain critical size continue to grow to large crystalline regions, a tendency which increases with initial cluster size [55]. This suggests that crystallization of nanocrystal seeded films is expected to be enhanced by the size of nanoseeds.

In studying the macroscopic crystallization kinetics, layered structure films are deposited on Corning 1737 glass substrates, annealed in a quartz furnace under nitrogen flow at controlled time interval and characterized by Raman spectroscopy at regular intervals. The interval length strongly depends on the annealing temperature, such as around 10 min at 650 °C and 40-60 min at 600 °C. All the seeded samples have the same film thickness of 120 nm as well as the control sample of unseeded Si film to obtain consistency, which are deposited under standard plasma operation condition with a deposition pressure of 100 mTorr, substrate temperature of 250 °C, applied rf power of 5 W, and SiH_4/He flow rate of 50 sccm. The varied seed density is manually controlled by the shutter and measured under TEM. Figure 4.1 indicates a linear increase of nanoseed density in the final film with extending the open time of the shutter. However the density is not accurately repeatable due to error arising from manual operation.

Figure 4.2 compares the Raman crystallinity growth of films containing single layers of nanoseeds at a concentration between 1 and 20 particle per μm^2 to films of equal

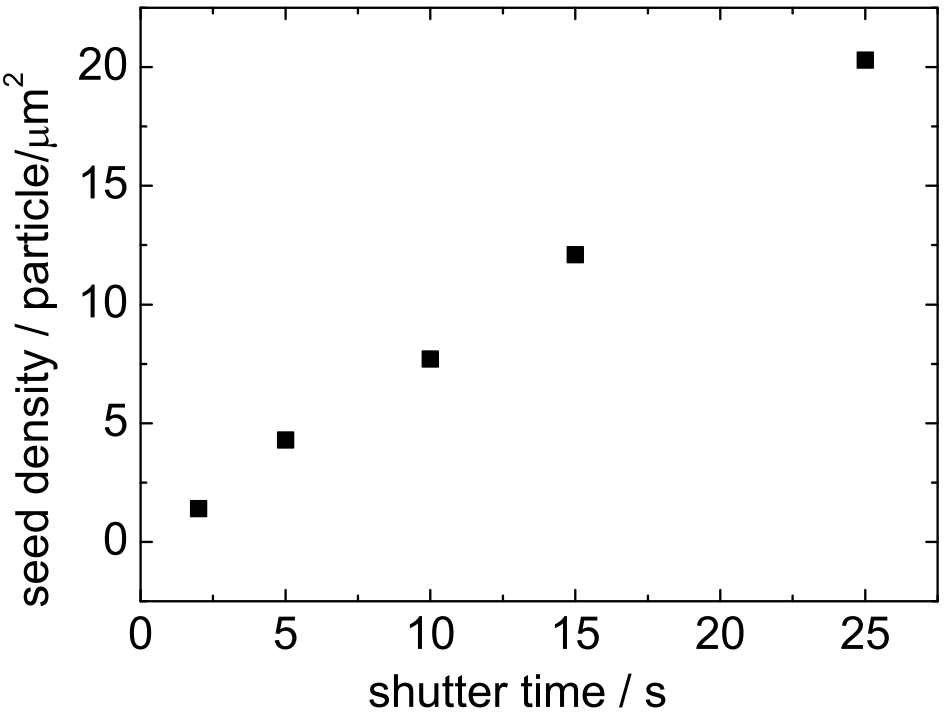

Figure 4.1: Nanoseed density in layered film as a function of shutter time.

thickness containing no seeds. The crystallinity is calculated from the comparison of areas of Si crystalline peak and amorphous Si TO peak. The yellow curve in Figure 4.2 shows the growth kinetics of intrinsic a-Si film without any nanoparticle seeding. As predicted by previous work, the growth of intrinsic amorphous silicon film has three distinct stages: an incubation period where native nucleation sites form, a rapid growth period in which nuclei grow epitaxially, and finally a saturation stage where the crystallization rate decreases as crystalline growth fronts interfere with each other, retarding their growth [53]. The incubation period is as long as 300 min, while the crystallization reaches saturation at a value around 0.7-0.8 after about 500 min, at which the film is considered to be "fully" crystallized, given the fact that there may exist amorphous regions between the boundary of grains and there may be error from the selection of Raman fitting coefficient β.

In comparison, the other colored curves in Figure 4.2 shows the crystallization of films with pre-existing nanoseeds. It is clear that the introduction of the seeds provides a substantial enhancement of crystallization over non-seeded films with full elimination of the amorphous incubation time. For example, the incubation period of unseeded film finishes at 300 min, while nearly all the seeded films reach full crystallization before the onset of growth occurs in their seedless counterparts. However, seeded films have a relatively lower grain growth rate (indicated by the slope of growth region) than unseeded films at early stage of crystallization (crystallinity less than 0.2). This is due to the fact that grain growth sites in unseeded films emerge in much greater numbers, whereas in seeded films the number of growth sites is fixed by the seed population.

Furthermore, it is interesting to observe that films with less seed density grow faster at early stage of crystallization and reach "fully" crystallization in shorter time, which is an additional advantage of the seeded structure because films seeded more sparsely

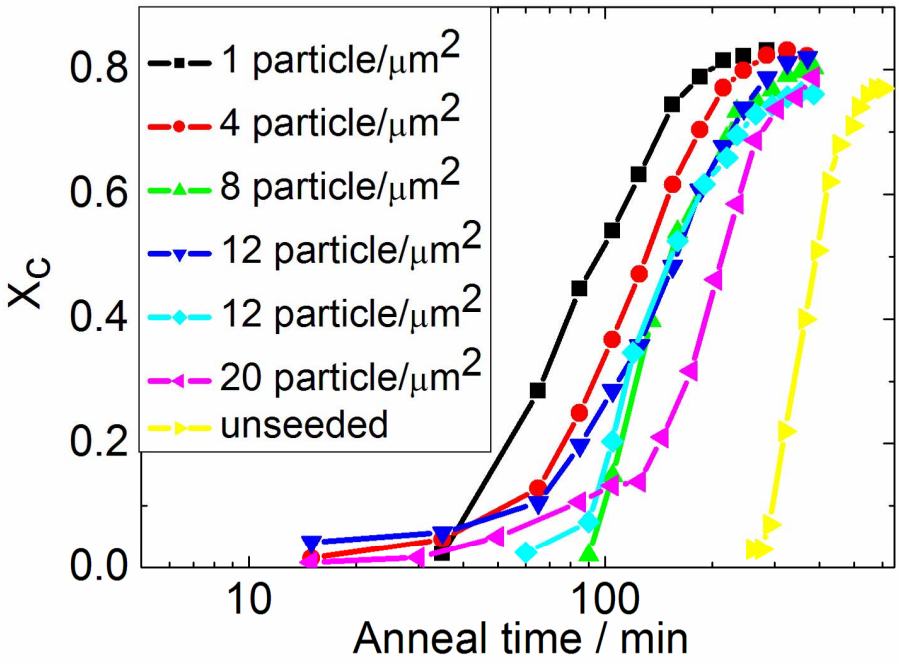

Figure 4.2: Time-series of Raman crystallinity of seeded and unseeded films annealed at 625 °C, indicating strong nanoseed enhanced crystallization over intrinsic a-Si:H film.

produce final microcrystalline film with larger grain sizes. This trend is explained as increasing short range disorder (SRD) of amorphous matrix due to greater seed inclusion. Figure 4.3 plots the half width at full maximum (HWFM) of a-Si Raman TO peak as a function of seed density, which dictates that the embedded seeds as crystalline structures increase the disorder of the amorphous matrix in the range of less than three layers of atoms near the seeds. The increased SRD is well-studied to hamper the solid phase epitaxy growth of the film [16]. Furthermore, there should exist an optimal value of nanoseed density (between 0 and 1 particle per μm^2), below which the crystallization rate would drop instead, due to the lack of pre-existing nucleation sites. However, it is difficult to achieve such low seed density by using a manually controlled shutter.

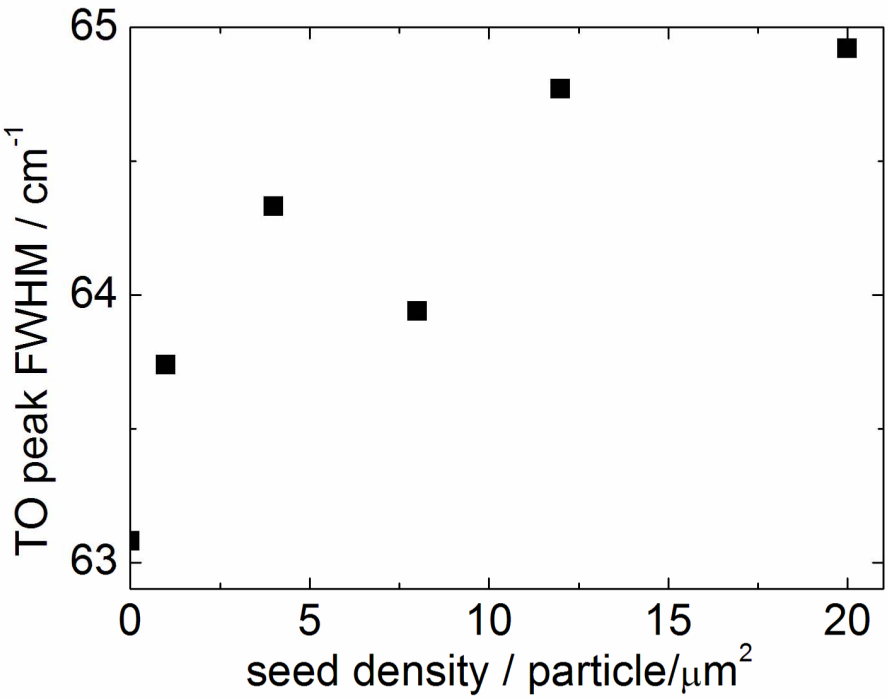

Figure 4.3: FWHM of a-Si TO peak of as-deposited seeded films with varied nanoseed density.

The effect of nanoseed density on the final grain size of "fully" crystallized films is studied in Figure 4.4. Since the grain size of the final film is in the order of tens of nanometers, it is difficult to measure it with X-ray diffraction (XRD). An alternative way to measure the relative grain size between films is to calculate the FWHM of the Raman crystalline peak, which decreases with improving crystal grains indicating more ordered film structure [56]. In Figure 4.4, increasing the seed density in a layered film leads to increased FWHM of the Raman crystalline peak, indicating reduced final grain size. It is noticeable that even films with the highest seed density of 20 particle per μm^2 still have final grain sizes larger than the corresponding unseeded film. Therefore, the introduction of nanoseeds in the amorphous matrix not only enhances crystallization, but also improves grain size of final crystallized film, as lower density of nucleation sites is present in the as-deposited film.

The improved grain size of seeded films enhances the electronic transport properties of "fully" crystallized films. All the films are deposited on glass substrates and are patterned with a chromium contact and I-V characteristics are taken to acquire dark conductivity values at several locations in each film. Figure 4.5 shows the dark conductivity of seeded and unseeded films, depicting a trend in which conductivity decreases with increasing initial seed density. Samples with lower initial seed density have fewer but larger grains, and thus obtain larger electrical conductivities with smaller grain boundary regions. It is interesting to note that the standard deviation in conductivity for films with lower seed densities exhibit a larger spread of values, which may be potentially explained by the non-uniformity of particle deposition caused by substrate charging.

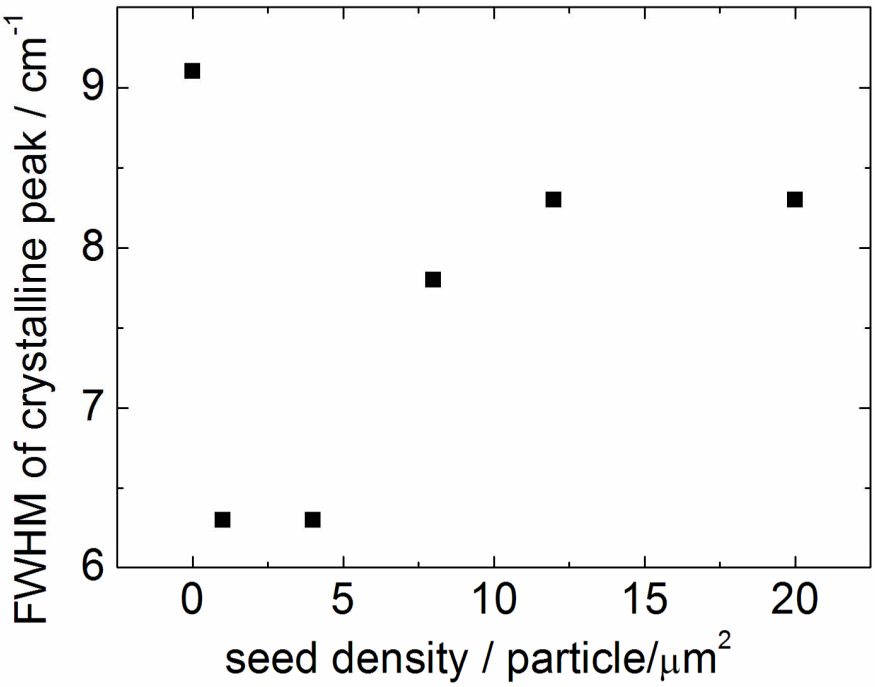

Figure 4.4: FWHM of a-Si TO peak of "fully" crystallized seeded films with varied nanoseed density, compared the unseeded film.

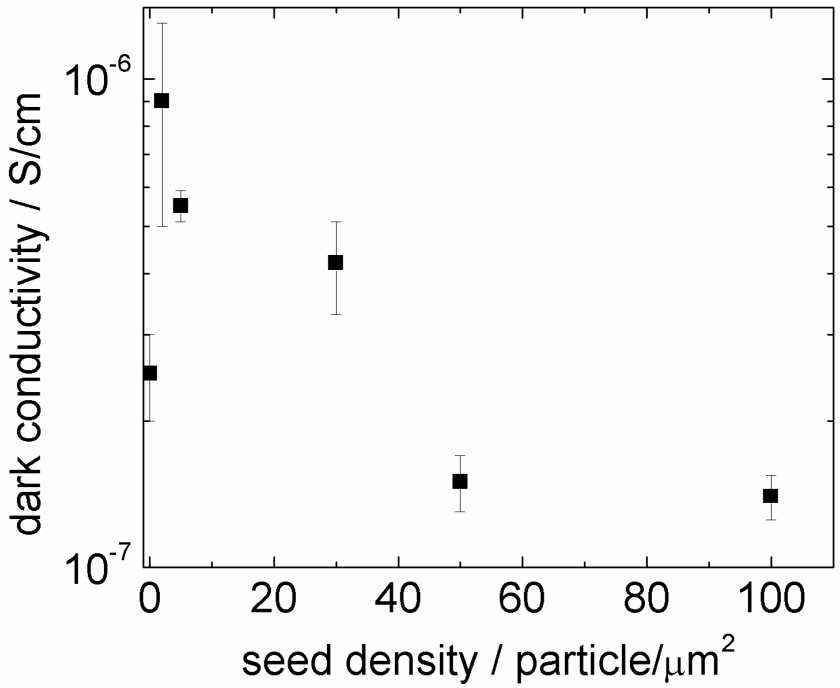

Figure 4.5: Plot of dark conductivity as function of initial seed density, compared with an unseeded control film. (Courtesy of Jason Trask).

4.3 Growth Model

In this study, the induced silicon nanocrystal seeds serve as pre-existing nucleation sites, and the growth originating from the seeds can be divided into two stages (Figure 4.6): the initial grain growth originating from the seeds before adjacent growth fronts meet with each other, and a second stage during which growth fronts collide and crystallization only proceeds in the remaining amorphous gaps between grains.

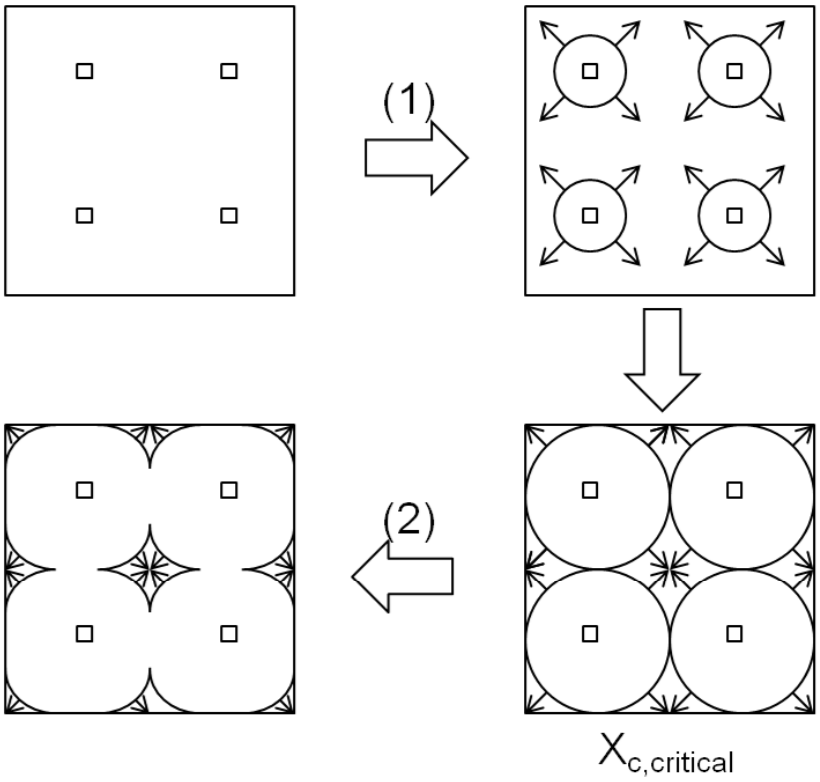

Figure 4.6: Schematic of the growth model of seeded film including two distinct stages. Arrows represent the direction of grain growth.

Considering a uniform distribution of nanoseed population density, the inter-particle distance is usually above hundreds of nanometers, larger than the thickness of the film. It is therefore appropriate to assume two-dimensional growth in the first growth stage:

$$\chi_c = \chi_{c0} + \pi\rho v_g^2 t^2 \tag{4.1}$$

χ_{c0} is the initial crystallinity estimated from the seed density acquired from TEM images, v_g is the isotropic grain growth rate and ρ is the effective aerial seed density, which takes into account the effect of seed stacking. After the Raman crystallinity, χ_c, reaches a transition value, $\chi_{c,critical}$, that divides the two distinct growth stages, the crystallization growth is calculated as:

$$\chi_c = \chi_{c,final} - \rho(4-\pi)(\sqrt{\frac{1}{\rho}} - v_g t)^2 \tag{4.2}$$

$\chi_{c,final}$ is the final crystallinity, typically close to 0.8. Figure 4.7 shows an example of the fitting technique of time-series Raman crystallinity curve by two-stage growth model and the grain growth rate, v_g, is shown to decrease as the seed density increases (Figure 4.8), consistent with the observation in Figure 4.2. The difference in v_g between two stages is due to the 2-D approximation at the first stage.

The Kolmogorov-Johnson-Mehl-Avrami (KJMA) equation is another strong tool to describe phase transformation kinetics. The key assumption in the derivation of the KJMA equation is that the nuclei are distributed randomly in 3-dimensional space. A typical KJMA model is characterized by the "S-curve", where growth is initially slow, then accelerates, followed by decelerating to saturation. Such growth behavior is described by the following exponential relation [57]:

$$f = 1 - e^{-Kt^n} \tag{4.3}$$

f is the crystallinity and k and n are Avrami constants. There is no clear physical interpretation of the Avrami constant k, which is a complex function of film property

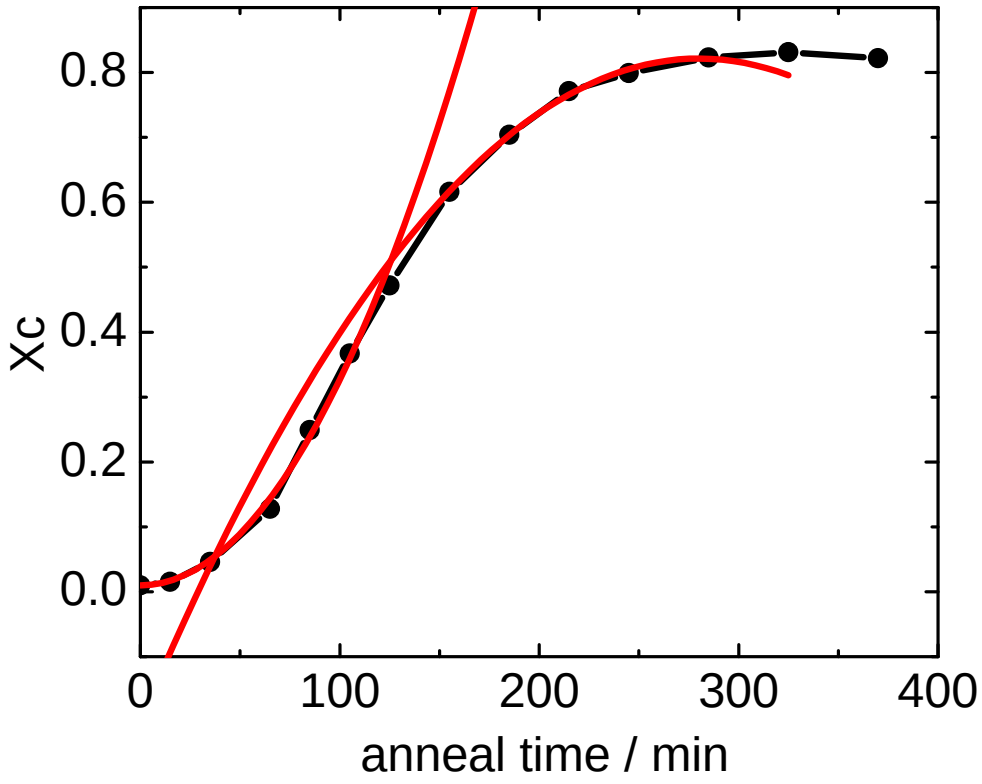

Figure 4.7: Example of fitting result of time-series Raman crystallinity curve by two-stage growth model. The seed density is 10 particle per μm^2.

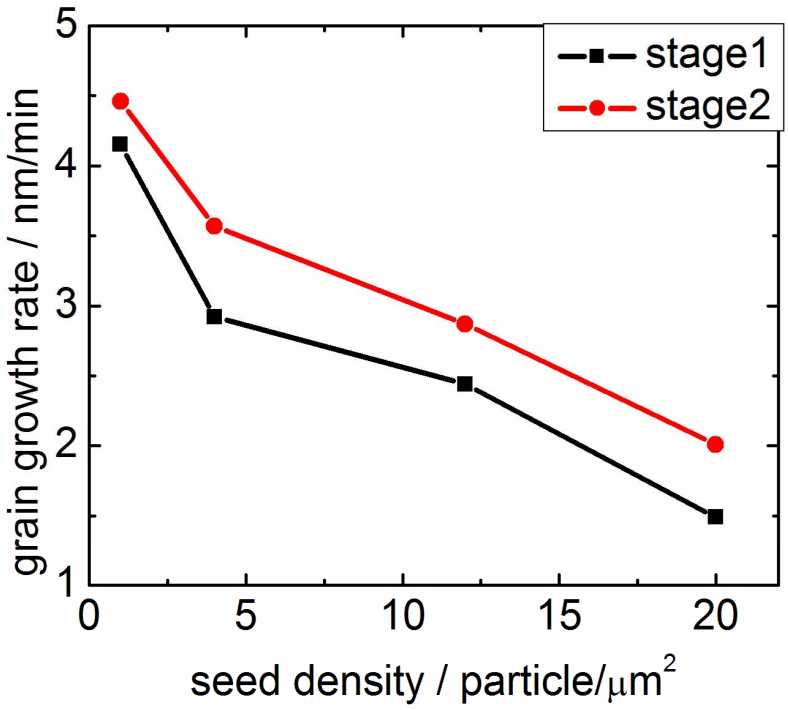

Figure 4.8: Grain growth velocity of the seeded films with different seed density.

as well as seed concentration. The constant n reflects the nature of the crystallization transformation. For instance, an n value of 4 describes a 3-dimensional growth plus one additional dimension from a constant nucleation rate. If the nuclei pre-exist at the beginning, the transformation is dominated by the 3-dimensional growth of the nuclei and n has a value of 3 [58].

Figure 4.9 compares the Avrami coefficient n between unseeded and seeded a-Si:H films with varied seed density. The unseeded film has an n value always larger than 4, indicating a 3-dimensional growth geometry plus a time constant nucleation rate, representing the growth kinetics of intrinsic a-Si film. On the other hand, all the seeded films have n values smaller than 3, since the nanoseeds are distributed randomly only in 2-dimensions at the interplane between amorphous layers, departing from the 3-dimensional approximation of the KJMA model. There is a clear trend that increasing seed density reduces the spacing between seeds, thus leading to smaller values of $\chi_{c,critical}$. This causes more offset from free 3-dimensional hemispherical seed growths and thus a smaller n value.

4.4 Role of Hydrogen

Hydrogen is believed to be a key factor in the crystallization process as well as the stress in a-Si:H films. The incorporation of hydrogen passivates dangling bonds, lowering the concentration of both the midgap states and band tail states [59]. Specifically, previous work has shown clear evidence for a structural transition from the relatively highly stressed or more disordered networks to the more ordered network when the total hydrogen content exceeds 15 % [15, 60]. The hydrogen evolution from nanocrystalline silicon films during annealing has been studied experimentally and computationally as

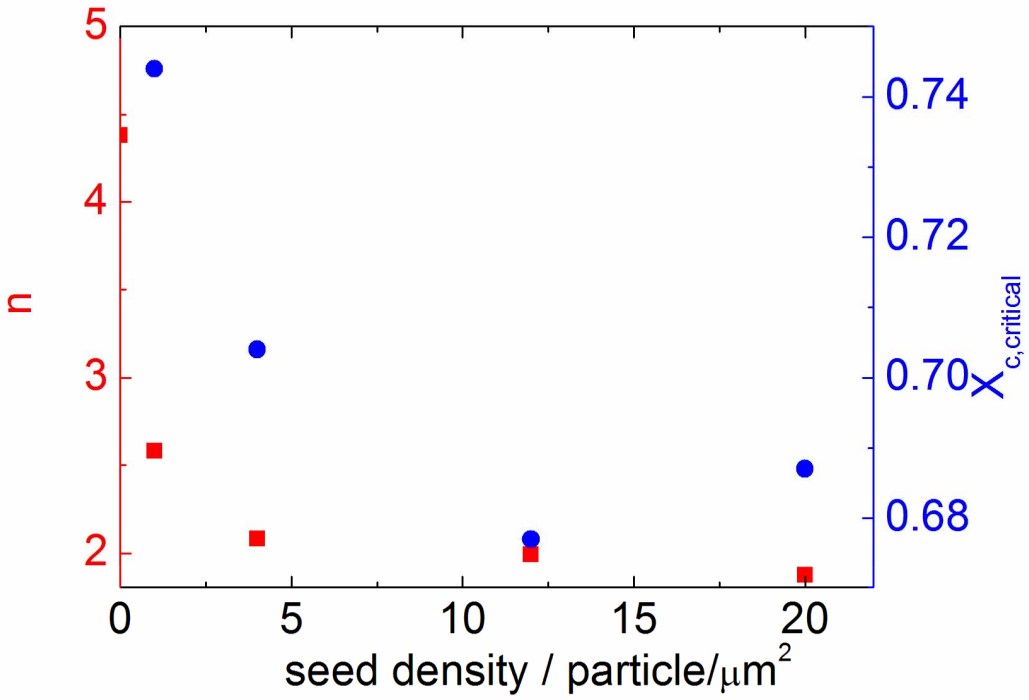

Figure 4.9: Avrami coefficient n at the first stage of two stage growth model and the transition crystallinity $\chi_{c,critical}$, as a function of seed density.

a function of annealing temperature [61, 62]. It is suggested that hydrogen is preferentially released from the grain boundaries (typically in the form of dihydrides) around 400 °C and from the bulk film (typically monohydrides) between 600-650 °C, with the rate of evolution increasing dramatically at even higher temperatures [63]. Since crystallization only occurs at temperatures above 550 °C, it is proper to assume that the relatively small amount of hydrogen at the nanocrystal seed surfaces evolves at the very early stages of annealing and only the hydrogen within the bulk film plays an important role in crystallization. The duration of the amorphous incubation period is associated with the time required to effuse the initial hydrogen content from the film, thus less hydrogen would induce faster onset of crystal growth. On the other hand, higher hydrogen concentration leads to a higher density of crystalline nuclei, which prevent grains to grow to a considerable size [64]. In this study, however, there is no artificial nucleus in the film.

In the case of PECVD films, the deposition conditions have direct effects on the hydrogen incorporation and the amorphous film microstructure. One significant way to control the hydrogen concentration of the film is to adjust the deposition temperature. The hydrogen content is measured by Forward Recoil Spectrometry (FReS) in Figure 4.10, where a clear trend shows that by increasing the deposition temperature during a-Si:H film growth, the bulk hydrogen content decreases accordingly. The decrease in hydrogen content is associated with an increase of the hydrogen diffusion coefficient [65], which is explained by the change of hydrogen solubility and hydrogen binding energy in silicon at different temperatures [66].

To study the effect of hydrogen content on the macroscopic crystallization kinetics, seeded films with varied temperature are deposited on glass substrates and measured by Raman spectroscopy upon furnace annealing. Figure 4.11 shows that films with higher

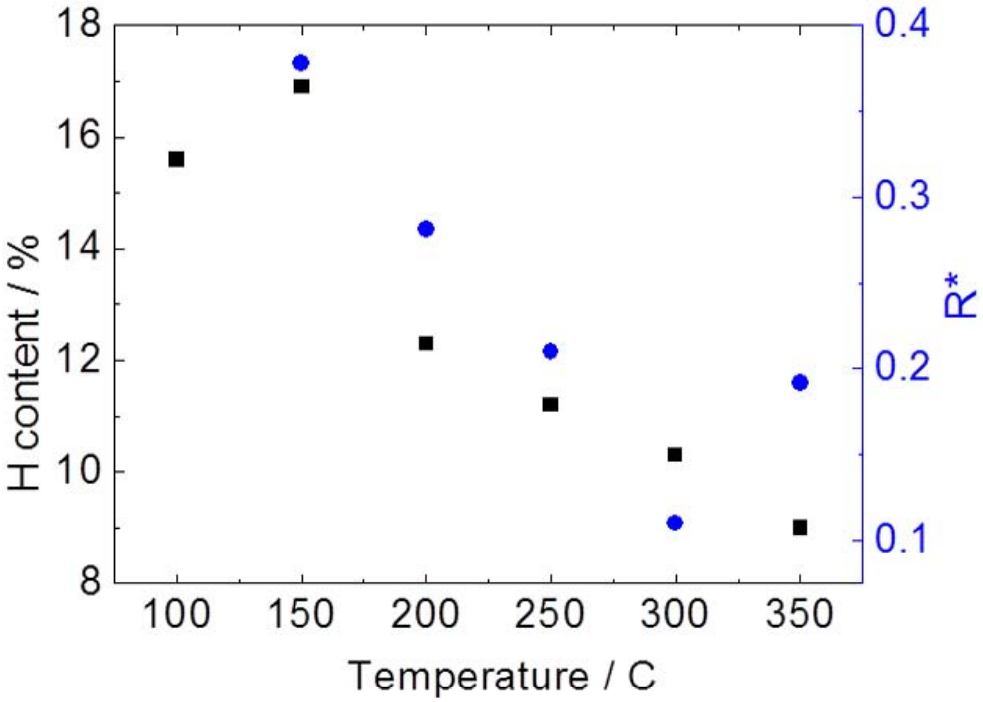

Figure 4.10: Plot of hydrogen concentration as well as the microstructure parameter in seeded films with different deposition temperature.

deposition temperature or lower hydrogen content exhibit substantial enhancement of crystallization. Such phenomenon is related to the observation that the increase of H content in the amorphous matrix enlarges the medium range disorder (MRD) of a-Si:H film, which is supported by the increasing microstructure parameter in Figure 4.10. The microstructure parameter R* is defined as:

$$R^* = \frac{I_{2100}}{I_{2100} + I_{2000}} \tag{4.4}$$

R* quantifies roughly the fraction of clustered hydrogen in the film and the microstructure quality of the film. I_{2000} and I_{2100} are the integrated infrared absorption peaks at 2000 cm^{-1} and 2100 cm^{-1}. The 2000 cm^{-1} peak is generally assigned as the stretching oscillations of isolated Si-H bonds, while the 2100 cm^{-1} peak originates from Si-H_2 and Si-H_3 located on nanosized void surfaces. The microstructure parameters in all the films are over 0.2 which indicate highly disordered films. Upon annealing, those nanosized voids collapse upon hydrogen effusion and restructure to form a more compact and ordered film, leading to higher crystallization rate [16].

4.5 Stress measurement

It is believed that the crystallization of a-Si:H films is strongly dependent on the residual stress in the film. The thermal energy provided by annealing is used to relieve the initial stress in the film and to initiate the crystallization process. Although the actual nature of intrinsic film stress is not fully understood in a-Si:H, it is hypothesized that it is related to the total hydrogen content within the film [67]. Furthermore, it has been shown that tensile stress applied to silicon films during annealing enhances the crystallization, while compressive stress produces an opposite effect [68, 69]. Previous studies measure the

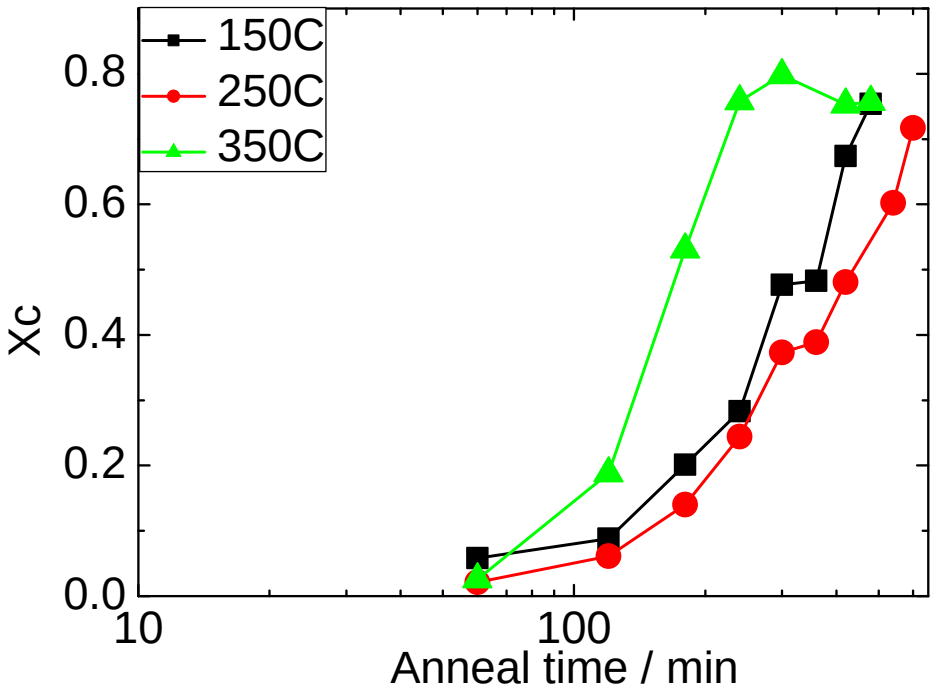

Figure 4.11: Plot of Raman crystallinity as a function of anneal time at 650 °C, for seeded films with different deposition temperature.

stress variation of intrinsic amorphous Si film upon annealing and observe a transition from highly compressive to highly tensile stress at roughly 400 MPa, including an initial rapid increase, a period of latency, a quasi-linear increase and a final level. The initial rapid increase has been explained due to dehydrogenation effects at the initial stage of annealing. The next two steps correspond to the incubation period and the volume contraction during crystallization phases, respectively [70].

The local residual stress σ can be measured throughout the crystallization process using Raman spectrometry with the following relationship [71]:

$$\sigma(MPa) = -250(\omega_s - \omega_0)(cm^{-1}) \tag{4.5}$$

ω_0 is the wave number of the stress free single crystal (520.5 cm^{-1}) and ω_s is the wave number of crystalline TO peak signal measured within the sample. A peak shift toward wave numbers lower than 520.5 cm^{-1} indicates tensile stress, and a shift towards higher wave numbers is related to compressive stress. Using this technique, the evolution of intrinsic stress with crystal growth is tracked for films of varying seed densities, shown in Figure 4.12. The seed density is varied between 1 and 20 particle per μm^2 and annealing temperature is kept at 650 °C. A large tensile stress in the films at begin stage of annealing is observed, opposite to what is reported in literature, due to the significant increase of the interfacial structure with the inclusion of nanocrystals. The initial increase of tensile stress during annealing corresponds to the volume contraction during crystallization [72]. The stress arrives at a maximum value at anneal times of 220-240 min for all the samples, approximately the same time when the Raman crystal fraction starts to saturate. This suggests a clear link between the crystallization process and the stress state within the film. The following decrease in stress at the end of the crystallization process is possibly caused by the movement of intra-grain defects in the

crystal grains such as dislocation glide, dislocation creep or diffusional creep [73]. Overall the introduction of nanoseeds increases the tensile stress in the amorphous film, which further enhances the crystallization process.

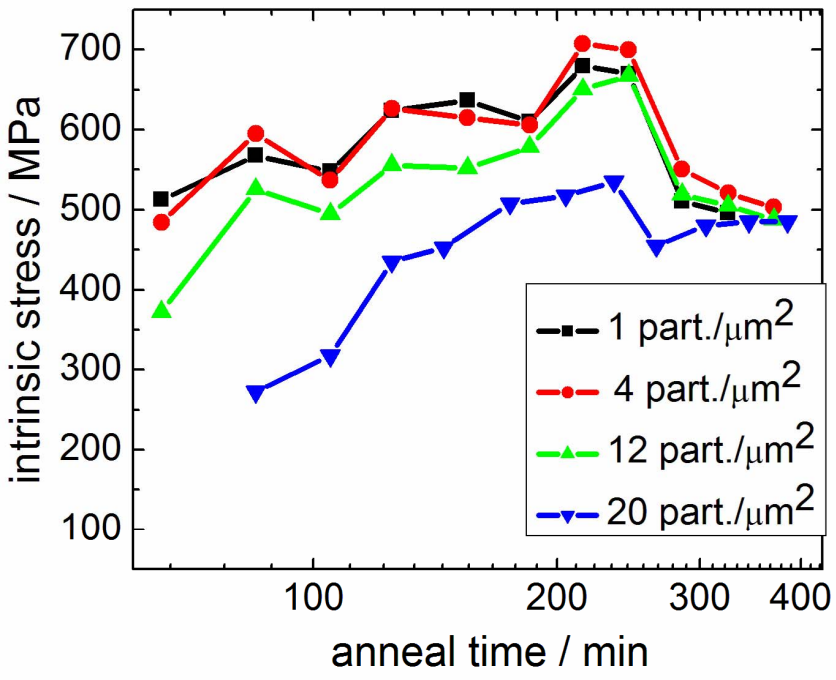

Figure 4.12: Time-series of intrinsic tensile stress of seeded films annealed at 625 °C.

Chapter 5

Nanovoids

5.1 Overview

This chapter discusses the microscopic crystallization kinetics of the layered structure film and the new phenomena, nanovoids, observed under in-situ TEM annealing. Nanocavity regions, referred to as "nanovoids", form at the interface between nanoseeds and the amorphous matrix. Those nanovoids propagate through the film during annealing at a speed higher than the SPE of the seeds and leave crystalline region behind. This further enhances the crystallization of a-Si:H films. Further study explains the formation of nanovoids related to film nanoporosity and the shading effect of the nanoparticles. The void propagation mechanism is believed to be the combination effects of atomic surface diffusion at its inner surface and twin growth at its tail region.

5.2 Nanovoid Formation

The motivation of this chapter is to explore microscopic crystallization events of the films with layered structure in HSTEM. The film structure is the same as that in Chapter 4:

cubic Si nanocrystals with density of around 4 particle per μm^2 are embedded between a 20 nm sublayer and an 80 nm capping layer. The films are deposited on thin carbon film (less than 10 nm) coated molybdenum (Mo) grids. Samples are loaded in the double-tilt heating-stage holder and then annealed in TEM with for real-time monitoring of the crystal growth. Phase diagrams confirm that the annealing temperature used in this study is below the melting temperature of Mo-Si alloys.

Figure 5.1 shows the time-series images recorded under 625 °C annealing, revealing a new kind of nanovoid enhanced crystallization mechanism never previously reported in literature.

The first image (a) is recorded after ramping the temperature of the TEM holder to 625 °C. It takes about 5 min for the sample to stabilize after the holder reaches desired temperature, as the Mo grid expands slowly during temperature increasing. While there is no significant sign that the embedded seed crystals start to grow, some clearly-defined light-contrast structures, indicating low density materials, form at the interface between the particles and the amorphous film. It is notable that almost every particle has such light-contrast regions present, and that these regions have irregular shapes and keep restructuring as they remain located at seed boundaries. Dark-field STEM images suggest that these light-contrast structures have missing silicon atoms, and represent voided regions [43].

Figure 5.1 (b) is recorded 10 min after Figure 5.1 (a), and shows that light-contrast structures start to coalesce into bubble-like structures, hereby referred to as "nanovoids". The size of the nanovoids varies from less than 5 nm to greater than 20 nm. The nanovoids appear to form repeatedly at the temperature as low as 570-580 °C, below the crystallization temperature of Si. Previous studies have observed similar phenomena of void formation. Tane et al. found that nanovoids of 1-2 nm formed during annealing

of amorphous Al_2O_3 films at 700 °C for 1-12 h, but no crystallization of the Al_2O_3 films was observed and films remained in an amorphous state [74]. They claimed that the nanovoid formation is caused by inhomogeneity in density due to volume shrinkage during annealing. Godet et al. reported the formation of nanovoids in a-Si:H related to the diffusion of hydrogen [75]. However, none of these studies reported the propagation behavior of nanovoids.

In Figure 5.1 (c), imaged after 30 min, nanovoids start to move away from their original location towards the bulk film. After 120 min, the nanovoids have moved several tens of nm from their original location and the tail region, in the wake of the voids, leave crystallized material behind, as shown by the measurement of diffraction pattern. The speed of the voids through the film is noticeably faster than the normal grain growth speed of embedded nanocrystals. Also, the voids continuously change their direction during motion. The size of a nanovoid is interpreted as the diameter of its back tail. The void in the left-middle of Figure 5.1 (e) with largest size seems to propagate the most distance. Simultaneously, voids smaller than 5 nm do not show significant displacement. It is frequently observed that the path of two nanovoids intersect without the voids merging with each other, evidence of 3-dimentional void motion.

In the final image (Figure 5.1 (f)), several voids appear to have ceased movement and become trapped as their front parts meet other crystalline materials. It is necessary to point out that the void motion is 3-dimentional, while the TEM images are only able to record the top-view 2-dimentional projection of void propagation. Therefore, the voids may still move outwards or inwards across the film, even when they appear to be stationary in TEM. Additionally, volume of the nanovoids does not change during the annealing process, and native nucleation is not observed as the film fully crystallizes within 3 hr of nanovoid formation.

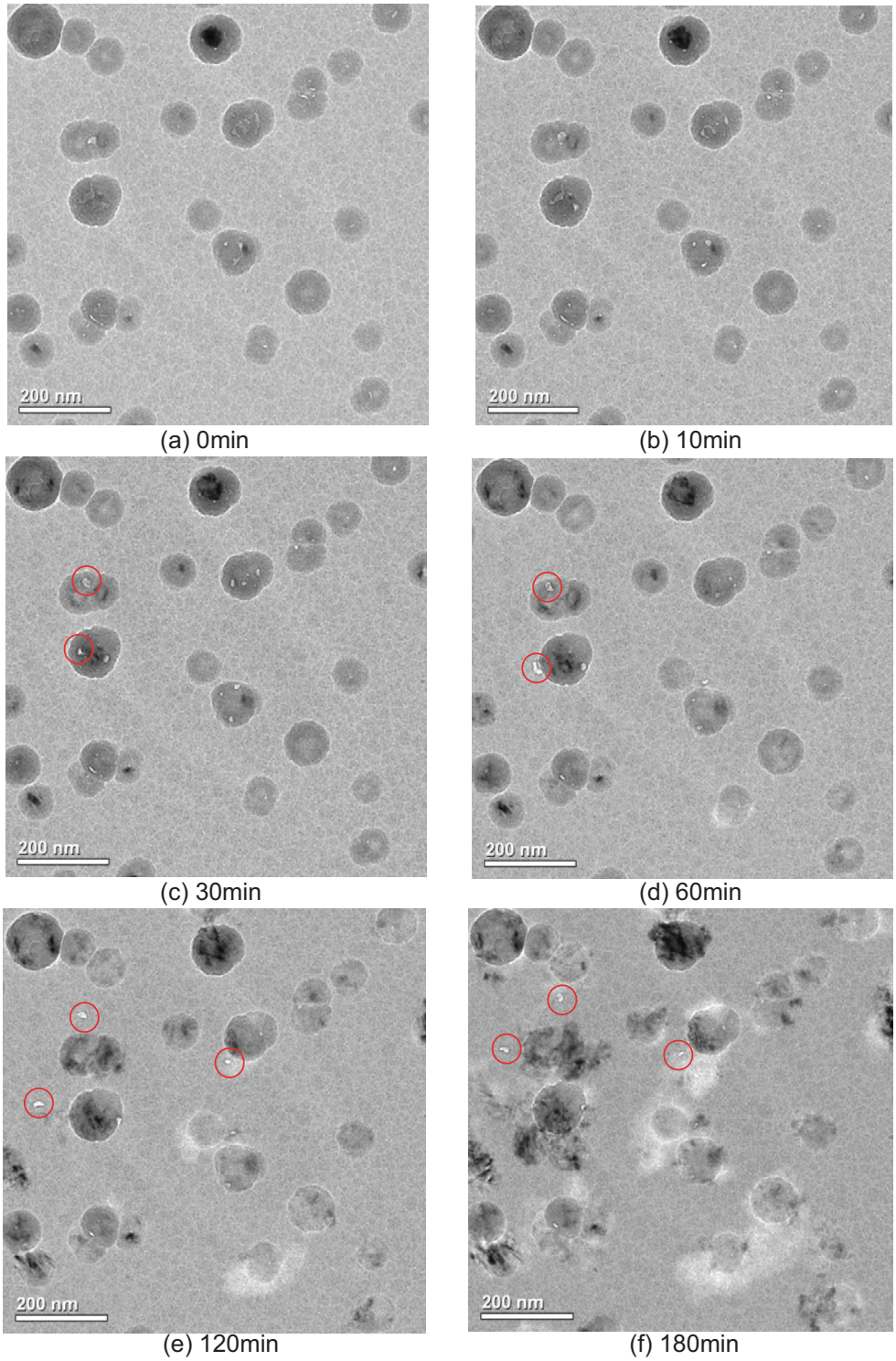

Figure 5.1: Time series images of HSTEM annealing of seeded film at 625 °C, indicating formation and propagation of nanovoids. Some propagating voids are circled in red.

Cross sectional TEM, performed by Andrew Wagner, is used to explore the formation mechanism of nanovoids. Figure 5.2 (a) shows the cross-sectional images of as-deposited seeded films without annealing. A cone-shaped region can be clearly observed around the nanoseed, a result of the inclusion of the nanoparticle within amorphous matrix. The light-contrasted region exists at the boundary of seeds and amorphous regions, extending from below the nanocrystal upward to the film surface. Figure 5.2 (b) shows that the light-contrasted region start to coalesce into a nanovoid upon annealing at 650 °C of 20 min.

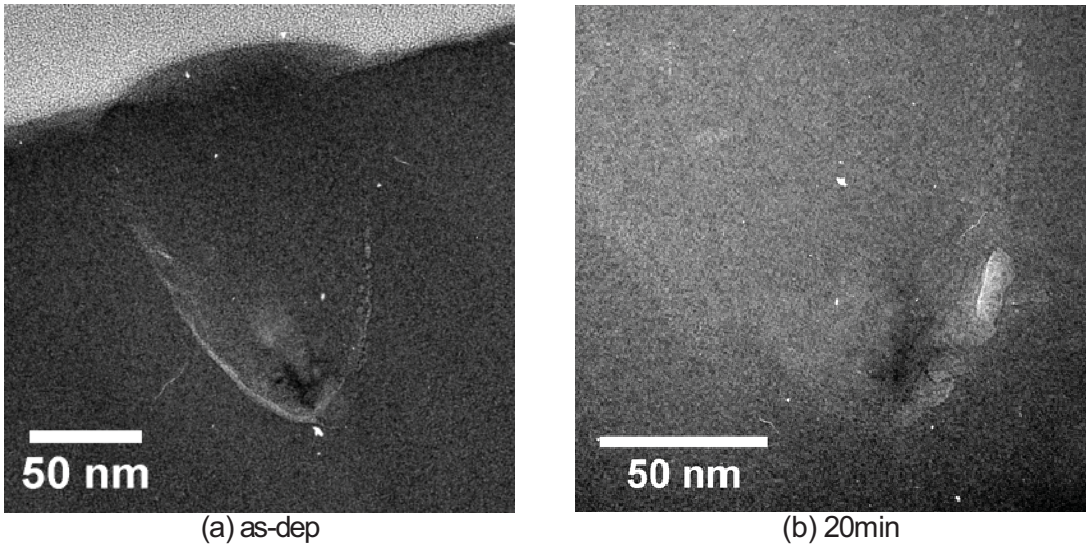

Figure 5.2: (a) Cross sectional TEM image of as-deposited a-Si:H film seeded with cubic Si crystals. The cone-shaped structure indicates the existence of nanovoids before annealing. (b) Cross sectional TEM image of seeded a-Si:H film annealed at 650 °C of 20 min. (Courtesy of Andrew Wagner)

Monte-Carlo simulations, performed by Andrew Wagner, of growth of seeded a-Si:H films reveal that the open volume region observed in cross-sectional TEM originates from nanoporosity arising from the atomic self-shadowing effect during film deposition as well as the shadowing effect due to the existence of nanoseeds, as shown in Figure 5.3. This shadowing effect is common in thin film deposition as well as micro-electronic processes, and leads to the formation of rough surfaces. For example, nanoseeds serve as a barrier to growth species, making it difficult to reach the corner of the seeds, as the growth species can approach the film surface at oblique angles but become more easily captured by higher surface points (top portion of nanoseed sidewalls). Shadowing can also occur at an atomic scale without nanoseeds and cause growth of nanocavity/nanoporosity during ballistic deposition of normal angle growth. Furthermore, the interface between the nanoseeds and sub-layer a-Si:H is not perfectly flat due to the surface roughness of an a-Si:H film. The open volumes beneath the seeds also contribute to the formation of nanovoids. To summarize, both the film nanoporosity and the incorporation of nanoseeds contribute to the light-contrast region at the boundary of the conical structure.

At elevated temperatures of 580-600 °C, the light-contrast region coalesces into large bubble-shaped nanovoids. Such deformation is driven by the minimization of the local free energy in terms of minimizing the surface area of the nanovoids [76, 77]. Spherical voids would form in the purely amorphous film, while in the case of silicon nanocrystal seeded films, the tendency to minimize surface free energy results in bubble-shaped nanovoids, with co-existence of both amorphous phase and faceted crystalline surfaces with minimum surface energy.

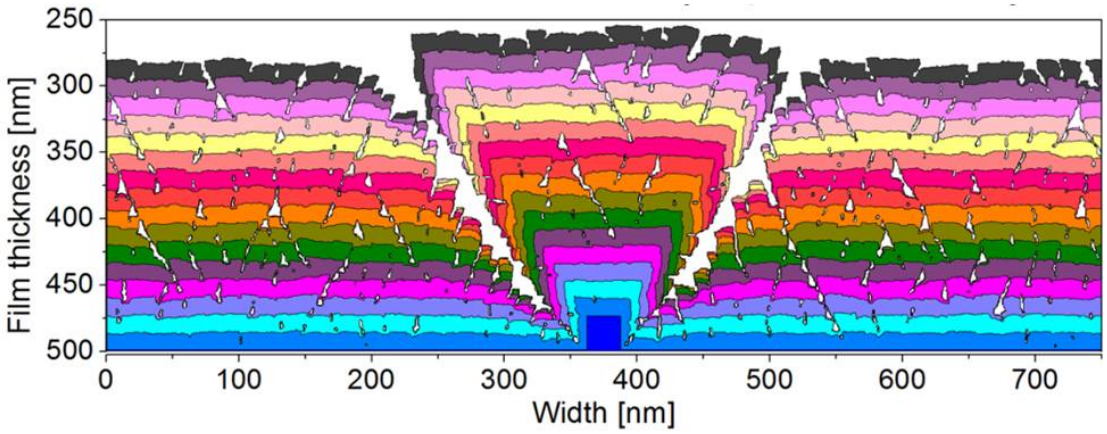

Figure 5.3: Monte-Carlo simulation of growth of seeded a-Si film shows the voided region as the results of film nanoporosity and nanoseeds incorporation. (Courtesy of Andrew Wagner)

5.3 Void Motion

5.3.1 Surface Diffusion

High-resolution TEM reveals the detailed structure of the nanovoids after partial annealing. In Figure 5.4, the red arrow indicates the direction of the void motion away from the seed crystal. It is clear that the front region of the void is amorphous, while the tail region behind the void is crystalline, as evidenced by the (111) lattice plane spacing. The shape of the void suggests that void movement is driven by surface diffusion of silicon atoms along the inner surface of the void from the amorphous to the crystalline side of the void. Surface diffusion causes the amorphous side to deplete while the crystalline surface grows. This contributes to the fast propagation of voids which outpace the normal solid phase epitaxy (SPE) originating from the embedded seeds. At steady state, the depletion rate of atoms at the amorphous side of the void must balance the growth rate at the crystalline side of the voids, which implies that the propagation speed at the amorphous side must be the same as that at the crystalline side along the propagation direction. The volume of the void region must be conserved during propagation, considering only surface diffusion kinetics, as the bulk self-diffusion of Si happens with a much higher activation energy (E_a = 4.6-4.8 eV) than surface diffusion (E_a = 2.38 eV) [78, 79].

Another set of HSTEM experiments is designed to confirm that the presence of initial crystalline phase is necessary to lead to void propagation, in which a-Si:H films are embedded with amorphous silicon nanoparticles. The time-series TEM images are shown in Figure 5.5. The first image (a) is recorded when the temperature stabilized after being ramped up to 625 °C. The embedded amorphous nanoparticles are not visible in the TEM image because both the seeds and the background film are amorphous in

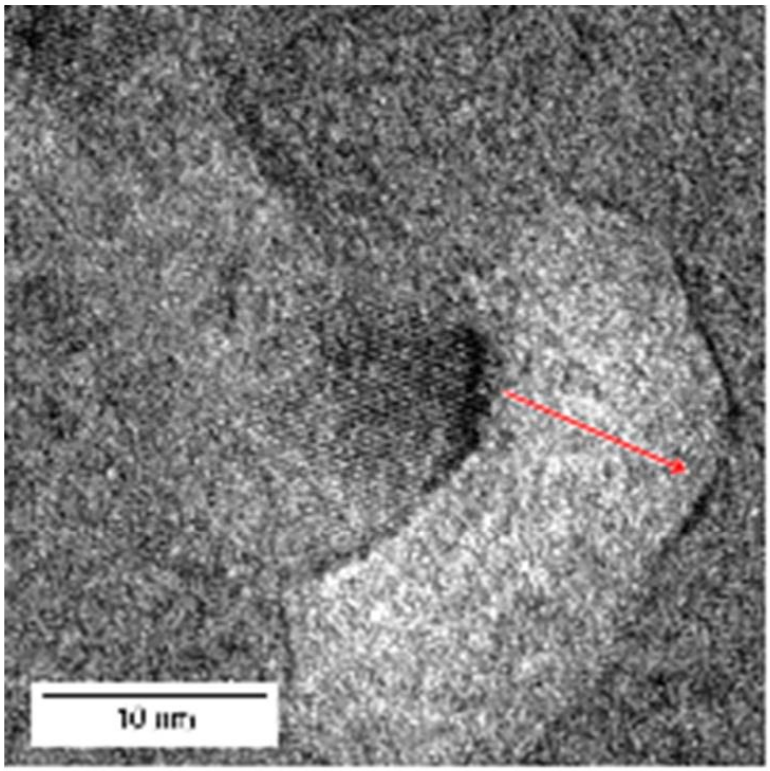

Figure 5.4: High resolution TEM image of nanovoid structure. Red arrow indicates the direction of void propagation. (Courtesy of Ozan Ugurlu)

structure. Voids form at the boundary of the seeds terminated with all amorphous phase, as verified by the SAD image. However, all the nanovoids appear stationary for a minimum of approximately 120 min, during which time the seeds are still amorphous (Figure 5.5 (b)). Figure 5.5 (c) shows that after 120 min, when the amorphous seeds start to crystallize and the tail region of the voids become crystalline, the voids begin forming bubble-like shapes and start propagating throughout the film. By comparison in crystalline particle seeded films, the time for the voids to start to move is less than 15 min at the same annealing temperature. As time progresses beyond the initial void formation stage, the voids move further from their original locations into the amorphous film, and leave crystalline regions in their wake, similar to the case of crystalline seeds. Considering that the time at which significant crystal growth can be seen in the film is well beyond the native incubation time observed in unseeded films at this temperature, native nucleation is most likely contributing significantly to grain growth as well. This HSTEM experiment confirms the mechanism of diffusion of silicon atoms along the partially amorphous/partially crystalline internal surface, and that the voids with fully amorphous surface do not propagate through the film until the nanovoid tail region crystallizes.

A 2D continuous surface diffusion equation is developed to further explain the kinetics of void propagation driven by surface diffusion. The system of a nanovoid at steady state is modeled with a polar system in Figure 5.6, assuming a void with hemi-spherical symmetry. The entire void region is at positive y axis and the x axis serves as the boundary of the crystalline tail of the void.

Assuming that the surface diffusion is only governed by the local curvature and annealing temperature, the increase of the chemical potential μ of Si atom when travelling from the center point of the front side (where the local curvature is zero) to a point

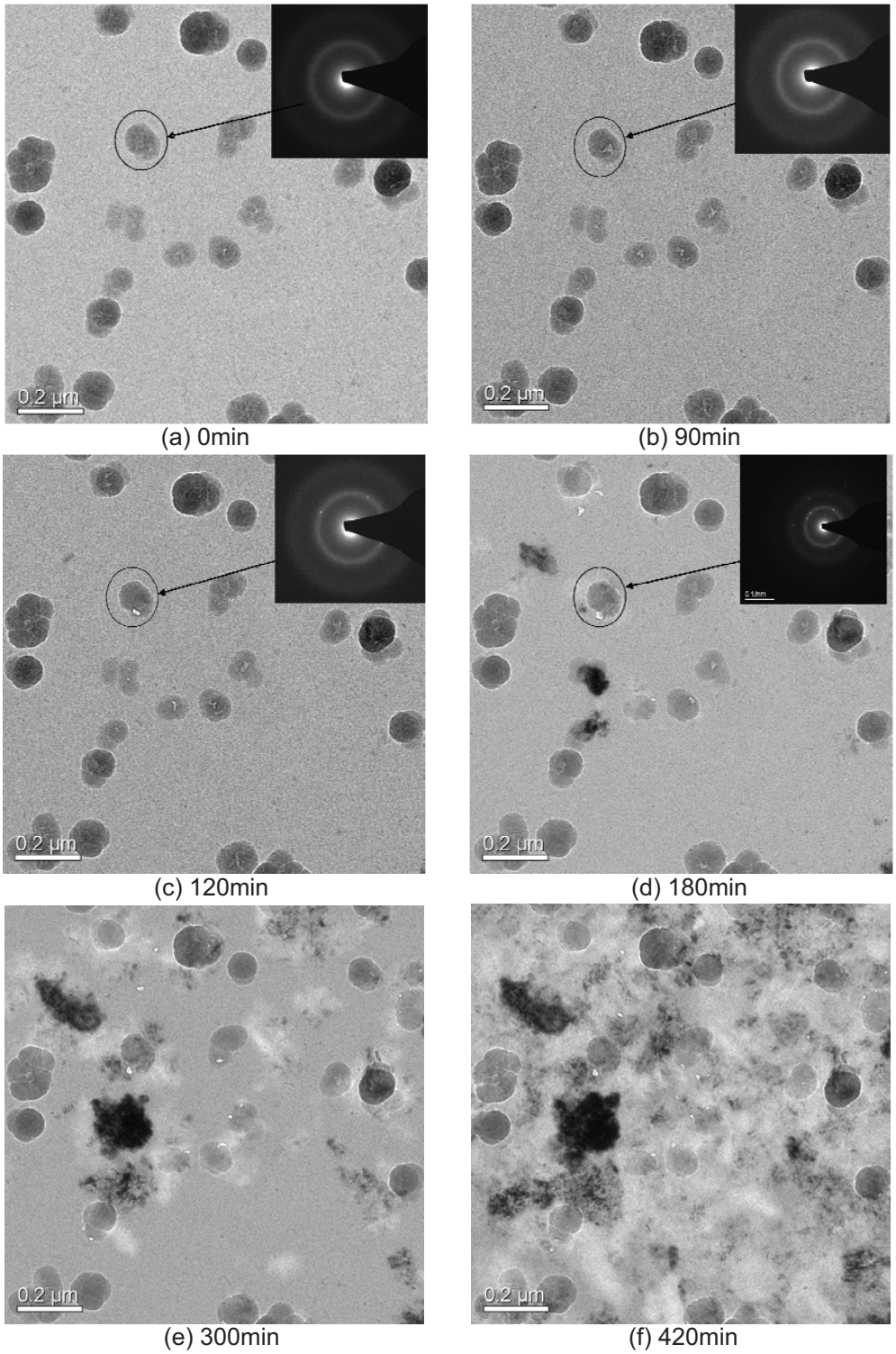

Figure 5.5: Time series images of HSTEM annealing of amorphous particle seeded film at 625 °C, indicating formation and propagation of nanovoids.

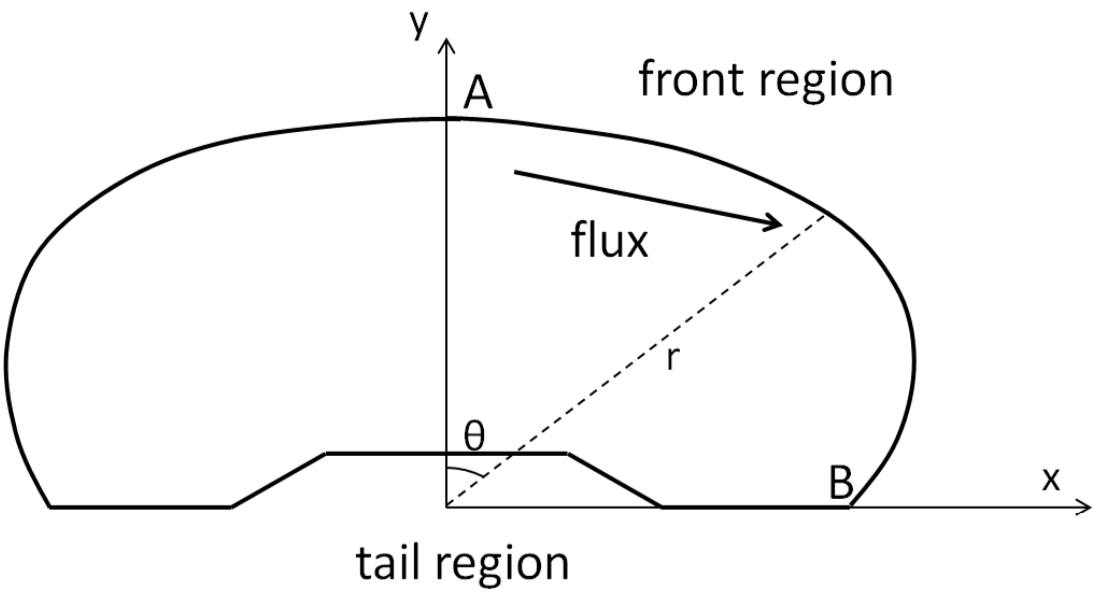

Figure 5.6: Sketch of nanovoid at steady state. The arrow shows the direction of atomic flux.

with curvature C is calculated as [80]:

$$\mu = \gamma \Omega C, \tag{5.1}$$

where γ is the surface free energy of the amorphous Si (1.9×10^{-4} J/cm^2) and Ω is the averaged atomic volume of amorphous Si and has a value of 1.07×10^{-22} cm^3. A gradient of chemical potential along the inner surface of the void creates a flux J_s of surface atoms, described by the Nerst-Einstein relationship [81]:

$$J_s = -\frac{D_s N_s}{kT}\frac{\partial \mu}{\partial s}, \tag{5.2}$$

where s is the arc length along the void surface and D_s and N_s are the surface diffusion coefficient and surface atomic density (4.4×10^{14} atom/cm^2 for amorphous silicon), respectively. The diffusion coefficient D_s has an Arrhenius form:

$$D_s = D_0 e^{-\frac{E_A}{kT}}. \tag{5.3}$$

For amorphous silicon, the coefficients D_0 and activation energy E_A are 4×10^1 cm^2/s and 2.38 eV, respectively [82]. Combining Equations 5.1 and 5.2, the atomic flux at nanovoid surface is:

$$J_s = -\frac{D_s N_s \gamma \Omega}{kT}\frac{\partial^2 C}{\partial s^2} \tag{5.4}$$

If there is no mass transfer in the ϕ direction and all the Si atoms are captured by the growth fronts at the crystalline tail to allow solid-phase epitaxy (SPE) to occur, the mass balance equation shows the growth speed along the y direction at any front surface point of the void:

$$V_{void} cos\theta_s = \frac{\partial y}{\partial t} = -\Omega \frac{\partial J_s}{\partial s} = \frac{D_s N_s \gamma \Omega^2}{kT} \frac{\partial^2 C}{\partial s^2} \tag{5.5}$$

Equation 5.5 shows that the void propagation speed is proportional to the second order derivative of surface curvature to arc length. However, due to the relatively low resolution of TEM image, it is difficult to measure the surface curvature at the void surface. Assuming that all voids have the same shape irrespective of size and zero local curvature at the center point of the front side, Equation 5.5 suggests that smaller sized voids should have a higher propagation speed than larger ones, which is opposite of what observed in HSTEM experiment. Therefore, there must be another mechanism that also contributes to the nanovoid propagation.

5.3.2 Crystal Twinning

Crystal twinning is frequently observed in most crystalline materials, including silicon [83]. It occurs when two crystal grains share the same crystal lattice planes symmetrically at their boundaries. In silicon, the energy to form twin boundaries is significantly lower than that of the other grain boundaries. Twin boundaries in silicon have very low electrical conductivity and their energy level is outside the silicon band gap. The mechanism of twin boundary formation during crystal growth is still unclear, but it is believed that a twin boundary forms parallel to other twins along the {111} facet face during crystal growth and surpercooling of the silicon melt is the driving force of twin formation [84].

Figure 5.7 shows the twinning kinetics on the Si {111} plane. Without the presence of crystal twinning, the silicon {111} surface has the lowest density of dangling bonds and the lowest surface energy. Therefore, the {111} plane is the slow growth plane of Si. This plane requires three adatoms per surface atom to grow a new layer. Nevertheless,

if a twin boundary forms at the surface, the mirror symmetry of adjoining grains leads to a surface angle of 141.06 degrees, allowing only two adatoms to grow a new bond at the twin surface. Therefore, the growth at the twin boundary needs energy less than one-fifth of that at other grain boundaries [85].

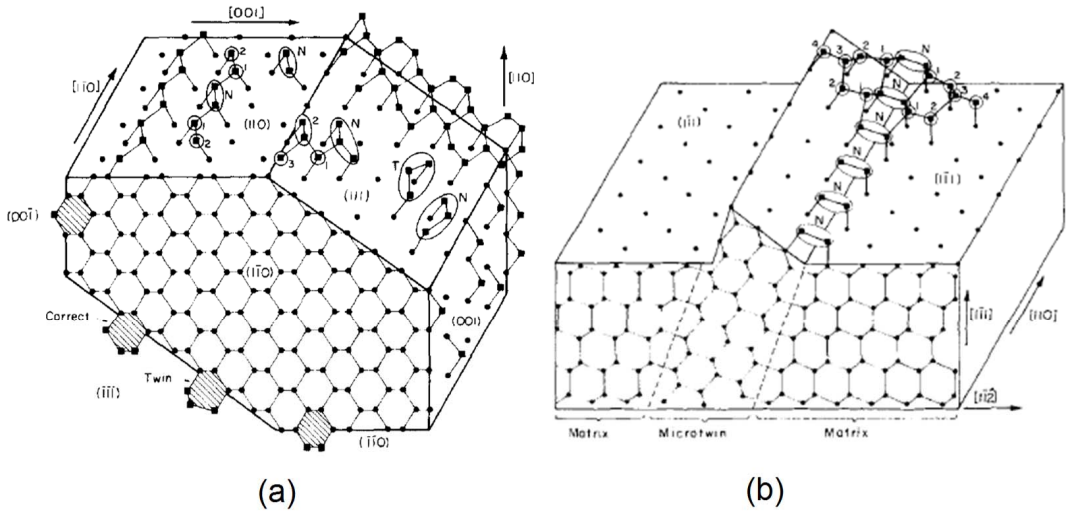

Figure 5.7: Schematic of crystal twinning along Si {111} plane: (a) It needs three adatoms to grow a new layer without twinning, (b) Only two adatoms are sufficient if a twin is present. [86]

High resolution TEM consistently shows the existance of twin formation at the {111} plane of tail region of the nanovoids (Figure 5.8). The measured angle of crystal planes at void tails indicates a value around 140 degrees which suggests the presence of twin boundaries at {111} planes, sketched in Figure 5.9. As shown in the surface diffusion modeling, the front amorphous part of the void provides sufficient adatoms for

the twin growth at the tail of the void. Once a nucleation site for twin growth forms at the back surface, the twin continues to grow on {111} surface along the direction shown by the red arrow until termination. Such growth fills the tail surface rapidly with another complete {111} surface. In the meantime there are always new nucleation sites for twin growth at the tail. Large area of nanovoid tail provides higher probability for a new twin growth site to form. Such formation and growth of the twin boundaries contribute to the step-like shape of void tails which is always observed in high resolution TEM study (Figure 5.4).

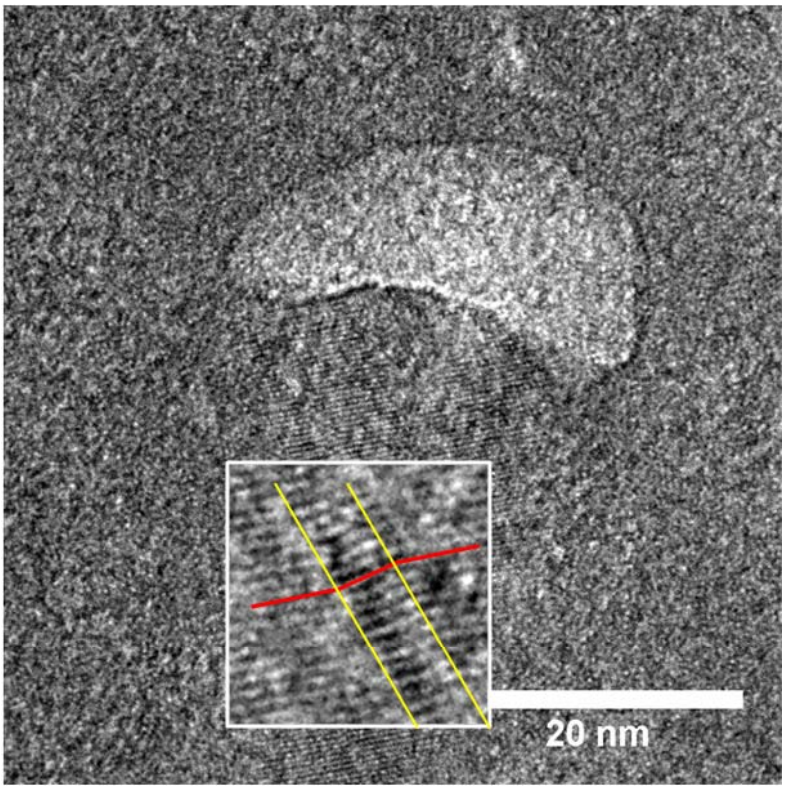

Figure 5.8: High resolution TEM image showing the existance of twin boundaries at the tail region of the nanovoid. (Courtesy of Andrew Wagner)

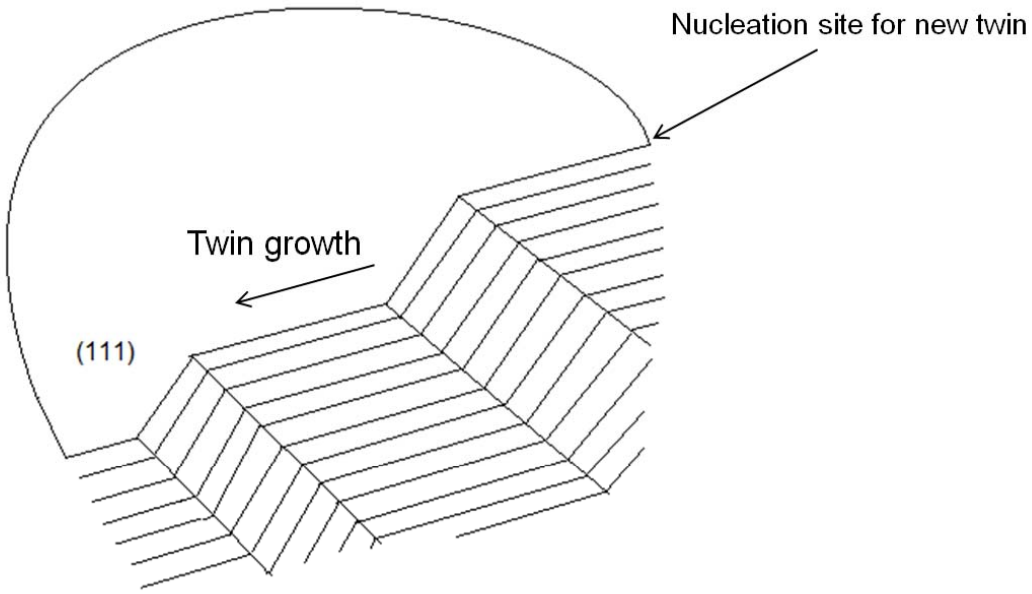

Figure 5.9: Sketch of void structure showing the growth of twin boundaries. The arrow shows the direction of surface atomic diffusion.

The study of void propagation speeds further confirms the twinning kinetics. Considering that void motion is due to the combinition of effects of surface diffusion at its front surface (approximately inversely proportional to the void size) and twin growth at its tail surface (proportional to the square of the void size), the overall void speed is expected to be roughly linearly proportional to its width. Figures 5.10, 5.11, 5.12 show the statistics of void speed versus void size at different annealing temperature of 600-625 °C, measured from time-series of HSTEM experiments using the ImageJ software. Each group of different colored data points represents one set of voids in the same HSTEM experiment. The error bars in these figures are relatively high since the measurement only studies the 2D displacement of void motion comparing to the 3D motion in the real case. Overall it is clear that the speed of void motion increases as void size increases even though there are large amounts of variation between data of individual HSTEM experiments.

The activation energy of nanovoid propagation can be extracted from the above measurement of void speed at various temperatures, assuming the void speed has a Arrhenius form of:

$$V_{void} = V_0 e^{-\frac{E_{a,void}}{kT}}, \tag{5.6}$$

where k is the Boltzman constant (1.38×10^{-23} $m^2kgs^{-2}K^{-1}$). E_a is defined as the minimum energy input to the system in order for a crystallization event to occur, therefore higher E_a means higher energy barrier. Figures 5.10, 5.11, 5.12 are fit with linear curves to extract void speed at different sizes. Figure 5.13 shows the Arrhenius plots of the speed of nanovoids with sizes of 10-20 nm at 600-625 °C, from the slope of which the $E_{a,void}$ is calculated as 4.8 eV. Such an energy value is interpreted as the sum of two distinct consecutive crystallization processes: for a nanovoid to grow a single atomic layer,

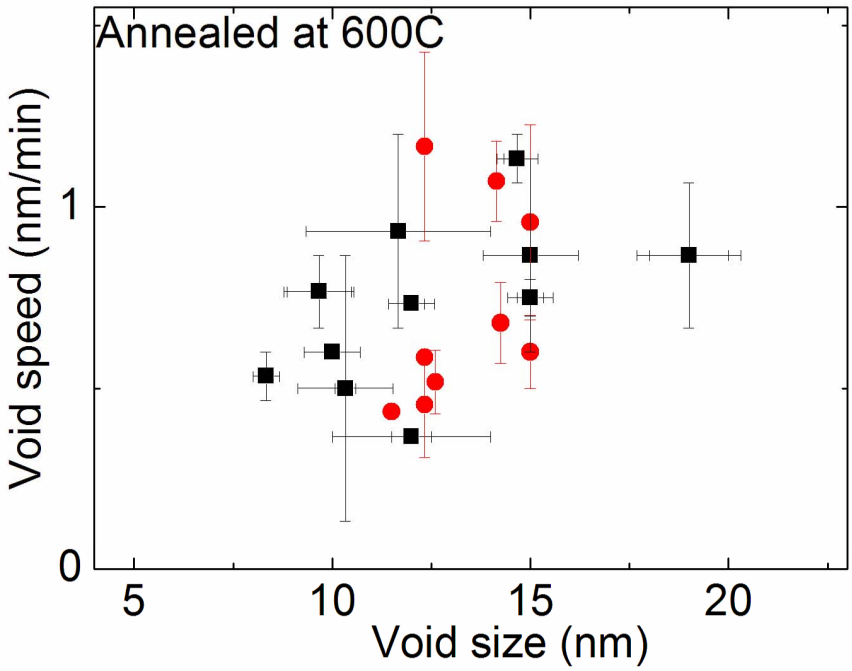

Figure 5.10: Void speed as a function of void width at annealing temperature of 600 °C.

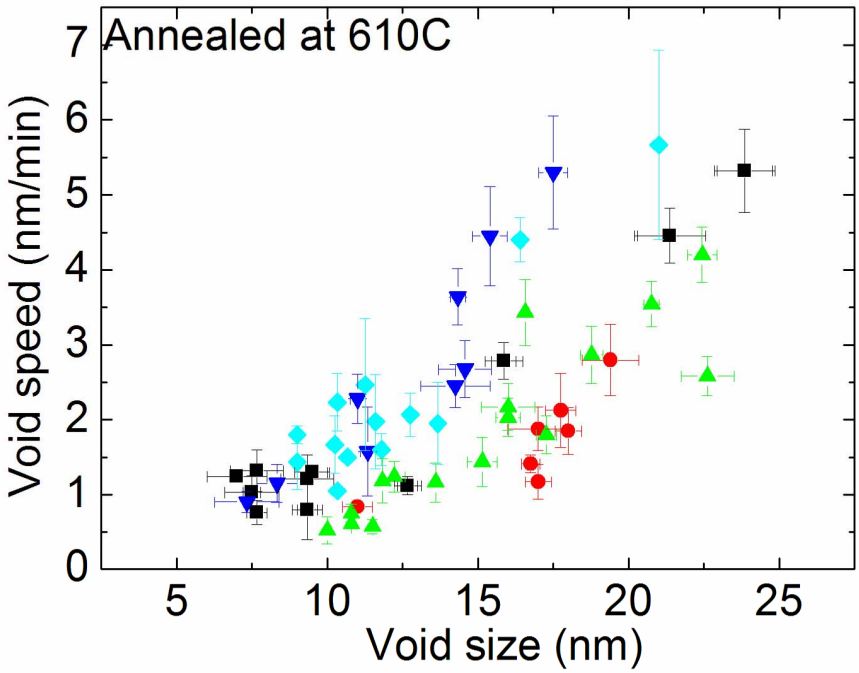

Figure 5.11: Void speed as a function of void width at annealing temperature of 610 °C.

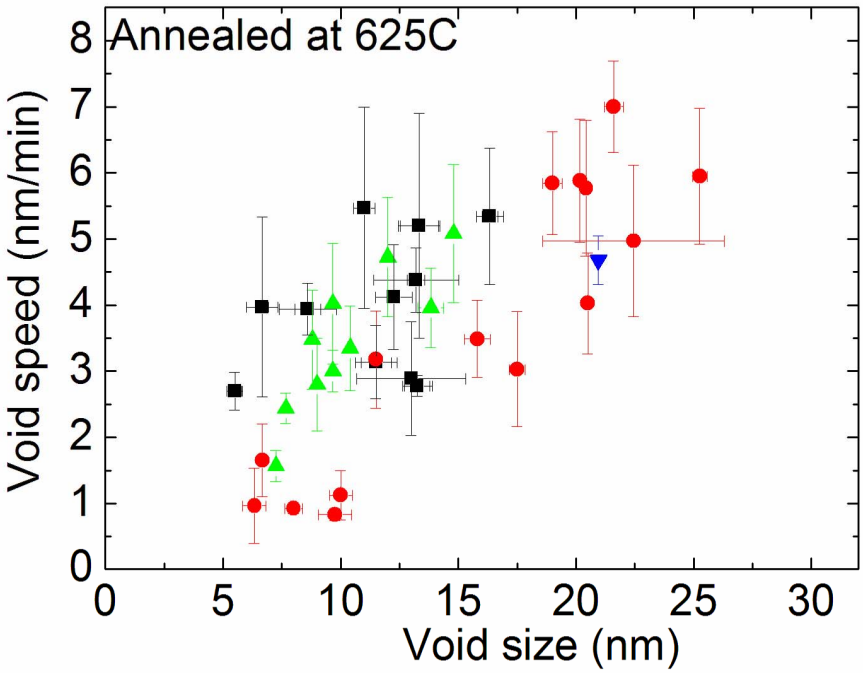

Figure 5.12: Void speed as a function of void width at annealing temperature of 625 °C.

atoms need to first diffuse along the inner surface by a diffusion event, then diffuse along the void tail to grow a layer of twin plane. The first process of surface diffusion of Si has a reported activation energy $E_{a,surf.diff}$ value around 2.38 eV [53], while the twin growth process has an activation energy $E_{a,twingrowth}$ value of 2.4 eV [87]. The follwoing Chapter 6 will compare the activation energy calculated from nanovoid speed with that measured from Raman crystallinity growth, which confirms that the mechanism of nanovoid enhanced crystallization.

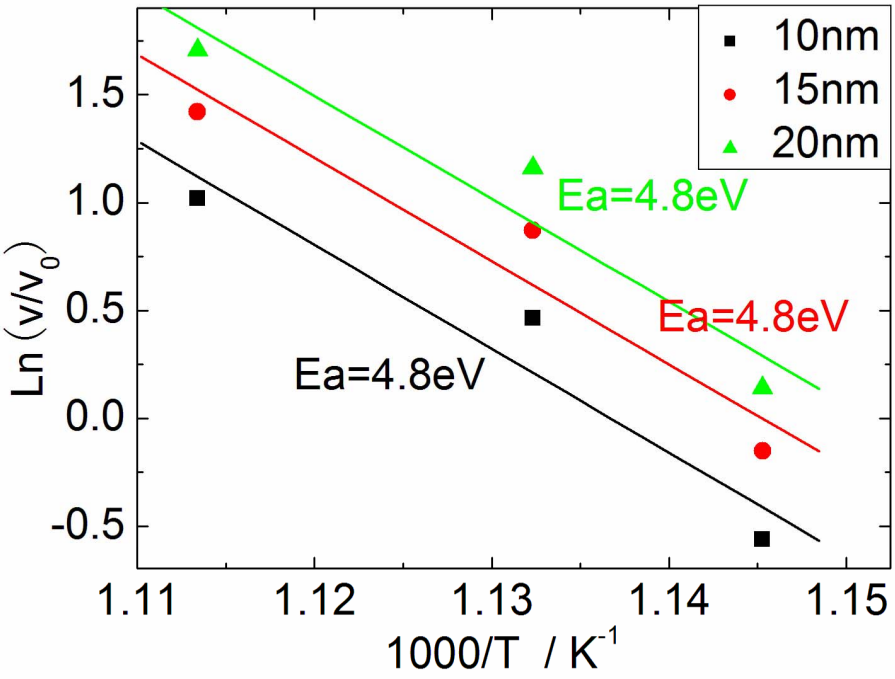

Figure 5.13: Arrehnius plots of the speed of nanovoid with size of 10-20 nm at 600-625 °C, indicating E_a of 4.8 eV.

Furthermore, Figure 5.14 measures the size distribution of all propagating nanovoids, excluding voids smaller than 5 nm which have speeds smaller than that of SPE and are

not observed to propagate. Most of the propagating voids have sizes between 5-20 nm, with voids larger than 20 nm seldomly observed. Two routes are expected to improve the crystallization enhancement involved by nanovoid propagation: either increasing nanovoid density or increasing nanovoid size.

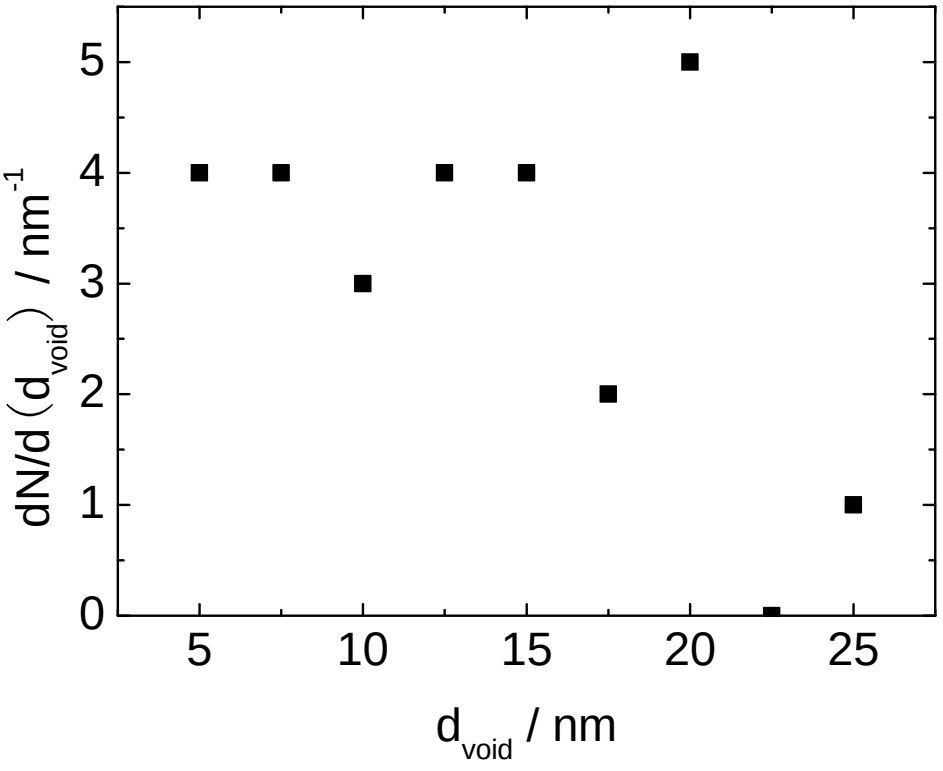

Figure 5.14: Size distribution of all propagating nanovoids.

Chapter 6

Nanovoid enhanced crystallization

6.1 Overview

This chapter focuses on the control of nanovoid enhanced crystallization. Formation of nanovoids is explained by the shadowing effect of seeds as well as film nanoporosity: high nanoporosity of amorphous films leads to high nanovoid density but in the meantime may impede void motion. On the other hand, seeding of spherical/multi-faceted nanoparticles also increases the void density by enhancing the shadowing effect, while the amorphous film could be kept at high density or low nanoporosity. Furthermore, this chapter develops a new structure of three-layer seeded films to control the nanovoid enhanced crystallization.

6.2 Film Nanoporosity

As discussed in Chapter 5, one of the origins of nanovoids is the coalescence of nanoporosity during film deposition. The density of the voids is expected to increase with film porosity. Previous studies have related the nanoporosity of amorphous silicon film with its medium range order (MRO), that is, 3-6 Å to as high as 15-25 Å from the nanoseeds [88].

In PECVD synthesis, it is believed that both gas-phase and surface reactions are controlled by the plasma properties, as the rapid potential drop in the plasma sheath region accelerates the ions to high energy towards the substrate. Film density can be tuned by various plasma properties, including deposition pressure, power density, deposition temperature and rf frequency, which vary the ion bombardment energy at film surface. For example, in the low deposition pressure regime around hundreds of mTorr, increasing pressure leads to a decrease of electron temperature, as the mean free path of electrons decreases and energy loss during collision increases, which further reduces the ion bombardment effect and produces low density film [89]. Power input is also strongly related to the amorphous film density. Lavareda *et al*. showed that higher power density contributes to lower film density in the power density region below 15 mW/cm^2 [90]. This is due to the fact that lower power density leads to high concentrations of SiH_3 radicals in the plasma. This reduces the void fraction in the film as SiH_3 has high diffusivity along the surface and fills the vacancies effectively, giving rise to more compact film growth. On the other hand, power density higher than 15 mW/cm^2 enhances ion bombardment effect, leading to much denser and more compressively stressed film.

Another plasma property that has influence on the film density is rf frequency. It is well-studied that ions do not respond to rf field at the high frequency of 13.56 MHz,

forming low density plasmas in which ion bombardment is less damaging, while at 100-350 kHz, ions rapidly respond to the rf field and give strong bombardment to growing film, thus producing denser films [91]. Furthermore, deposition temperature is related to the diffusivity of growth species at film surface and contributes to film nanoporosity as well. However this effect is not significant at deposition temperatures around 200-300 °C [92].

In this study, the effect of plasma pressure and power density is found to have direct impact on film density. As shown in Figure 6.1, the deposition rate is less than 30 Å/min at deposition pressure lower than 200 mTorr and there are no significant differences between the growth rate at 100 mTorr and 200 mTorr. The growth rate increases dramatically to greater than 100 Å/min at a pressure of 400 mTorr. Such a trend is consistent with previous work by Lavareda [91]. However, the deposition rate is still much lower than the industrial production rate (50-500 Å/min) [90].

The delivered power density has a positive correlation with film growth, also indicated in Figure 6.1. Not all of the rf power is consumed in the plasma discharge, most of which is lost as heat dissipation in the matching network. An MKS Alpha 0231 V-I probe is connected in series with the rf cable to monitor the real-time rf voltage, current and phase difference between voltage and current signal (ϕ), from which the power delivered to plasma is calculated as [48]:

$$P_{delivered} = VIcos\phi \tag{6.1}$$

It is calculated that approximately only 35-45% of total applied rf power is absorbed by the plasma. Under normal operation of argon or silane plasma (100-400 mTorr), the maximum applied power is restricted to below 25 W, above which arcing is observed during discharge, which has the potential to damage the plasma system. The delivered

rf power density has a range of 10-120 mW/cm^2, with the diameter of stainless steel electrode of 4 inches.

The growth rate of amorphous Si films increases roughly linearly with rf power at 100 mTorr and 200 mTorr, however, at 400 mTorr the increase is more significant, from only 11 Å/min at 10 mW/cm^2 up to 120 Å/min at 120 mW/cm^2. In addition, the increase in growth rate at 400 mTorr has an S-curve-like trend, that is, the growth rate has a large rise around 50 mW/cm^2 and it reaches saturated value below 25 mW/cm^2 as well as above 75 mW/cm^2.

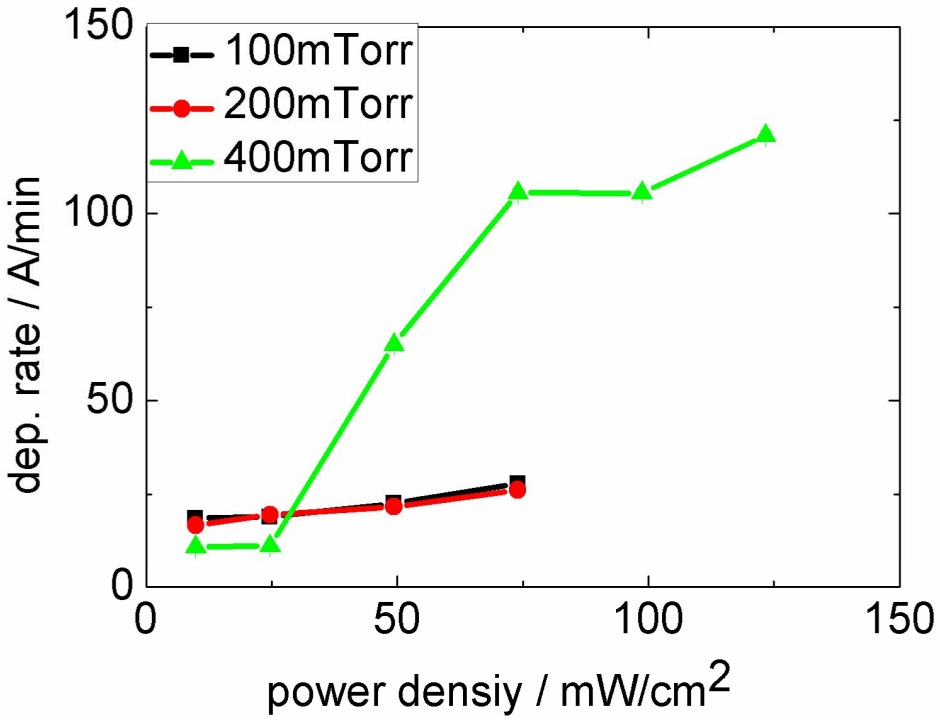

Figure 6.1: Deposition rate of a-Si:H films with increasing plasma pressure from 100 mTorr to 400mTorr and increasing delivered rf power from 10 mW/cm^2 to 120 mW/cm^2.

Film nanoporosity is measured by spectroscopic ellipsometry, a powerful tool to

analyze thin film thickness and other nanoproperties [93, 94]. Ellipsometry uses polarized light to characterize thin film surfaces and material nanostructure by analyzing the change of polarization of lights. With the H content around 8-12% in the seeded films, the nanoporosity is typically below 6% of the total volume. Figure 6.2 shows the improvement of H content and nanoporosity of a-Si:H films with increasing the power density. It is interesting to note that all the curves of deposition rate, H content and nanoporosity have the same S-curve-like trend, where the sharp rise always happens at around 50 mW/cm^2. Films deposited below 25 mW/cm^2 have low hydrogen content and nanoporosity with negative values arising from the error in measurement and modeling of ellipsometry fitting; while films at deposition power high than 75 mW/cm^2 have significantly higher porosity. Those films are therefore expected to show high nanovoid density under TEM annealing.

To study the effect of film nanoporosity on the nanovoid density, a-Si:H films deposited under varied power density and seeded with cubic nanocrystals are annealed in HSTEM. Figure 6.3 shows that films with higher nanoporosity or lower density exhibit higher density of nanovoids, as predicted. In films deposited at 10-25 mW/cm^2, which have nanoporosity close to 0%, the void density is much less than 1 nanovoid per seed. Films deposited above 50 mW/cm^2, whose nanoporosity rises up to 10-12%, have nanovoid formation at the boundary of almost every seed. It is noticeable that films formed under 125 mW/cm^2 have the highest void density, which gives a greater chance of observing large-sized nanovoids.

The increased void density eventually enhances crystallization upon annealing. Figure 6.4 presents the HSTEM experiment of seeded film deposited under power density of 25 mW/cm^2, which has extremely low nanoporosity. Almost no nanovoids form in HSTEM, leading to only epitaxy growth of nanoseeds and thus no nanovoid enhanced

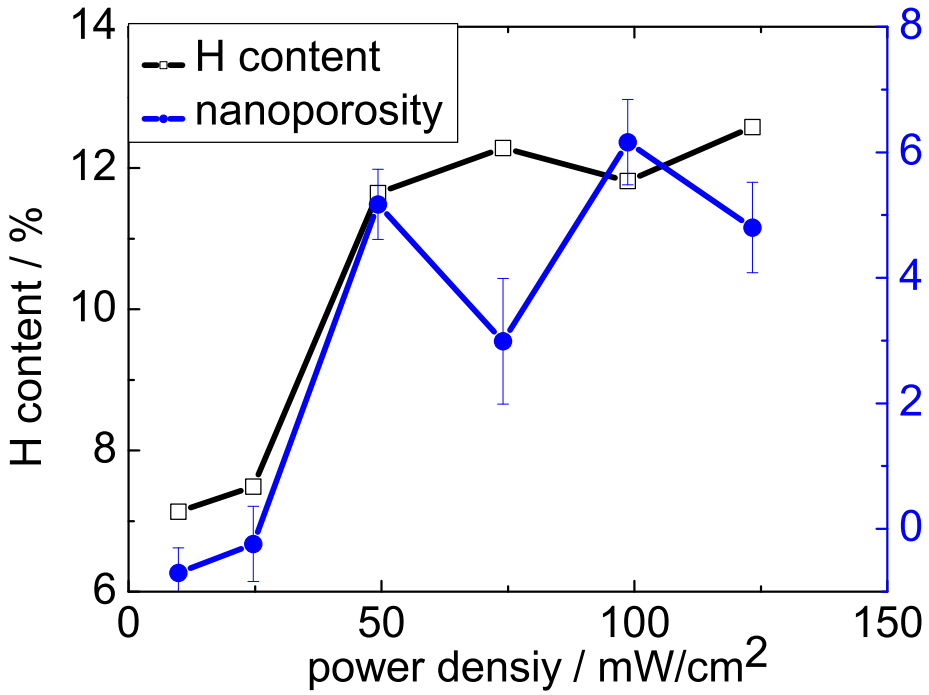

Figure 6.2: H content and nanoporosity of a-Si:H films with increasing delivered rf power from 10 mW/cm^2 to 120 mW/cm^2. The deposition pressure is fixed at 400 mTorr.

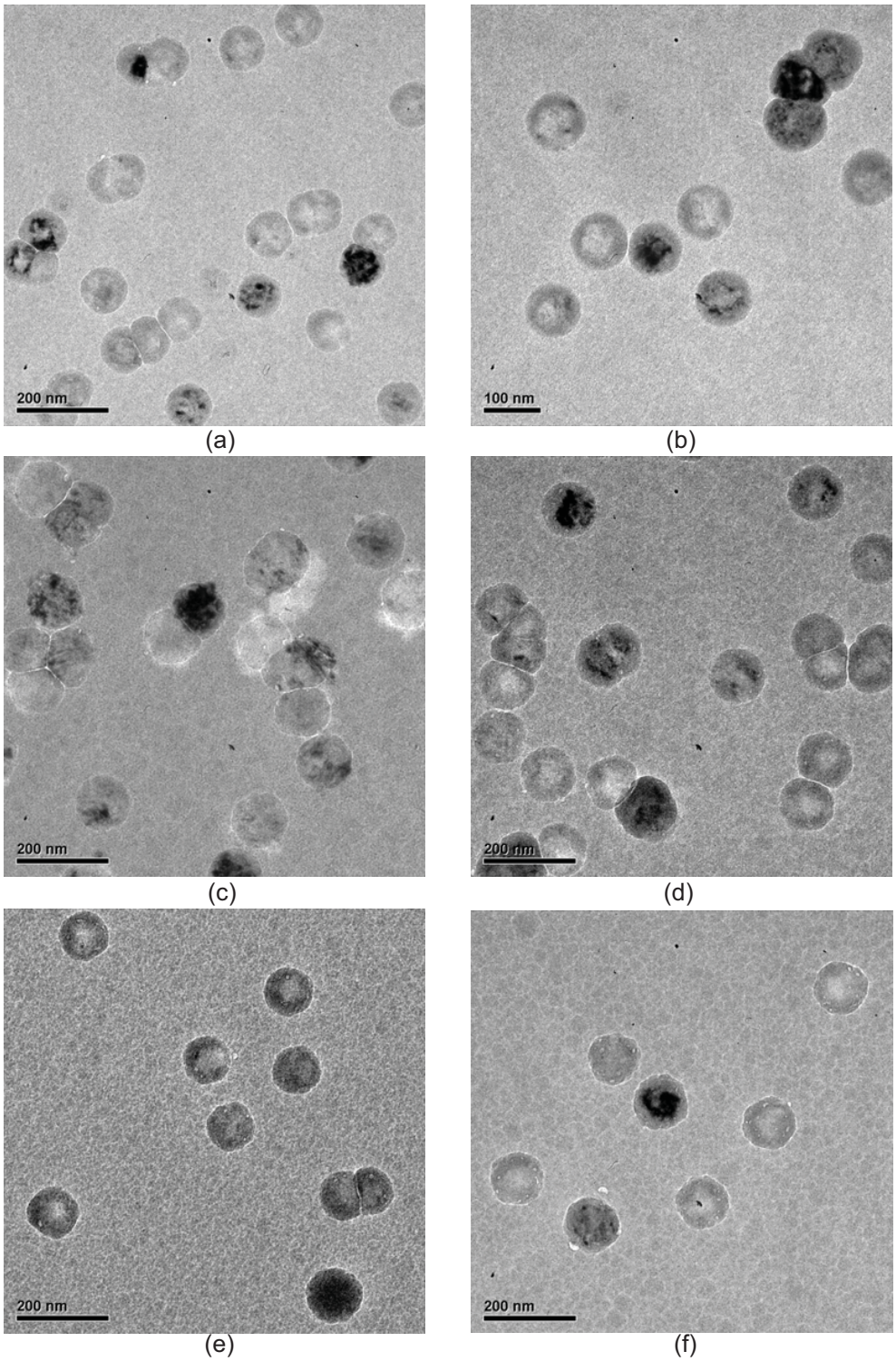

Figure 6.3: TEM images of seeded film deposited at various power density, showing varied nanovoid density. (a): power density (P_{rf}) = 10 mW/cm^2, annealing temperature (T_a) = 625 °C, annealing time (t_a) = 10 min; (b): P_{rf} = 25 mW/cm^2, T_a = 625 °C, t_a = 10 min; (c): P_{rf} = 50 mW/cm^2, T_a = 625 °C, t_a = 15 min; (d): P_{rf} = 75 mW/cm^2, T_a = 610 °C, t_a = 20 min; (e): P_{rf} = 100 mW/cm^2, T_a = 600 °C, t_a = 15 min; (f): P_{rf} = 125 mW/cm^2, T_a = 610 °C, t_a = 10 min.

crystallization. In comparison, films deposited at 125 mW/cm^2 has nanoporosity as high as 12% and shows significant nanovoid propagation. Although nanovoids in Figure 6.5 move through the film at the beginning stage of annealing, they always become trapped at a propagation displacement less than 200-400 nm.

It is consistently observed in TEM that voids in high nanoporosity films fail to provide substantial enhancement of crystallization, due to the significantly increased SPE of nanoseeds. This observation is supported by the hydrogen effusion theory [95]. During pre-annealing around 550-600 °C, the hydrogen present in nanovoids/divacancies starts to diffuse out of the film, restructuring the amorphous network in the process. Therefore, as-deposited films with higher nanoporosity undergo larger structural transitions to a more compact structure. This eventually leads to a more ordered film structure and causes higher epitaxy growth of the film. In other words, although high nanoporosity improves void density, it also inhibits the outgrowth of the voids. Figure 6.6 compares the speed of void propagation with that of solid phase epitaxy growth from the seeds, both measured using ImageJ software. It is clearly observable that voids under 10 nm in length have speeds less than the average speed of epitaxy growth. Even nanovoids over 15 nm propagate less than 2 times faster than the seed growth.

Such an effect is further revealed by time-series Raman annealing experiments. Samples prepared with plasma power density of 10-125 mW/cm^2 and pressure of 400 mTorr are deposited onto Corning glass substrate and annealed at 625 °C and 650 °C. Results from these are shown in Figure 6.7 and Figure 6.8. Similar to the S-curve-like trend shown in Figure 6.1 and Figure 6.2, films with deposition power higher than 50 mW/cm^2 show significant improvement of crystallization rate than the low power samples, which is consistent with significantly higher void density observed in TEM annealing experiments. Furthermore, increased nanovoid density largely increases the

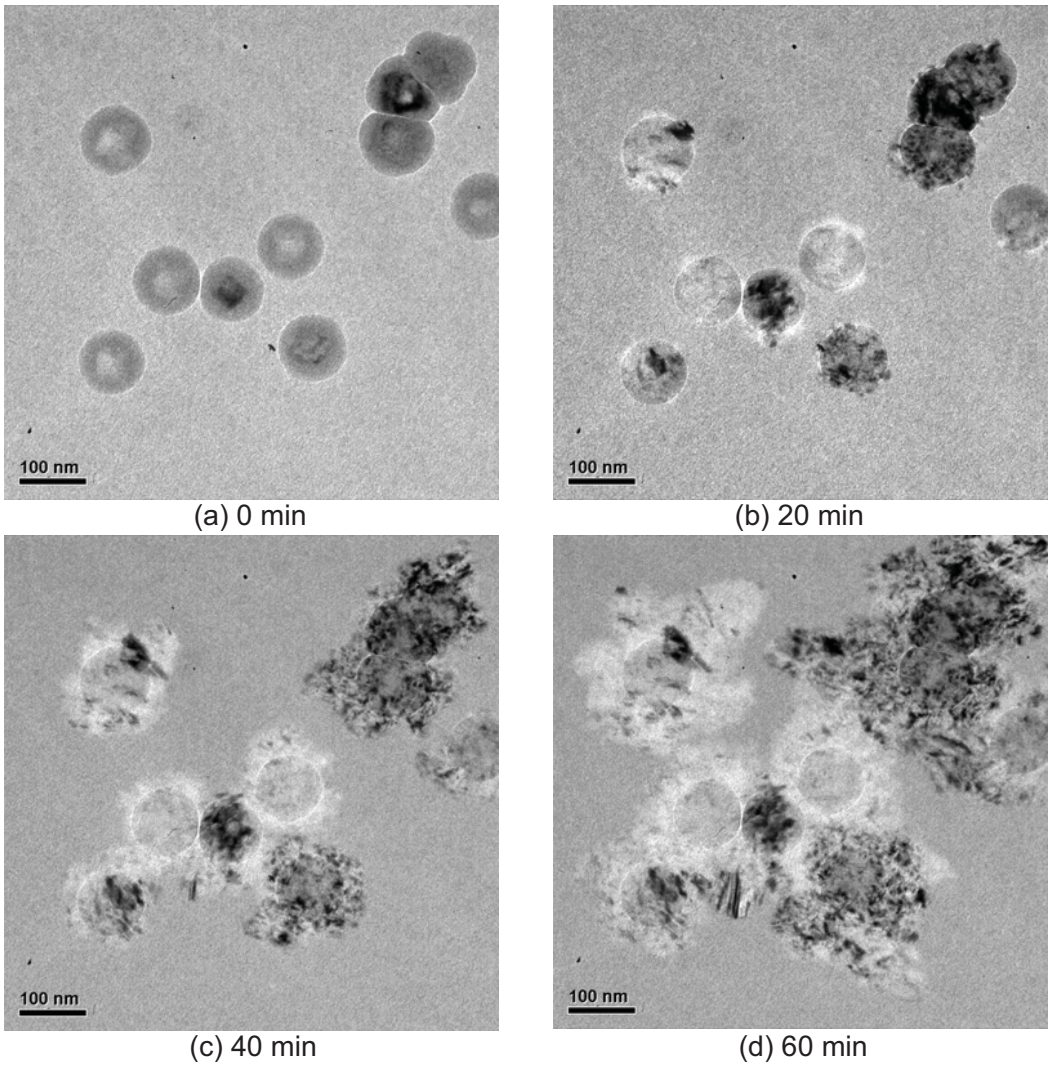

Figure 6.4: Time series images of HSTEM annealing at 625 °C of seeded film deposited at 25 mW/cm^2, indicating few nanovoids formation thus no nanovoid enhanced crystallization effect.

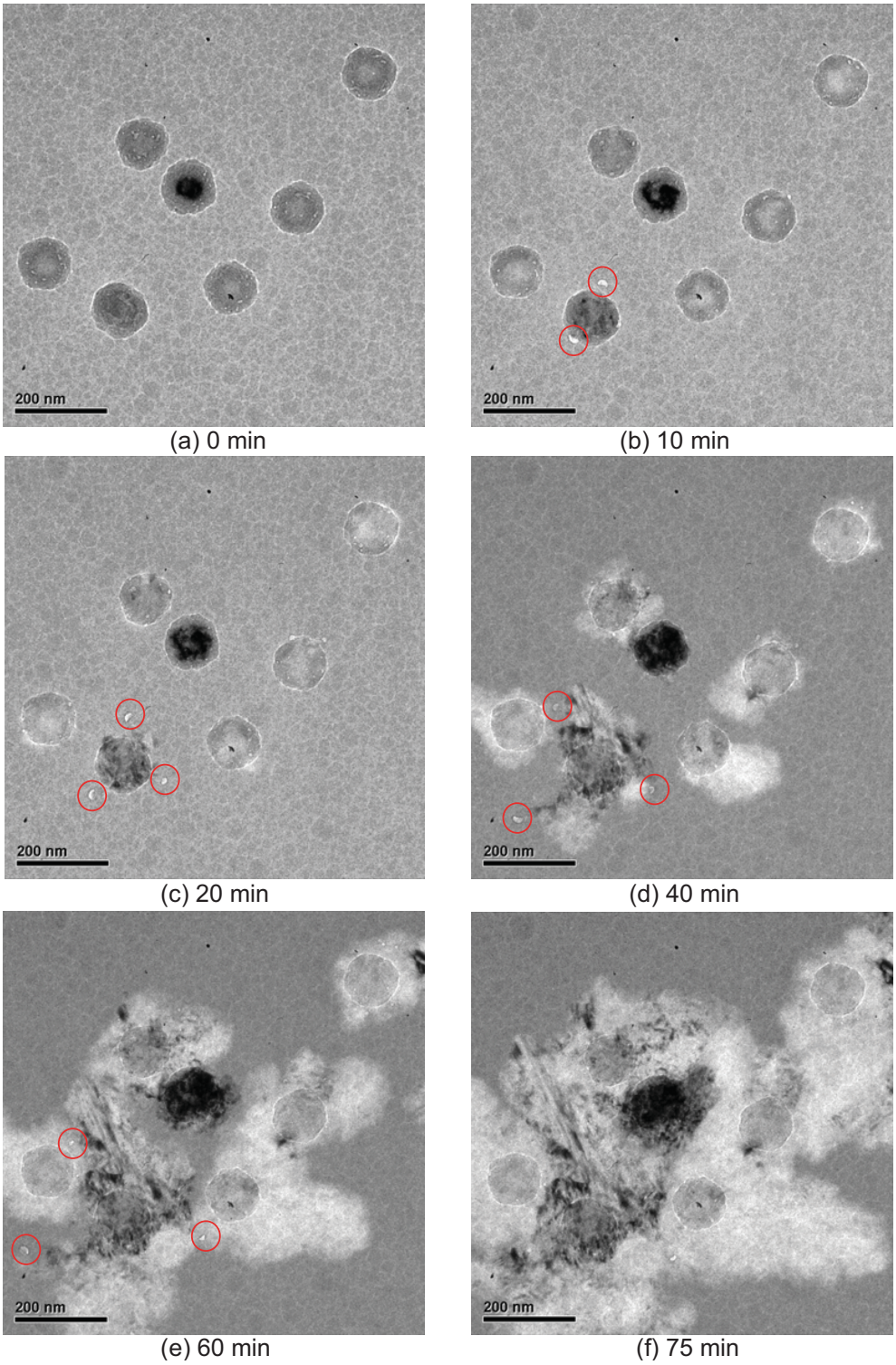

Figure 6.5: Time series images of HSTEM annealing at 610 °C of seeded film deposited at 125 mW/cm^2, indicating significant nanovoid formation and moderate nanovoid enhanced crystallization effect. Some propagating voids are circled in red.

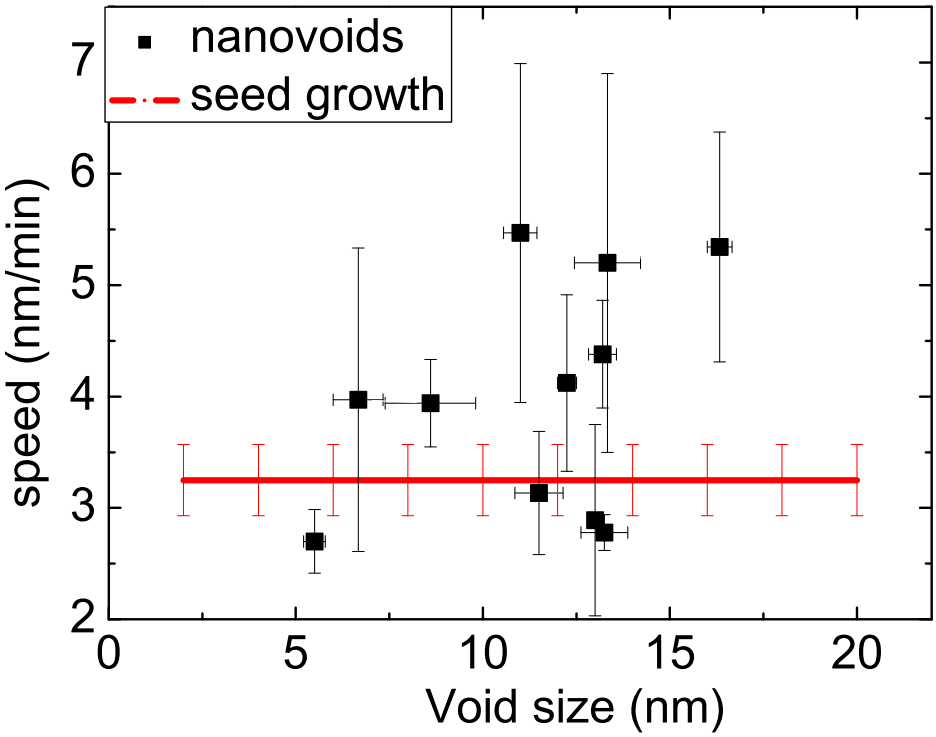

Figure 6.6: Comparison of nanovoid propagation speeds with seed SPE speed, measured from Figure 6.5, indicating void speed is at most two times the seed growth rate.

area of crystallization growth fronts by the tail region of voids, which further contributes to the overall crystallization mechanism.

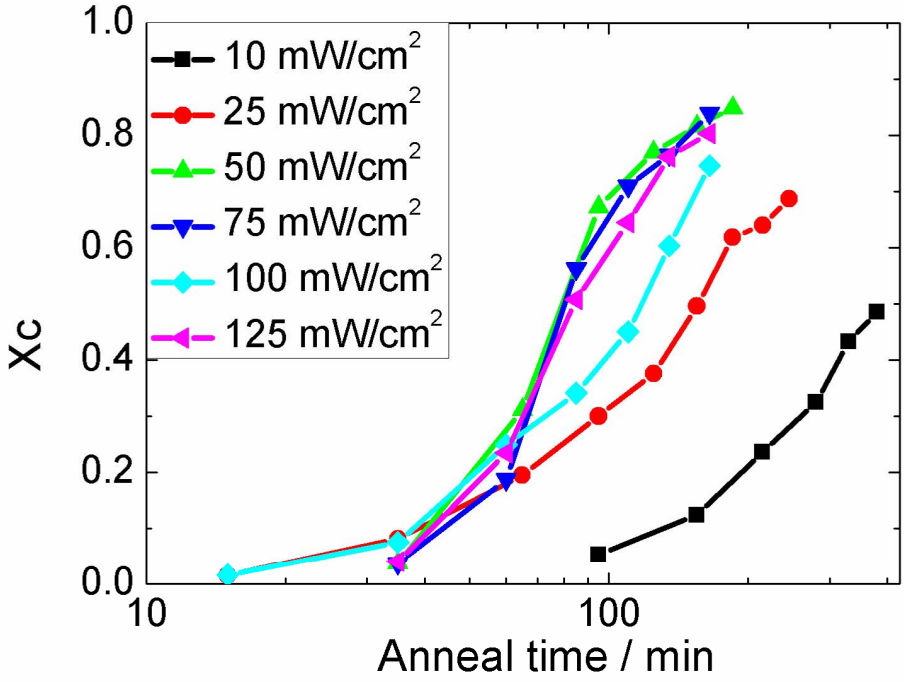

Figure 6.7: Time-series of Raman crystallinity of seeded film annealed at 625 °C, showing enhanced crystallization rate due to void propagation for films deposited under power density higher than 25 mW/cm^2.

The growth mechanism of seeded a-Si:H films is further studied by analyzing the characteristic crystallization time, t_c, and the Avrami coefficient n [96]. Characteristic crystallization time represents the time at which sample reaches a crystal fraction of $1 - 1/e = 0.63$. Figure 6.9 plots t_c as a function of annealing temperature and input rf power. It is easy to observe that higher annealing temperature leads to higher crystallization rates, indicating a smaller value of t_c. Under a fixed annealing temperature, t_c decreases as power increases, a trend consistent with Figure 6.7 and Figure 6.8. At annealing

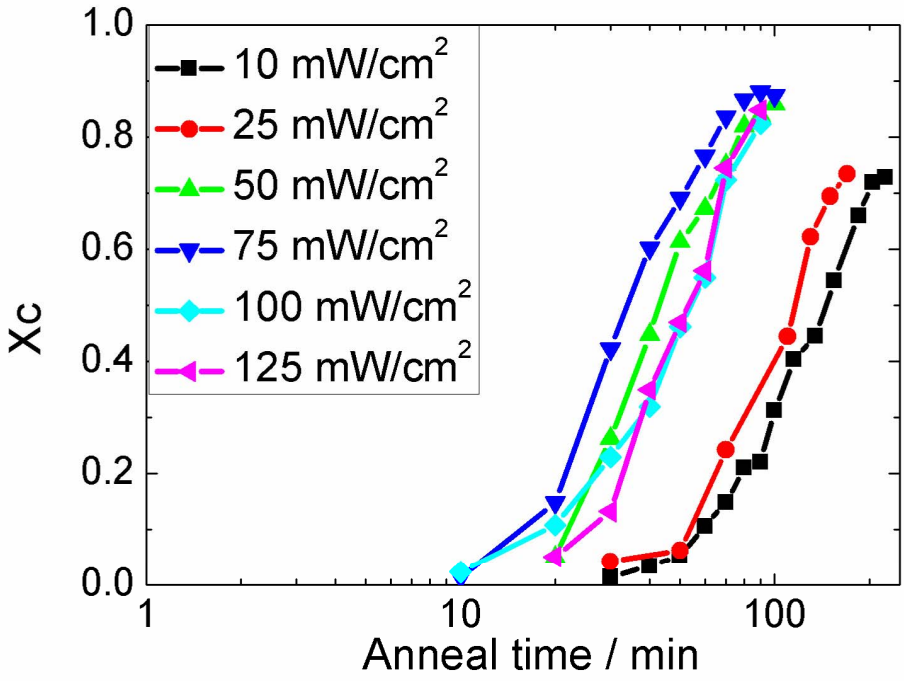

Figure 6.8: Time-series of Raman crystallinity of seeded film annealed at 650 °C, showing enhanced crystallization rate due to void propagation for films deposited at power density higher than 50 mW/cm^2.

temperatures of 625 °C and 650 °C, the decrease is very slow (from 200-400 min down to 100 min), while at 600 °C, the decrease is more significant (1400 min to 400 min), with power rising from 10 mW/cm^2 to 75 mW/cm^2, respectively. Crystallization time always reaches the saturation value above 75 mW/cm^2. Such decreases in t_c is another indication that density of nanovoids increases in high power films which contributes to enhanced crystallization kinetics.

Figure 6.10 calculates the Avrami coefficient n of seeded films annealed at 625 °C and 650 °C with deposition power of 10-125 mW/cm^2. The S-curve trend suggests different growth mechanisms for low and high power films. Films deposited below 50 mW/cm^2 show formation of very few nanovoids, supported by previous HSTEM and Raman experiments. Therefore only SPE of nanoseeds dominates the crystallization process in these cases, indicated by a n value around 1.5-2.5. By contrast, films deposited under power higher than 50 mW/cm^2 show the existence of high nanovoid density, with growth kinetics resulting from a combination of seed growth with low n value and additional nanovoid propagation adding more growth fronts, dictated by a n value over 3.

6.3 Three-layer Film

One way to address the competition between seed growth and nanovoid propagation described in the last section is to deposit one layer of film with high nanoporosity only adjacent to the nanoseeds and a second layer of film with low nanoporosity in the bulk away from the seeds, to suppress the expitaxy growth. This idea is achieved by a three-layer structure, shown in Figure 6.11. The main difference between this new seeded film structure and the traditional two-layer structure is that the top layer is composed of two layers deposited with different input rf power: after embedding seeds onto the surface

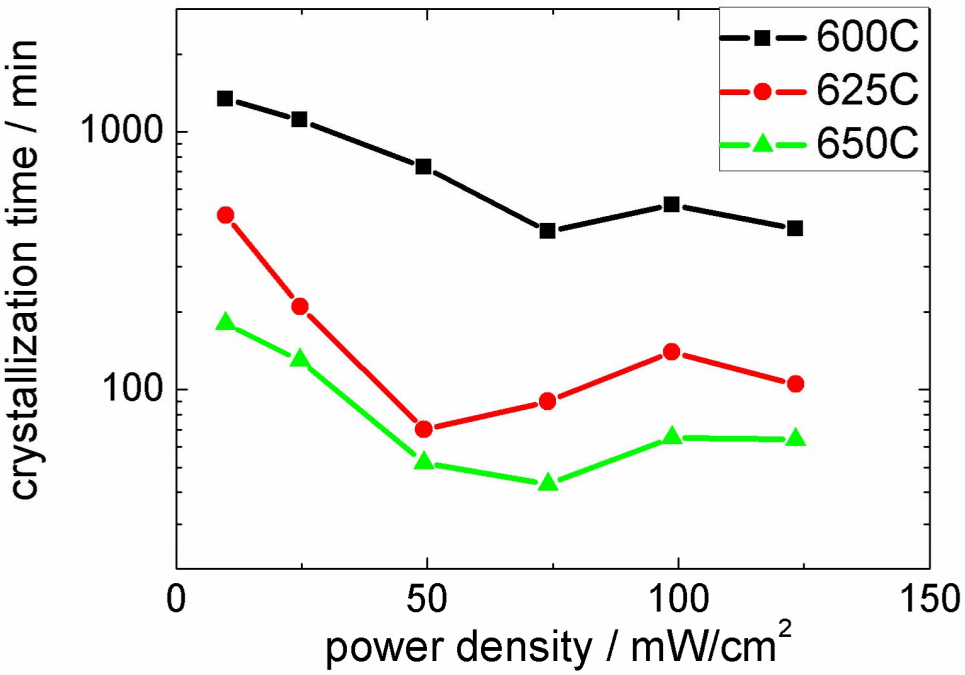

Figure 6.9: Measurement of characteristic crystallization time at different annealing temperature of seeded film deposited at power density of 10-125 mW/cm^2.

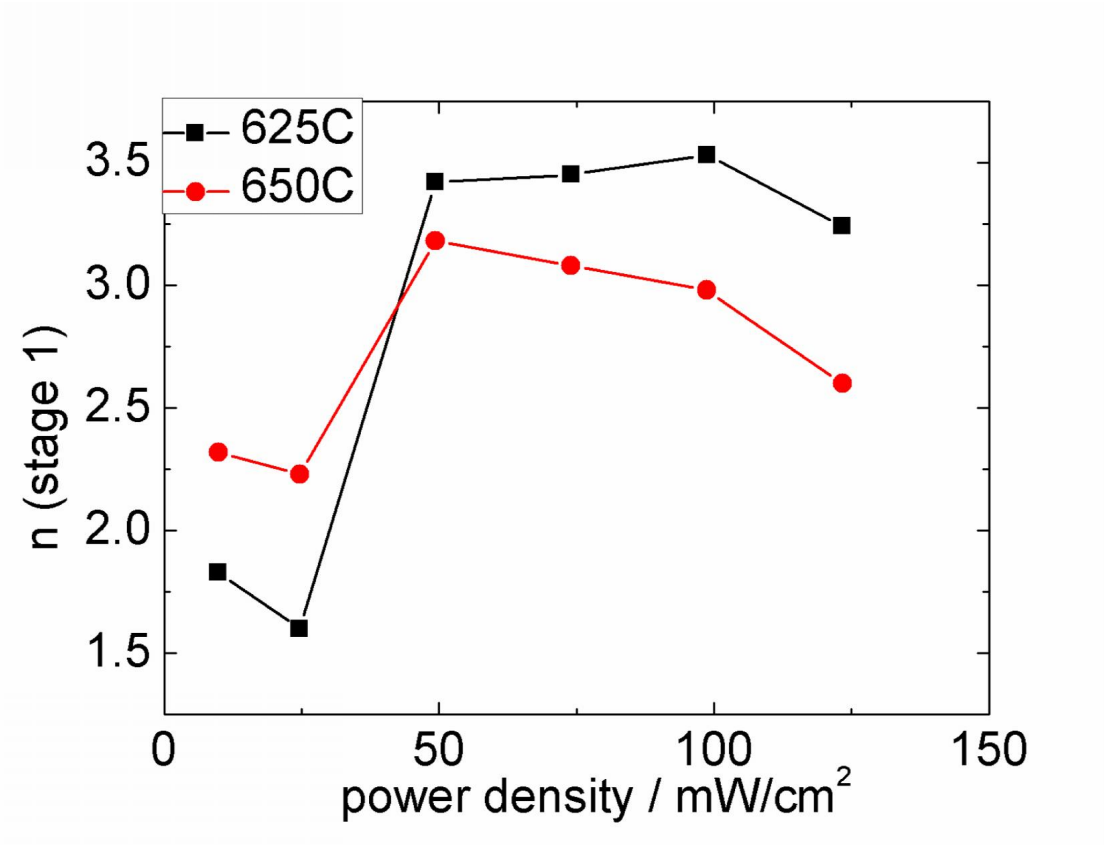

Figure 6.10: Plot of Avrami coefficient n as a function of annealing temperature and power density.

of 20 nm sub-layer, a thin layer a-Si:H film is deposited, typically at a thickness of 20 nm near the seeds which is close to the maximum size of nanovoids, with high power (larger than 25 mW/cm^2) which enables the void formation. Afterwards, another thick top layer is capped under 10 mW/cm^2 which creates a dense bulk film that inhibits the normal grain growth. Such structure does not increase the complexity of production, since the deposition of top layers is easily achieved by simply increasing the rf power.

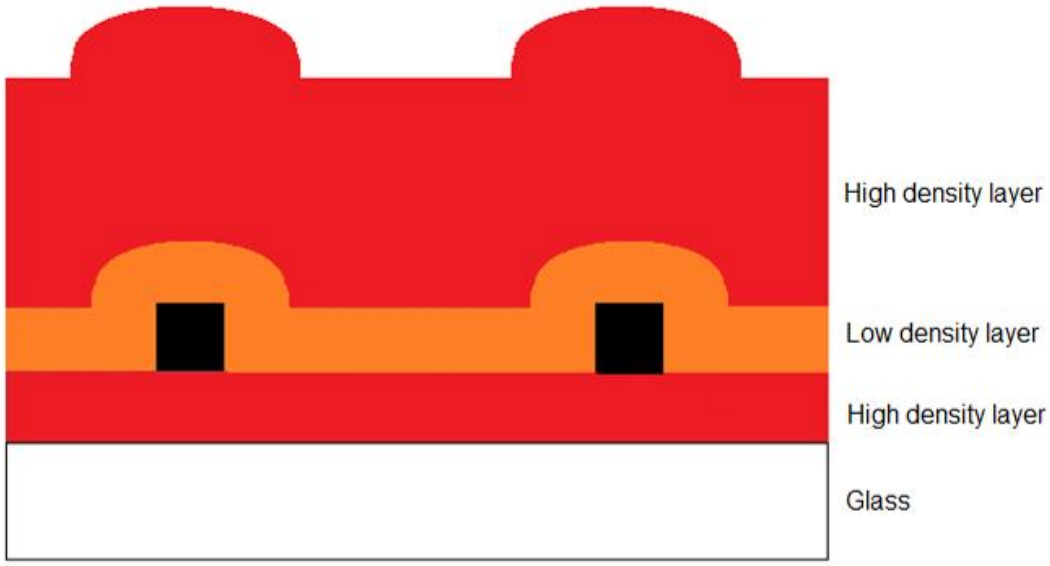

Figure 6.11: Sketch of three-layer structure of seeded films.

Three-layer structured films are deposited onto Mo TEM grids and analyzed under HSTEM annealing. Figure 6.12 (a) shows that nanovoids of high density form under annealing due to the high nanoporosity region around the nanoseeds. The average void

density is greater than 4 voids per seed and almost all seeds have at least one nanovoid large enough to propagate upon annealing. Since the bulk of the amorphous region has relatively low nanoporosity as well as low hydrogen content, the normal SPE growth is suppressed, supported by the comparison of nanovoid speed with SPE speed in Figure 6.13. Compared to Figure 6.6, the SPE speed is reduced from over 3 nm/min to 1 nm/min. The void speed remains almost the same, as both samples are annealed under the same temperature. Therefore, three-layer film structure enables the increase in nanovoid (with a size around 20 nm) speed up to over 5 times higher than the seed growth. Furthermore, even voids with size less than 10 nm still have comparable speed to SPE growth, therefore those small-sized voids are less likely to get trapped during annealing.

Raman annealing of three-layer samples deposited on glass substrate shows higher crystallization rate than the corresponding two-layer films, shown in Figure 6.14. The three-layer film composed of films deposited at applied power of 2 W and 5W has crystallization rate significantly higher than two-layer films deposited at applied power of 2 W and 5W, respectively. Therefore such three-layer method improves the total crystallization rate in terms of prominence of nanovoid enhanced crystallization kinetics.

6.4 Spherical Seeds

As the origin of the nanovoids is explained by both film nanoporosity and the shadowing effect of nanoparticles, another way to improve the nanovoid enhanced crystallization effect is to implant spherical (or non-cubic) nanoparticles into the film, which would provide enhanced shadowing effect. Spherical particles are synthesized as described in Chapter 3.

Spherical nanocrystal seeded films are deposited on Mo TEM grids and analyzed

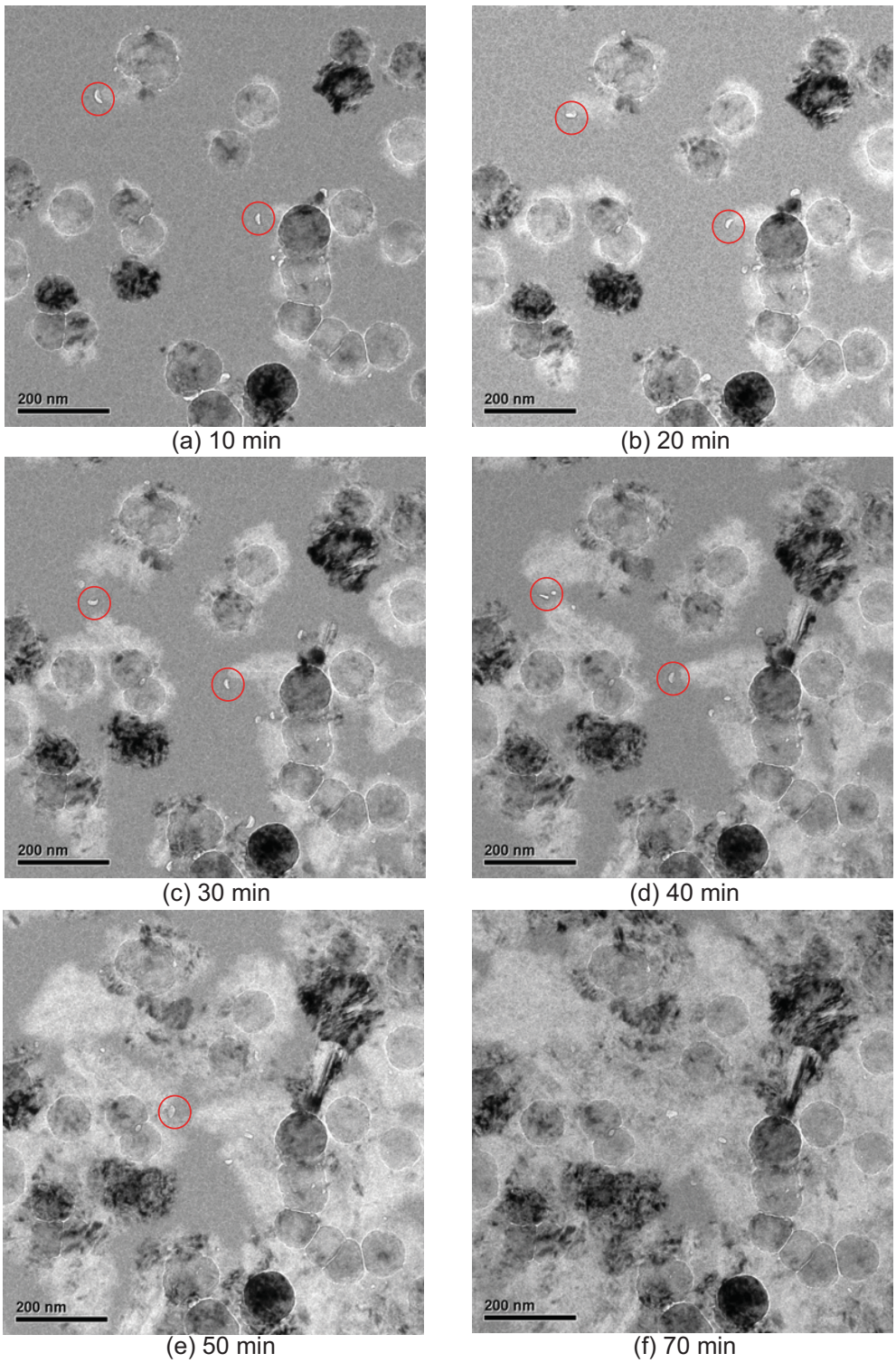

Figure 6.12: Time series images of HSTEM annealing at 625 °C of three-layer seeded film, indicating significant nanovoids formation and nanovoid enhanced crystallization effect. Some propagating voids are circles in red.

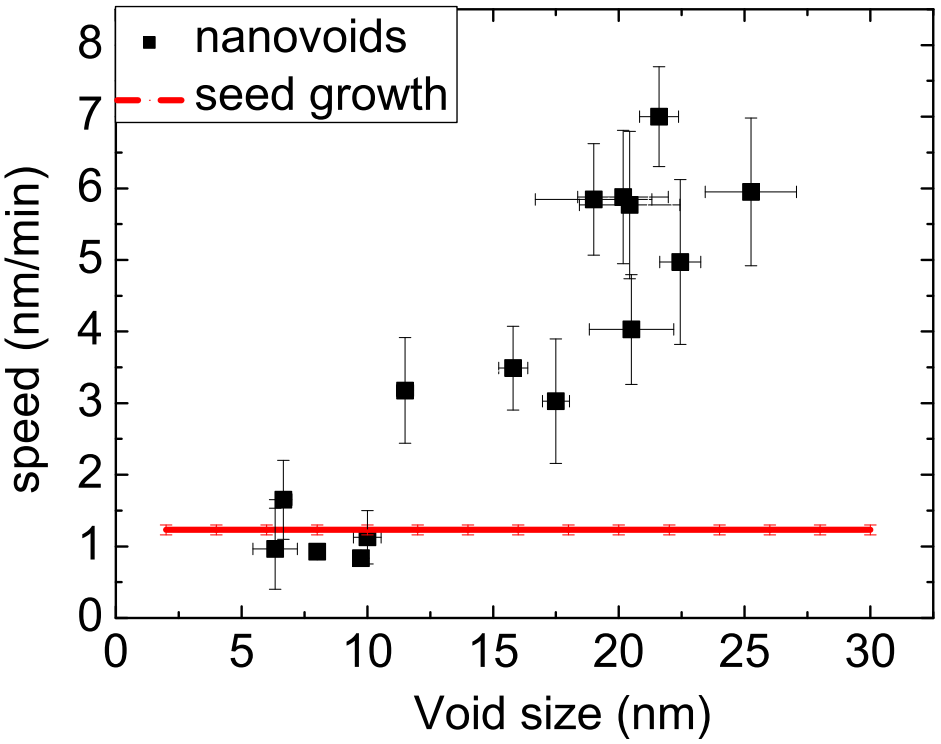

Figure 6.13: Comparison of nanovoid propagation speed with seed SPE speed, measured from Figure 6.12, indicating that void speed is at most six times greater than seed growth rate.

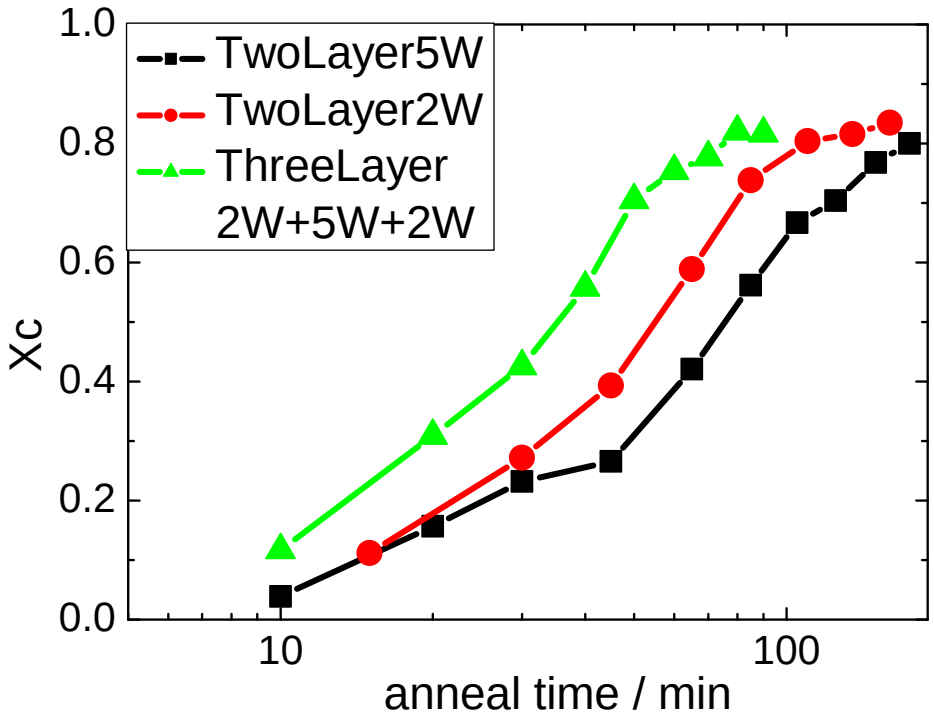

Figure 6.14: Time-series of Raman crystallinity of three-layer seeded film annealed at 625 °C, showing enhanced crystallization rate over two-layer seeded films.

under HSTEM annealing. Figure 6.15 shows the time-series images of HSTEM annealing at 625 °C of spherical nanoparticle seeded film. While the density of the voids is not as high compared to the three-layer structured film, more large sized nanovoids (over 15 nm) are observed, although voids smaller than 5 nm in size are easily trapped by the seed growth. The formation of large nanovoids is due to the stronger shadowing effect caused by non-vertical walls of the spherical nanoseeds. Another important feature of spherical nanoparticle seeded films is that the void propagation speed is remarkable compared to the normal grain growth, as shown in Figure 6.16. The nanovoid speed at size of over 15 nm is up to 6 times higher than the slow seed epitaxy growth. Therefore the introduction of the spherical particles improves the nanovoid enhanced crystallization, in terms of forming large sized nanovoids while the bulk film is still kept at low nanoporosity.

Figure 6.17 shows the Raman crystallinity curve of spherical particle seeded films annealed at 600-650 °C, describing a clear trend of temperature-driven crystallization behavior. Figure 6.18 expresses the Arrhenius plots of the characteristic crystallization time of three different kinds of films, including two-layer cubic nanocrystal seeded films deposited under low rf power density of 10 mW/cm^2 where no nanovoids are observed, two-layer cubic nanocrystal seeded films deposited under high rf power density of 125 mW/cm^2 where high density of nanovoids exists, and two layer spherical nanocrystal seeded films deposited under low rf power density of 10 mW/cm^2 where large nanovoids are presented. Activation energy (E_a) calculated from the slope of Arrhenius curves further indicates the growth kinetics:

$$1/t_c = 1/t_{c0} e^{-\frac{E_a}{kT}} \tag{6.2}$$

Since almost no nanovoids exists within two-layer cubic nanocrystal seeded film deposited under low rf power, its Arrhenius growth curve shows an E_a value of 2.7 eV,

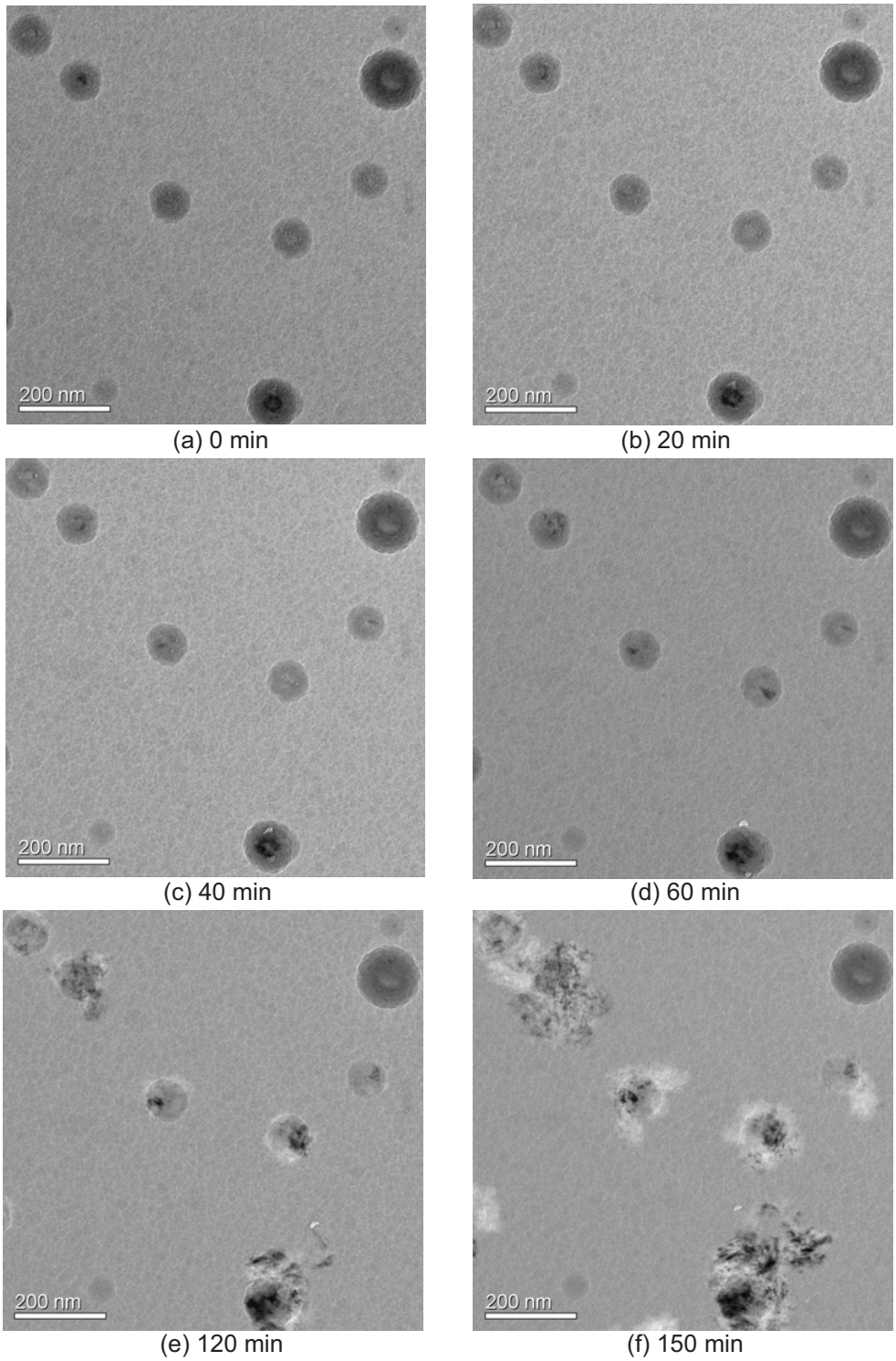

Figure 6.15: Time series images of HSTEM annealing at 625 °C of spherical nanoparticle seeded film, indicating significant nanovoid speed compared to seed epitaxy growth.

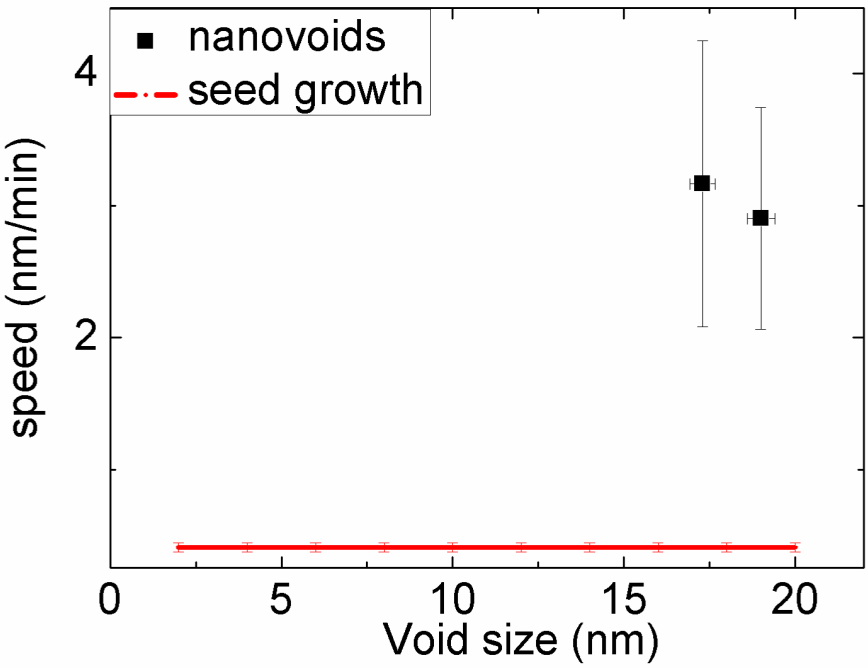

Figure 6.16: Comparison of nanovoid propagation speed with seed SPE speed, measured from Figure 6.15, indicating void speed is up to six times greater than seed growth rate.

consistent with that of normal epitaxy growth [53]. Spherical nanocrystal seeded films show strongly dominant nanovoid enhanced crystallization kinetics, thus obtaining the higher E_a value of 4.4 eV, very close to the activation energy of void motion, $E_{a,void}$, reported in Chapter 5 (4.8 eV). Cubic nanocrystal seeded films deposited at high rf power show less significant void propagation compared to the seed epitaxy growth and has an intermediate E_a value of 3.2 eV.

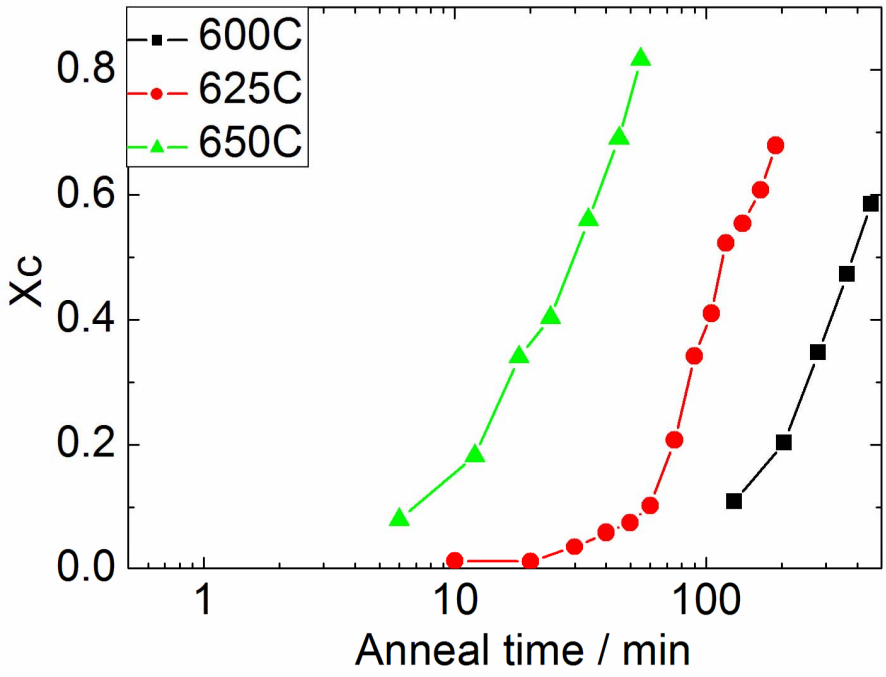

Figure 6.17: Time-series of Raman crystallinity of two-layer spherical nanoparticle seeded film annealed at 600-650 °C.

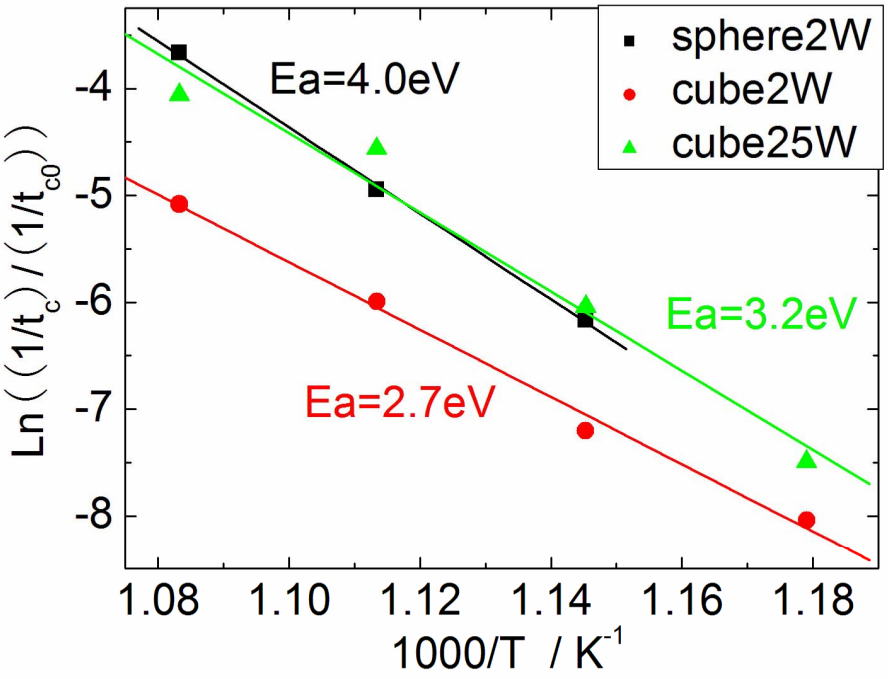

Figure 6.18: Arrhenius plot of crystallization time of different film structures at 600-650 °C: two-layer cubes seeded film deposited under low 2 mW, two-layer cubes seeded film deposited under 25 mW and two layer sphere seeded film under 25 mW

Chapter 7

Conclusion

7.1 Summary

This work studies a new approach to synthesizing μc-Si:H with a lower thermal budget and better control of the microstructure, with potentially larger grain sizes. This unique technique uses a low-pressure radio-frequency plasma reactor to synthesize silicon nanocrystals and embed them into a-Si:H matrix, where they serve as starting points for crystal grain growth upon thermal annealing. Such film structure enables the decoupling of the deposition parameters for amorphous and crystallite components. The implantation of nanocrystal seeds reduces the total crystallization time by eliminating the incubation period. Final grain size in "fully" crystallized films is controlled by the initial seed concentration, which further tunes the electrical properties of the microcrystalline film.

Raman spectroscopy observes a trend of increasing crystallization rate with decreasing seed density, explained as an effect due to the short range disorder of amorphous

matrix with more seed inclusion. A two-stage growth model and the Kolmogorov-Johnson-Mehl-Avrami model indicate growth kinetics of the seeded film as initial grain growth originated from the seeds and a following stage after the growth fronts collide with each other. Hydrogen is believed to be a key factor in the crystallization process, as films with low microstructure parameter exhibit substantial enhancement of crystallization. The evolution of the stress during annealing is also studied while a transition of large tensile stress is observed.

Further heated stage TEM experiments show the formation of nanovoids at the interface between the nanoseeds and the amorphous matrix after annealing temperatures reach 580 °C. Nanovoids propagate through the film at a speed higher than normal grain growth rate of nanoseeds and leave a crystalline region behind, leading to the nanovoid enhanced crystallization effect. The formation of nanovoids is related to film nanoporosity as well as the shadowing effect of the nanoparticles. The void propagates due to a combined effect of atomic surface diffusion at its inner surface and the twin growth at its tail region.

The density of nanovoids increases with the film nanoporosity. As such, seeded films deposited under high rf power density shows growth kinetics of combined void propagation with normal epitaxy growth. The embedding of spherical nanocrystals also improves the void density by enhancing the shadowing effect, while the amorphous film can be kept at low nanoporosity. Furthermore, an alternative deposition scheme is developed, in which a three-layer structured seeded film enables independent control of nanovoid density and the epitaxy growth of the nanoseeds.

7.2 Future Work

The existence of nanovoids enhanced crystallization of a-Si:H by adding additional growth fronts, however the final film may exhibit smaller grain sizes due to the generation of twin boundaries in the tail region of nanovoids, which may further limit the charge carrier mobility of the crystallized film. Further study to compromise between these two effects, together with efforts to control the void motion in order to achieve more homogenous distribution of grain sizes, would be beneficial to the application of the layer-by-layer method in PV industry.

The implantation of silicon nanoparticles can be repeated in other semiconductor nanomaterials, such as germanium (Ge). It would be interesting to seed Ge nanoparticles into Si film or introduce Si nanoseeds into amorphous Ge matrix as both materials have similar lattice constants, and the nanovoid formation and propagation are expected to be observed again.

References

[1] K. Branker, M. Pathak, and J. M. Pearce. A review of solar photovoltaic levelized cost of electricity. *Renewable and Sustainable Energy Reviews*, 15(9):4470–4482, December 2011.

[2] Sultan Ahmed, Al Jaber, Manfred Konukiewitz, Robert Dixon, Michael Eckhart, David Hales, and Griffin Thompson. Renewables 2011. 2011.

[3] Sultan Ahmed, Al Jaber, Robert Dixon, Michael Eckhart, Griffin Thompson, and David Hales. Renewables 2012. 2012.

[4] Vasilis Fthenakis and Erik Alsema. Photovoltaics energy payback times, greenhouse gas emissions and external costs: 2004 to early 2005 status. 2006.

[5] H. S. Ullal and B. Von Roedern. Thin film CIGS and CdTe photovoltaic technologies: commercialization, critical issues, and applications preprint. 2007.

[6] Amy H. I. Lee, Hsing Hung Chen, and He-Yau Kang. A model to analyze strategic products for photovoltaic silicon thin-film solar cell power industry. *Renewable and Sustainable Energy Reviews*, 15(2):1271–1283, February 2011.

[7] Martin A. Green. Thin-film solar cells: review of materials, technologies and commercial status. *Journal of Materials Science: Materials in Electronics*, 18(S1):15–19, April 2007.

[8] W. Van Sark, G. W. Brandsen, M. Fleuster, and M. P. Hekkert. Analysis of the silicon market: Will thin films profit? *Energy Policy*, 35(6):3121–3125, June 2007.

[9] V. M. Fthenakis and H. C. Kim. Photovoltaics: Life-cycle analyses. *Solar Energy*, 85(8):1609–1628, August 2011.

[10] Guy Beaucarne. Silicon thin-film solar cells. *Advances in OptoElectronics*, 2007:1–12, 2007.

[11] Armin Aberle. Thin-film solar cells. *Thin Solid Films*, 517(17):4706–4710, July 2009.

[12] M. Fehr, A. Schnegg, B. Rech, K. Lips, O. Astakhov, F. Finger, C. Freysoldt, R. Bittl, and C. Teutloff. Dangling bonds in amorphous silicon investigated by multifrequency EPR. *Journal of Non-Crystalline Solids*, pages 10–13, January 2012.

[13] A. Kolodziej. Staebler-Wronski effect in amorphous silicon and its alloys. *Science And Technology*, 12(1):21–32, 2004.

[14] D. Beeman. Structural information from the Raman spectrum of amorphous silicon. *Physical Review B*, 32(2):874, 1985.

[15] Aniekan Magnus Ukpong. Computer simulation of the influence of hydrogen on stress-order correlations in amorphous silicon. *Molecular Simulation*, 35(5):395–404, April 2009.

[16] K. Sharma, M. A. Verheijen, M. C. M. Van de Sanden, and M. Creatore. In situ crystallization kinetics studies of plasma-deposited, hydrogenated amorphous silicon layers. *Journal of Applied Physics*, 111(3):033508, 2012.

[17] D. Drabold, T. Abtew, F. Inam, and Y. Pan. Network structure and dynamics of hydrogenated amorphous silicon. *Journal of Non-Crystalline Solids*, 354(19-25):2149–2154, May 2008.

[18] G. Mensing, J. Gilligan, P. Hari, E. Hurt, G. Lupke, S. Pantelides, N. Tolk, and P. C. Taylor. Defect transition energies and the density of electronic states in hydrogenated amorphous silicon. *Journal of Non-Crystalline Solids*, 299-302:621–625, April 2002.

[19] Kazunori Koga, Toshihisa Inoue, Kouki Bando, Shinya Iwashita, Masaharu Shiratani, and Yukio Watanabe. Highly stable a-Si:H films deposited by using multi-hollow plasma chemical vapor deposition. *Japanese Journal of Applied Physics*, 44(No. 48):L1430–L1432, November 2005.

[20] Ihsanul Afdi Yunaz, Kenji Hashizume, Shinsuke Miyajima, Akira Yamada, and Makoto Konagai. Fabrication of amorphous silicon carbide films using VHF-PECVD for triple-junction thin-film solar cell applications. *Solar Energy Materials and Solar Cells*, 93(6-7):1056–1061, June 2009.

[21] Giovanni Bruno. *Plasma Deposition Of Amorphous Silicon-Based Materials*. 1995.

[22] Guy Turban. Basic phenomena in reactive low pressure plasmas used for deposition and etching. *Pure and Applied Chemistry*, 56(2), 1984.

[23] E. A. G. Hamers, A. Fontcuberta, C. Niikura, R. Brenot, and P. Roca. Contribution

of ions to the growth of amorphous, polymorphous, and microcrystalline silicon thin films. *Journal of Applied Physics*, 88(6):3674, 2000.

[24] Michael A. Lieberman. *Principles of Plasma Discharges and Materials Processing*. 2005.

[25] S. Gall, C. Becker, K.Y. Lee, T. Sontheimer, and B. Rech. Growth of polycrystalline silicon on glass for thin-film solar cells. *Journal of Crystal Growth*, 312(8):1277–1281, April 2010.

[26] O. Vetterl, F. Finger, R. Carius, P. Hapke, L. Houben, O. Kluth, A. Lambertz, A. Muck, B. Rech, and H. Wagner. Intrinsic microcrystalline silicon: A new material for photovoltaics. *Solar Energy Materials and Solar Cells*, 62(1-2):97–108, April 2000.

[27] J. Meier, F. L. Fliickiger, H. Keppner, and A. Shah. Complete microcrystalline behavior p-i-n solar cell-Crystalline or amorphous cell behavior? *Applied Physics Letters*, 65(7):860–862, 2000.

[28] Chan-Do Park, Hae-Yeol Kim, Min-Hee Cho, Kuk-Jin Jan, and Jai-Young Lee. Solid-phase crystallization of hydrogenated amorphous silicon/hydrogenated microcrystalline silicon bilayers deposited by plasma-enhanced chemical vapor deposition. *Thin Solid Films*, 359(2):268–274, January 2000.

[29] C. Becker, E. Conrad, P. Dogan, F. Fenske, B. Gorka, T. Hanel, K. Y. Lee, B. Rau, F. Ruske, and T. Weber. Solid-phase crystallization of amorphous silicon on ZnO:Al for thin-film solar cells. *Solar Energy Materials and Solar Cells*, 93(6-7):855–858, June 2009.

[30] T. Matsuyama. High-quality polycrystalline silicon thin film prepared by a solid phase crystallization method. *Journal of Non-Crystalline Solids*, 198-200:940–944, May 1996.

[31] Romyani Goswami, Biswajit Chowdhury, and Swati Ray. Solid phase crystallization of protocrystalline silicon films: Changes in structural and optical properties. *Thin Solid Films*, 516(8):2306–2313, February 2008.

[32] K. Brendel, N. H. Nickel, P. Lengsfeld, A. Schopkea, I. Siebera, M. Nerdingb, H. P. Strunkb, and W. Fuhs. Excimer laser crystallization of amorphous silicon on metal coated glass substrates. *Thin Solid Films*, 427(1-2):86–90, March 2003.

[33] N. Sinh. Optimization of layered laser crystallization for thin-film crystalline silicon solar cells. *Solar Energy Materials and Solar Cells*, 74(1-4):295–303, October 2002.

[34] Tae Y. Choi, David J. Hwang, and Costas P. Grigoropoulos. Ultrafast laser-induced crystallization of amorphous silicon films. *Optical Engineering*, 42(11):3383, 2003.

[35] C. C. Tsai, R. Thompson, and B. L. Stafford. Metal-induced crystallization of hydrogenated amorphous Si films. *Physica B*, pages 953–955, 1983.

[36] A. Behnam, F. Karbassian, S. Mohajerzadeh, A. Ebrahimi, and M. Robertson. Low-temperature nickel-induced nano-crystallization of silicon on PET by MIC, hydrogenation and mechanical stress. *Solid-State Electronics*, 50(9-10):1618–1624, September 2006.

[37] E. Korin, R. Reif, and B. Mikic. Crystallization of amorphous silicon films using a multistep thermal annealing process. *Thin Solid Films*, 167(1-2):101–106, December 1988.

[38] M. Hakim, I. Matko, B. Chenevier, and P. Ashburn. Lateral crystallization of amorphous silicon by germanium seeding. *Microelectronic Engineering*, 83(11-12):2437–2440, November 2006.

[39] A. T. Voutsas, M. K. Hatalis, J. Boyce, and A. Chiang. Raman spectroscopy of amorphous and microcrystalline silicon films deposited by low-pressure chemical vapor deposition. *Journal of Applied Physics*, 78(12):6999, 1995.

[40] Ingrid De Wolf. Micro-Raman spectroscopy to study local mechanical stress in silicon integrated circuits. *Semiconductor Science and Technology*, 139, 1996.

[41] C. Smit, R. Van Swaaij, H. Donker, A. Petit, W. Kessels, and M. Van de Sanden. Determining the material structure of microcrystalline silicon from Raman spectra. *Journal of Applied Physics*, 94(5):3582–3588, 2003.

[42] R. Saleh and N. H. Nickel. Raman spectroscopy of B-doped microcrystalline silicon films. *Thin Solid Films*, 427(1-2):266–269, March 2003.

[43] Curtis Anderson. *PhD Thesis: Enhanced Crystallization of Amorphous Silicon Thin Films Using Embedded Silicon Nanocrystals.* PhD thesis, University of Minnesota, 2008.

[44] R. D. Verda, J. R. Tesmer, M. Nastasi, and R. W. Bower. Accurate hydrogen depth profiling by reflection elastic recoil detection analysis. *Nuclear Instruments and Methods in Physics Research Section B: Beam Interactions with Materials and Atoms*, 190(1-4):419–422, May 2002.

[45] R. B. Wehrspohn, S. C. Deane, I. D. French, I. Gale, J. Hewett, M. J. Powell, and J. Robertson. Relative importance of the Si-Si bond and Si-H bond for the stability

of amorphous silicon thin film transistors. *Journal of Applied Physics*, 87(1):144, 2000.

[46] Cyril Aubaud, Helene Bureau, Caroline Raepsaet, Hicham Khodja, Anthony C. Withers, Marc M. Hirschmann, and David R. Bell. Calibration of the infrared molar absorption coefficients for H in olivine, clinopyroxene and rhyolitic glass by elastic recoil detection analysis. *Chemical Geology*, 262(1-2):78–86, May 2009.

[47] Ameya Bapat, Christopher R. Perrey, Steven A. Campbell, and Uwe Kortshagen. Synthesis of highly oriented, single-crystal silicon nanoparticles in a low-pressure, inductively coupled plasma. *Journal of Applied Physics*, 94(3):1969, 2003.

[48] Ameya Bapat, Curtis Anderson, Christopher R Perrey, C Barry Carter, Stephen A Campbell, and Uwe Kortshagen. Plasma synthesis of single-crystal silicon nanoparticles for novel electronic device applications. *Plasma Physics and Controlled Fusion*, 46(12B):B97–B109, December 2004.

[49] Ryan Gresback, Zachary Holman, and Uwe Kortshagen. Nonthermal plasma synthesis of size-controlled, monodisperse, freestanding germanium nanocrystals. *Applied Physics Letters*, 91(9):093119, 2007.

[50] Ameya Bapat, Marco Gatti, Yong-Ping Ding, Stephen Campbell, and Uwe Kortshagen. A plasma process for the synthesis of cubic-shaped silicon nanocrystals for nanoelectronic devices. *Journal of Physics D: Applied Physics*, 40(8):2247–2257, April 2007.

[51] Pere Roca I Cabarrocas, Anna Fontcuberta I Morral, Sarra Lebib, and Yves Poissant. Plasma production of nanocrystalline silicon particles and polymorphous

silicon thin films for large-area electronic devices. *Pure and Applied Chemistry*, 74(3):359–367, 2002.

[52] Fang-Mei Tseng, Chih-Hung Hsieh, Ya-Ni Peng, and Yi-Wei Chu. Using patent data to analyze trends and the technological strategies of the amorphous silicon thin-film solar cell industry. *Technological Forecasting and Social Change*, 78(2):332–345, February 2011.

[53] Corrado Spinella, Salvatore Lombardo, and Francesco Priolo. Crystal grain nucleation in amorphous silicon. *Journal of Applied Physics*, 84(10):5383, 1998.

[54] A. Mahan, S. Ahrenkiel, R. Schropp, H. Li, and D. Ginley. A comparison of grain nucleation and grain growth during crystallization of HWCVD and PECVD a-Si:H films. *Thin Solid Films*, 516(5):529–532, January 2008.

[55] G. L. Olson. Kinetics of solid phase crystallization amorphous silicon. *Materials Science Reports*, 3(May):1–78, 1988.

[56] E. Bardet. The grain size in microcrystalline silicon: correlation between atomic force microscopy, UV reflectometry, ellipsometry, and X-ray diffractometry. *Journal of Non-Crystalline Solids*, 198-200:867–870, May 1996.

[57] M. Avrami. Kinetics of phase change. I. General theory. *Journal of Chemical Physics*, 7:1103–1112, 1939.

[58] M. Avrami. Kinetics of phase change. II. Transformation-time relations for random distribution of nuclei. *Journal of Chemical Physics*, 8:212–224, 1940.

[59] Blair Tuttle and James Adams. Energetics of hydrogen in amorphous silicon: An ab initio study. *Physical Review B*, 57(20):12859–12868, May 1998.

[60] E. Spanakis. Elastic properties, intrinsic and photoinduced stress in hydrogenated amorphous silicon thin films with different hydrogen content. *Journal of Applied Physics*, 89:4294–4300, 2001.

[61] B. Pan. Simulation of hydrogen evolution from nano-crystalline silicon. *Journal of Non-Crystalline Solids*, 333(1):44–47, January 2004.

[62] D. M. Goldie and S. K. Persheyev. Quantitative hydrogen measurements in PECVD and HWCVD a-Si:H using FTIR spectroscopy. *Journal of Materials Science*, 41(16):5287–5291, June 2006.

[63] G. Cerofolini, L. Meda, R. Balboni, F. Corni, S. Frabboni, G. Ottaviani, R. Tonini, M. Anderle, and R. Canteri. Hydrogen-related complexes as the stressing species in high-fluence, hydrogen-implanted, single-crystal silicon, July 1992.

[64] N. Budini, P. A. Rinaldi, J. A. Schmidt, R. D. Arce, and R. H. Buitrago. Influence of microstructure and hydrogen concentration on amorphous silicon crystallization. *Thin Solid Films*, 518(18):5349–5354, July 2010.

[65] W. Beyer. Incorporation and thermal stability of hydrogen in amorphous silicon and germanium. *Journal of Non-Crystalline Solids*, 198-200:40–45, May 1996.

[66] W. Beyer. Solubility and diffusion of hydrogen in hydrogenated crystalline and amorphous silicon. *Journal of Non-Crystalline Solids*, 227-230:880–884, May 1998.

[67] J. P. Harbison, A. J. Williams, and D. V. Lang. Effect of silane dilution on intrinsic stress in glow discharge hydrogenated amorphous silicon films. *Journal of Applied Physics*, 55(4):946, 1984.

[68] M. Hossain, H. Abusafe, H. Naseem, and W. Brown. Characterization of hydrogenated amorphous silicon thin films prepared by magnetron sputtering. *Journal of Non-Crystalline Solids*, 352(1):18–23, January 2006.

[69] Jungwon Park, Seyeoul Kwon, Seung-Ik Jun, Ilia N. Ivanov, Jinbo Cao, Janice L. Musfeldt, and Philip D. Rack. Stress induced crystallization of hydrogenated amorphous silicon. *Thin Solid Films*, 517(11):3222–3226, April 2009.

[70] V. Paillard, P. Puech, M. A. Laguna, P. Temple-Boyer, B. Caussat, J. P. Couderc, and B. de Mauduit. Resonant Raman scattering in polycrystalline silicon thin films. *Applied Physics Letters*, 73(12):1718, 1998.

[71] Thanh Nga Nguyen, Van Duy Nguyen, Sungwook Jung, and Junsin Yi. Raman scattering analysis of the residual stress in metal-induced crystallized amorphous silicon thin films using nickel. *Applied Surface Science*, 255(19):8252–8256, July 2009.

[72] P. Temple-Boyer, E. Scheid, G. Faugere, and B. Rousset. Residual stress in silicon films deposited by LPCVD from disilane. *Thin Solid Films*, 310(1-2):234–237, November 1997.

[73] V. Koleshko, V. Belitsky, and I. Kiryushin. Stress relaxation in thin aluminium films. *Thin Solid Films*, 142(2):199–212, September 1986.

[74] M. Tane, S. Nakano, R. Nakamura, H. Ogi, M. Ishimaru, H. Kimizuka, and H. Nakajima. Nanovoid formation by change in amorphous structure through the annealing of amorphous Al2O3 thin films. *Acta Materialia*, 59(11):4631–4640, June 2011.

[75] C. Godet, N. Layadi, and P. Roca. Role of mobile hydrogen in the amorphous silicon recrystallization. *Applied Physics Letters*, 66(23):3146, 1995.

[76] S. Hara, S. Izumi, T. Kumagai, and S. Sakai. Surface energy, stress and structure of well-relaxed amorphous silicon: A combination approach of ab initio and classical molecular dynamics. *Surface Science*, 585(1-2):17–24, July 2005.

[77] S. J. Clark. Very low energy surface of silicon. *Physical Review B*, 15(8):5728, 1994.

[78] Ant Ural, P. B. Gri, and J. D. Plummer. Nonequilibrium experiments on self-diffusion in silicon at low temperatures using isotopically enriched structures. 274:512–515, 1999.

[79] Shu-Zu Lu and Angus Hellawell. Growth mechanisms of silicon in Al-Si alloys. *Journal of Crystal Growth*, 73:316–328, 1985.

[80] J. M. Sallese, A. Ils, D. Bouvet, P. Fazan, and Chris Merritt. Modeling of the depletion of the amorphous-silicon surface during hemispherical grained silicon formation. *Journal of Applied Physics*, 88(10):5751, 2000.

[81] Andrew S. Dalton, Yevgeniy V. Kondratenko, and Edmund G. Seebauer. Diffusion mechanisms on amorphous silicon surfaces. *Chemical Engineering Science*, 65(6):2172–2176, March 2010.

[82] A. Dalton, D. Llera-Hurlburt, and E. Seebauer. Surface diffusion kinetics on amorphous silicon. *Surface Science*, 494(1):L761–L766, November 2001.

[83] Kentaro Kutsukake, Takuro Abe, Noritaka Usami, Kozo Fujiwara, Kohei Morishita, and Kazuo Nakajima. Formation mechanism of twin boundaries during crystal growth of silicon. *Scripta Materialia*, 65(6):556–559, September 2011.

[84] Johan Pohl, Michael Muller, Albrecht Seidl, and Karsten Albe. Formation of parallel (111) twin boundaries in silicon growth from the melt explained by molecular dynamics simulations. *Journal of Crystal Growth*, 312(8):1411–1415, April 2010.

[85] L. F. Mattheiss and J. R. Patel. Electronic stacking-fault states in silicon. *Phys. Rev. B*, 23:5384–5396, May 1981.

[86] P. Komninou, E. G. Doni, Th. Karakostas, G. L. Bleris, and P. Delavignette. High-symmetry triple junctions in polycrystalline silicon. *Journal of Applied Crystallography*, 24(3):232–238, June 1991.

[87] H. Kahn. Homogeneous nucleation during crystallization of amorphous silicon produced by low-pressure chemical vapour deposition. *Philosophical Magazine A*, 82(1):137–165, January 2002.

[88] K. V. Shanavas, K. K. Pandey, Nandini Garg, and Surinder M. Sharma. Computer simulations of crystallization kinetics in amorphous silicon under pressure. *Journal of Applied Physics*, 111(6):063509, 2012.

[89] Michael A. Lieberman. *Principles Of Plasma Discharges For Materials Processing.* John Wiley & Sons Inc, 2005.

[90] G. Lavareda, C. Nunes, A. Amaral, J. P. Conde, M. Vieira, and V. Chu. Properties of high growth rate amorphous silicon deposited by MC-RF-PECVD. *Vacuum*, 64(3-4):245–248, January 2002.

[91] W. Van Sark, J. Bezemer, and W. F. Van Der Weg. Role of ions in PECVD of amorphous silicon. *Surface and Coatings Technology*, 74-75:63–66, September 1995.

[92] E. Amanatides, E. Katsia, D. Mataras, A. Soto, and G. Voyiatzis. Temperature effect and stress on microcrystalline silicon thin films deposited under high pressure plasma conditions. *Thin Solid Films*, 511-512:603–607, July 2006.

[93] S. C. Siah, B. Hoex, and A. G. Aberle. Accurate characterisation of silicon nitride films on rough silicon surfaces by ellipsometry. *Energy Procedia*, 8(0):122–127, 2011.

[94] P. Van Veenendaal, Gerard W. M. Van Der Mark, J. K. Rath, and R. Schropp. Spectroscopic and kinetic ellipsometry studies of hot-wire deposited polycrystalline silicon on glass. *Thin Solid Films*, 430(1-2):41–45, 2003.

[95] F. Law, B. Hoex, J. Wang, J. Luther, K. Sharma, M. Creatore, and Van de Sanden. Kinetic study of solid phase crystallisation of expanding thermal plasma deposited a-Si:H. *Thin Solid Films*, 520(17):5820–5825, June 2012.

[96] Jason Trask, Andrew J Wagner, K Andre Mkhoyan, and Lin Cui. Seed-induced crystallization of amorphous silicon for the formation of large-grain poly-crystalline silicon. *Proceedings of the 4th International Conference on Energy Sustainability*, pages 1–4, 2010.